NASA TECHNICAL NOTE

NASA TN D-2969

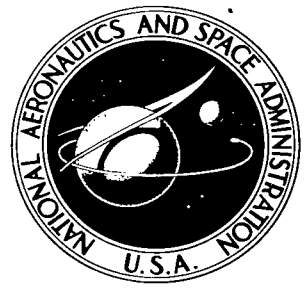

NASA TN D-2969

AN EXPERIMENTAL AND THEORETICAL INVESTIGATION OF THE PRESSURE DISTRIBUTION AND FLOW FIELDS OF BLUNTED CONES AT HYPERSONIC MACH NUMBERS

by Joseph W. Cleary

Ames Research Center
Moffett Field, Calif.

NATIONAL AERONAUTICS AND SPACE ADMINISTRATION • WASHINGTON, D. C. • AUGUST 1965

NASA TN D-2969

AN EXPERIMENTAL AND THEORETICAL INVESTIGATION OF THE PRESSURE DISTRIBUTION AND FLOW FIELDS OF BLUNTED CONES AT HYPERSONIC MACH NUMBERS

By Joseph W. Cleary

Ames Research Center
Moffett Field, Calif.

NATIONAL AERONAUTICS AND SPACE ADMINISTRATION

For sale by the Clearinghouse for Federal Scientific and Technical Information
Springfield, Virginia 22151 – Price $3.00

AN EXPERIMENTAL AND THEORETICAL INVESTIGATION OF THE PRESSURE DISTRIBUTION AND FLOW FIELDS OF BLUNTED CONES AT HYPERSONIC MACH NUMBERS

By Joseph W. Cleary
Ames Research Center

SUMMARY

An experimental and theoretical investigation of the flow of a perfect gas over spherically blunted cones has been conducted at hypersonic Mach numbers. Numerical solutions for inviscid flow at zero angle of attack are presented and analyzed to show the effect of cone angle on surface-pressure distribution for Mach numbers of 10 and ∞ and specific-heat ratios of 1.4 and 1.667. Profiles of the inviscid shock-layer flow properties for a 15° half-angle blunted cone are given at several axial stations.

Experimental longitudinal and circumferential pressure distributions for 15° and 30° half-angle blunted cones with bluntness ratios of 6 and 5.45, respectively, were obtained from wind-tunnel tests in air. The pitot-pressure distribution was measured in the shock layer of a 15° blunted cone at angle of attack. Pitot traverses were made at two axial stations to show the thinning of the entropy layer.

At 0° angle of attack, the experimental pressure distributions and pitot traverses of the shock layer compare favorably with the inviscid numerical theory but some viscous effects were observed. Theory and experiment both demonstrate the existence of a high total-pressure layer enclosing the low total-pressure layer adjacent to surfaces of blunted cones. The high total-pressure layer is a result of an inflection of the shock that is a characteristic of the three-dimensionality of flow over blunted cones. For windward surfaces, increasing angle of attack brings the high total-pressure layer in close proximity to the cone surface; this may influence transition of the boundary layer.

INTRODUCTION

Comparative studies of convective and radiative heating during entry at speeds greater than parabolic speed were made in reference 1 to determine how to minimize aerodynamic heating of sharp conical bodies. The advantage of preserving laminar flow throughout the entry was demonstrated. Previous research (refs. 2 and 3, for example) has shown that a small amount of bluntness is conducive to delaying boundary-layer transition. Blunted cones merit further study both because some blunting of the tip due to extreme heating appears unavoidable and because blunting has favorable effects on transition.

Blunting alters the flow so that properties of the shock layer are influenced many nose radii downstream. The fluid passing through the strong shock part of the curved bow wave undergoes a significant reduction of total pressure and forms a low-density, high-entropy layer that, for conical shapes, diminishes in thickness with increasing axial distance from the nose. Near the nose, the distribution of flow properties in the shock layer is similar to that predicted by blast-wave theory while, many nose radii downstream, the distribution is essentially conical except for the thin entropy layer. As the entropy layer thins with increasing axial distance, the surface pressure expands below, and then approaches, asymptotically, the sharp-cone pressure. This overexpansion of the flow is highly dependent on cone angle. These effects of bluntness may have an important bearing on control effectiveness, flow separation, heat transfer, and type of boundary layer.

The foregoing effects of bluntness can be predicted qualitatively by analytical studies of axisymmetric blunted-cone flows (see refs. 2 to 9, for example). However, these analytical methods do not predict all aspects of the flow over a specified blunted cone. For example, experiment has shown that for a range of cone angles, blunted-cone flows have an inflection in the shock that does not appear amenable to simplified analytical treatment. On the other hand, the numerical method of characteristics gives the true shock shape and all other features of the inviscid flow accurately. Since numerical methods for blunted axisymmetric bodies are restricted, at present, to a limited range of angles of attack (ref. 10), it is generally necessary to resort to experimental methods at large angles of attack.

The purpose of the present investigation is to study theoretically and experimentally the flow field over blunted cones. Numerical results are presented for zero angle of attack to show the effects of cone angle, specific-heat ratio, and Mach number on surface-pressure distribution and pressure drag. Also shown are profiles of shock-layer properties for a 15° half-angle blunted cone. Experimental results are presented to show the effect of angle of attack on the longitudinal and circumferential pressure distribution for 15° and 30° half-angle blunted cones at Mach numbers of 5.25, 7.4, and 10.6. Also shown are experimental pitot traverses of the shock layer at two stations for a Mach number of 10.6 that demonstrate the thinning of the entropy layer and how it is affected by angle of attack. Numerical and experimental results are compared to illustrate viscous effects and to verify the main features of the numerical solutions.

SYMBOLS

A area

A_b cone base area

C_D drag coefficient, $\frac{\text{drag}}{q_\infty A_b}$

C_p pressure coefficient, $\frac{p - p_\infty}{q_\infty}$

d_s shock standoff distance

l length of cone

M	Mach number
p	static pressure
p_t	total pressure
q	dynamic pressure, $\frac{1}{2}\rho V^2$
R	nose radius
R_o	gas constant
Re*	Reynolds number, per foot
R_s	radius of curvature of shock for r = 0
s	entropy
T_t	total temperature
u, v	velocity components in the x, r directions
V	velocity
x, r	wind-axis cylindrical coordinates
x'	body-axis coordinate
α	angle of attack
γ	ratio of specific heats
δ	cone half-angle
η	coordinate normal to body surface
θ	shock angle
ξ	body surface coordinate from the nose
ρ	density
φ	circumferential angle in body cylindrical coordinate system
ω	surface inclination to free-stream velocity

Subscripts

b	base
c	cone surface
min	minimum value
p	pitot
s	shock
stag	stagnation point on body
∞	free stream
2	immediately behind shock

Superscripts

—	correlation parameters (eqs. (10) and (11))
~	along streamline of maximum total pressure

NUMERICAL METHOD

Solutions of the flow over blunted cones were obtained by numerically solving the complete inviscid equations of a perfect gas. The computations were performed on an IBM 7090 computer by essentially the same method as that

of reference 11. The same method was used to study blunted-wedge flows in reference 12. The procedure consists of two parts: (1) An inverse numerical solution of the subsonic and transonic flow over the blunted nose is used to provide properties of the flow beyond the sonic line, and (2) from these supersonic inputs along a line from the body to the shock, the solution is continued downstream by the axisymmetric method of characteristics. Sketch (a)

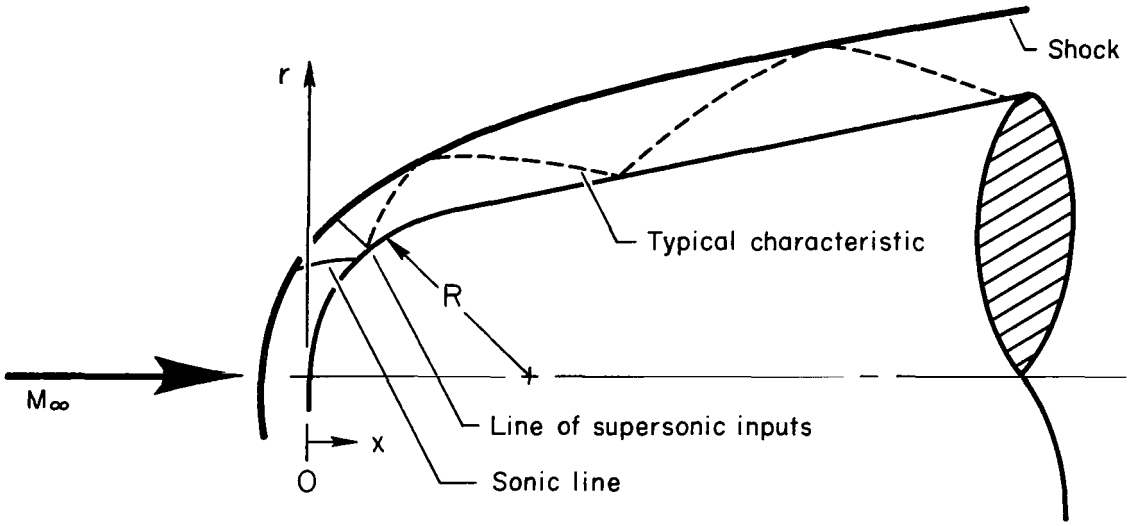

Sketch (a)

illustrates the main features of the method. Twelve inputs were used from the body to the shock to start the characteristics net since this number was found sufficient to provide accurate solutions. A quadratic interpolation of entropy was used in the numerical calculation of the characteristics net to obtain accurate profiles of the flow properties within the shock layer. In most cases, solutions were achieved over an axial distance of about 60 nose radii. Solutions were computed for cone angle increments of 5° from a cone angle of 0° to the maximum possible before the flow became locally subsonic, thereby invalidating the method of characteristics. Solutions were computed for specific-heat ratios of 1.4 and 1.667 and Mach numbers of 10 and ∞ (actual $M_\infty = 10{,}000$). Corresponding solutions for blunted wedges are given in reference 12.

EXPERIMENTAL METHOD

Wind-Tunnel Facility

The tests were conducted in air in the Ames 3.5-Foot Hypersonic Wind Tunnel. The tunnel circuit is shown schematically in figure 1. High-pressure air is heated in the pebble-bed heater and flows through the axisymmetric test section to the vacuum spheres. The nozzle and test section are cooled by helium which is introduced through an annular slot in the nozzle at the subsonic entrance.

The model support system is hydraulically actuated and servo-controlled over an angle-of-attack range of -5° to $+15^{\circ}$. The operation of the wind tunnel is automatic, and the model attitude sequence and the tunnel total pressure are programmed into a controller prior to a run. Data are recorded on magnetic tape. For the test results presented herein, the total temperature was 2000° Rankine, and the Mach number and the free-stream Reynolds number per foot were

M_∞	Re^*_∞
5.25	1.4×10^6
7.4	3.2×10^6 (3.7×10^6 for shadowgraphs)
10.6	1.0×10^6

Although the total temperature of the air was sufficient to partially excite the vibrational mode of the molecules, the experimental results can be considered essentially those of a perfect gas with $\gamma = 1.4$.

Models and Test Procedure

The models were constructed from stainless steel and had a wall thickness of about 0.38 inch. Separate models were built for surface pressure measurements and for pitot traverses of the shock layer. The pressure models were blunted cones of 15° and 30° half angles. Geometrical details of these models and the position of pressure orifices are given in figure 2, and the models are shown mounted on the sting support in figures 3(a) and 3(b). Each model had three rows of pressure orifices installed at φ of 0°, 90°, and 180°. Pressure distributions for other values of φ were obtained by rotating the model and repeating the run. Measurements of pressure distribution were made at Mach numbers of 5.25, 7.4, and 10.6.

Pitot traverses were made only on a 15° half-angle blunted cone. This model was instrumented with movable pitot probes mounted on the top ($\varphi = 0^{\circ}$) at station $x'/R = 3.59$ and on the bottom ($\varphi = 180^{\circ}$) at station $x'/R = 16.67$ as shown in figure 3(c). Data for other values of φ were obtained by rotating the model. The 0.040-inch-diameter probes were actuated by an internally mounted electric motor, and their positions were measured with a potentiometer. It is believed from visual surface flow studies, that the data obtained with the rear probe are essentially free of interference from the forward probe. Slight local interference due to interaction of the probe bow shock with the adjacent boundary layer may have occurred when the probe was near the surface. However, this effect on the pitot-pressure measurements is believed unimportant. The probes were alined with the surface of the model and were, therefore, subject to some misalinement with the flow during the traverse. This misalinement was greatest for those traverses at angle of attack and not in the pitch plane. However, estimates from numerical solutions using first-order theory (ref. 10) indicate that the crossflow angles to the probes were less than 10°. This is believed within a range suitable for accurate measurements of pitot pressure.

Both the pressure distribution and pitot-traverse models were internally cooled and because the runs were about two minutes long, surface temperatures were well below the adiabatic wall temperature during the entire run. Surface- and pitot-pressure measurements were made at the beginning and end of each run to evaluate the effect of varying heat transfer; no significant effects were observed.

Although the models had a polished surface at the beginning of the tests, some abrasion of the surface occurred during the tests due to dust from the pebble-bed heater. This abrasion was greatest at Mach numbers of 5.25 and 7.4 and least at a Mach number of 10.6. The photographs of figure 3 give some indication of the model surface condition at the termination of the test. Before each run the model was restored to a comparatively smooth finish.

Precision

Random errors existed not only in reading and recording the pressure data but also in determining free-stream Mach number due to slight variations in total pressure and total temperature with time. Because there are also systematic errors in determining Mach number, a brief analysis of the effect of an error in Mach number on the precision of pressure coefficient was made. This analysis indicated that at a Mach number of 10, an error of 1 percent in determining Mach number caused an error of about 5 percent in pressure coefficient. On this basis and since the pressure cells have a precision of about 1 percent at the lowest pressures measured, it is believed the precision of pressure coefficients is about ±2 to ±4 percent. Angle measurements are accurate within $\pm 0.1^{\circ}$, and probe heights are accurate within ±0.02 inch.

NUMERICAL RESULTS FOR ZERO ANGLE OF ATTACK

A detailed study of properties at the surface and within the shock layer is essential for determining the main characteristics of the flow over blunted cones. Both surface and shock-layer properties are obtained from the numerical solutions, and the effects of varying cone angle, Mach number, and specific-heat ratio on the flow will now be considered. The surface-pressure distribution for the spherical nose and blunted cone and the integrated pressure drag will be considered initially for a wide range of cone angles. While blunted-cone flows are highly dependent on cone angle, for simplicity, shock-layer properties for only one representative cone angle of 15° will be given. It is believed that the interrelationship between surface and shock-layer properties will be indicative of the effects of cone angle on shock-layer properties for other cone angles. Finally, the total-pressure gradient at the surface will be examined, and an approximate correlation will be obtained.

Surface-Pressure Distribution

Hemispherical nose.- The effect of specific-heat ratio on the pressure distribution for a hemispherical nose is presented in figure 4 for Mach

numbers of 10 and ∞. The effect of specific-heat ratio on the forward part of the nose, $x/R < 0.4$, has been considered previously in reference 13; therefore, only the effect on the afterpart, $x/R > 0.4$, is of interest here. The solution for $M_\infty = \infty$ and $\gamma = 1$ of figure 4(b) is the Newton-Busemann solution with the centrifugal force correction. (A characteristics solution could not be achieved under these conditions.) Figure 4 shows that increasing specific-heat ratio has a small effect on pressure coefficient for the range $1.4 < \gamma < 1.667$, but pressure coefficient decreases significantly as $\gamma \to 1$. These effects and the almost negligible effect of Mach number for the range from 10 to ∞ are similar to those of plane flow shown in reference 12. The plane-flow pressure distribution for $\gamma = 1.4$ is shown here for comparison with that of the hemispherical nose. It can be observed from figure 4 that the pressure coefficient for $x/R = 1$ is twice as great for plane flow as for axisymmetric flow. It is apparent that any simple procedure for estimating this pressure coefficient (such as matching pressure gradients of Newtonian and Prandtl-Meyer flows, ref. 14) that does not account for differences between plane and axisymmetric flows may give only approximate results. This point will be demonstrated later when comparisons are made with experimental data.

Blunted cone.- The effects of cone angle and Mach number on the pressure distribution of blunted cones are presented in figures 5 and 6 for specific-heat ratios of 1.4 and 1.667, respectively. The overexpansion of the pressure below sharp-cone values for the larger cone angles of figures 5 and 6 was followed by a small oscillating overshoot and then an asymptotic return to sharp-cone values with increasing x/R. For shallow cone angles, the trends of the pressure distribution were similar to that for large cone angles but the oscillating overshoot occurred beyond the range of x/R shown in figures 5 and 6. Although increasing Mach number moved the minimum pressure point aft, the effect is generally small for the range of Mach numbers shown. A close examination of figures 5 and 6 shows that increasing Mach number increased the minimum pressure coefficient of shallow cones but decreased the minimum of the steeper cones.

As cone angle was increased, the tangent point approached the sonic line, and the numerical method of characteristics could not be used beyond the cone angle corresponding to sonic flow on the cone surface. Nevertheless, by an extrapolation of the pressure distributions of figures 5 and 6, speculations about the nature of the sonic lines of these flows can be made. A discussion of these flows is given in reference 15.

Pressure Drag

The pressure-drag coefficients of blunted cones have been obtained by graphically integrating the pressure distributions shown in figures 5 and 6. The results are presented in figures 7 and 8 for specific-heat ratios of 1.4 and 1.667, respectively, to show the effects of cone length and Mach number. A base pressure coefficient of 0 was assumed. The drag-coefficient curve of the sharp cone is also shown, and it envelops the blunted-cone curves. To the accuracy of these results, the inviscid drag coefficient of blunted cones is always greater than that of the sharp cone of the same angle when based on base area. This result is at variance with the theory of reference 9 where as

much as 10-percent reduction in drag coefficient is indicated by blunting sharp cones. It is believed the theory of reference 9 may overestimate the overexpansion phenomenon for these cases and result in the lower drag calculations. It is of interest that drag measurements at low supersonic Mach numbers for spherically blunted cones in reference 16 show total drag (viscous and pressure) greater than that of a sharp cone. While these results are not necessarily pertinent at hypersonic Mach numbers, they do indicate that blunting does not reduce drag.

Interrelationship Between Surface and Shock-Layer Properties

Before proceeding with a detailed study of the shock-layer profiles on blunted cones, it is helpful to examine the interrelationship between shock shapes, surface-pressure distribution, and total-pressure profiles. These properties are shown in figure 9 for several free-stream conditions and for a blunted wedge and cone with a half-angle of 15°. The solutions for blunted wedges were previously given in reference 12. The total-pressure profiles show relative values along a normal from the body to the shock at axial stations $x/R = 5$ and 20. It is apparent at the outset that overexpansion of surface pressure and inflection of the shock are three-dimensional phenomena. The overexpansion of pressure on blunted cones is similar to the isentropic compression in the shock layer of sharp cones in that both phenomena are uniquely due to three-dimensionality of the flow. Since the momentum and energy equations are identical for plane and axisymmetric flows, an account of the differences observed must lie in the equation of continuity. For this reason, it is instructive to examine the continuity equations of these flows in more detail. The continuity equations are

$$\frac{\partial(\rho u)}{\partial x} + \frac{\partial(\rho v)}{\partial r} = 0 \quad \text{plane flow} \tag{1}$$

$$\frac{\partial(\rho u)}{\partial x} + \frac{\partial(\rho v)}{\partial r} + \frac{\rho v}{r} = 0 \quad \text{axisymmetric flow} \tag{2}$$

Equation (1) is obviously satisfied for sharp-wedge flows since ρ, u, and v are constants. However, for the case of blunted-wedge flows, the distinguishing feature is that near the nose between the body and the shock $\partial(\rho v)/\partial r = -\partial(\rho u)/\partial x > 0$. Moreover, for that region of the flow where blast-wave effects are significant, the derivatives are comparatively large absolute numbers. Outside the entropy layer at a large distance from the nose these derivatives vanish, of course, and sharp-wedge theory is applicable. For axisymmetric flows, the term $\rho v/r$ has a modifying effect (see eq. (2)). Also, it can be demonstrated from solutions of sharp cones that $\partial(\rho v)/\partial r$ is always negative and $\partial(\rho u)/\partial x$ is positive and small. Near the nose of blunted cones, however, where blast-wave effects are significant, $\partial(\rho v)/\partial r$ is a large positive number and, to satisfy continuity, it is essential that $\partial(\rho u)/\partial x$ be negatively large. At some distance downstream of the blunted nose, it is evident that $\partial(\rho v)/\partial r$ must undergo a change in sign. Therefore, there is a curve along which

$$\frac{\partial(\rho u)}{\partial x} + \frac{\rho v}{r} = 0 \qquad (3)$$

Numerical solutions of blunted-cone flows indicate this curve occurs near, but just downstream, of the maximum total-pressure streamline. However, the possibility of integrating the equations of motion for this condition and thus establishing an analytical upper boundary on the maximum total-pressure streamline appears remote.

Properties of the Flow in the Shock Layer

Some of the general aspects of the three-dimensional nature of blunted-cone flows have been considered. To continue the study of the numerical solutions, it is worthwhile to explore some of the details of the entropy and shock layer. These details are most vividly portrayed by several traverses of the flow normal to the cone surface which show the effect of increasing x/R on the thinning of the entropy layer. Typical of a wide range of blunted-cone flows are the traverses of the shock layer for a 15° blunted cone which will now be considered.

Profiles of shock-layer properties.- Static and total pressure, Mach number, density, velocity, and dynamic-pressure profiles are presented in figures 10 and 11 for specific-heat ratios of 1.4 and 1.667, respectively. Sharp-cone values are also shown and are based on the same distance from the surface to the shock of the blunted cone at $x/R = 60$. The sharp-cone values illustrate the asymptotic return to conical flow at a large axial distance from the nose. Coincidentally, for this cone angle, the traverse at $x/R = 10$ intersects the shock at about where the shock-wave slope is a minimum.

From the several profiles of flow properties shown in figures 10 and 11, it can be observed that static pressure is most nearly in agreement with sharp-cone values for large x/R. On the other hand, total pressure appears to display the largest differences from sharp-cone values, and it is of interest to note the effects of Mach number and specific-heat ratio on these differences. The ratios of blunted-cone maximum total pressure to that of the sharp cone for $\gamma = 1.4$ is about 1.50 and 3.00 for Mach numbers of 10 and ∞, respectively, while for $\gamma = 1.667$, the corresponding values are 1.34 and 1.96. It is evident that the total-pressure ratio is significantly increased by increasing Mach number but decreased by increasing specific-heat ratio from 1.4 to 1.667. Since it can be argued on a Newtonian theory basis that the shock inflection vanishes for $M_\infty \to \infty$ and $\gamma \to 1$, apparently a maximum value of this total-pressure ratio exists between $\gamma = 1$ and 1.667. Because the minimum shock angle is essential for estimating the maximum total pressure of blunted-cone flows, values and coordinates of this minimum are given in figure 12.

Effective Reynolds number.- Figures 10(b) and 11(b) show that the thickness of the low total-pressure layer and the enveloping high total-pressure layer decreased inversely with x/R. Although increasing Mach number thinned

these layers, increasing the specific-heat ratio from 1.4 to 1.667 thickened them. It is reasonable to expect the high total-pressure layer may have an adverse effect on the local convective heat transfer to blunted cones after the total-pressure layer has become very thin. Under this condition, the high total-pressure layer would approach the edge of the boundary layer, and because of its greater kinetic energy, it would increase the shear at the wall by jet-like viscous interaction. Furthermore, the high total-pressure layer may cause earlier transition of the boundary layer from laminar to turbulent flow by increasing the effective Reynolds number at the boundary-layer edge. To estimate the effective Reynolds number, the ratio of Reynolds number per foot along the streamline of maximum total pressure to that of the streamline along the cone surface, $\tilde{R}e^*/Re_c^*$ was computed from the inviscid solutions by using Sutherland's viscosity law and a total temperature of 2000° Rankine. It should be noted that the unit Reynolds number on the maximum total-pressure streamline is about the maximum for all streamlines within the shock layer. The results of computations showing the effects of Mach number are given in figure 13 for cone angles of 15° and 30° and $\gamma = 1.4$. It is evident from figure 13 that the effective Reynolds number can be significantly increased by boundary-layer growth into the high total-pressure region. While the infinite Mach number curves shown in figure 13 represent a fictitious condition, a large effect of free-stream Mach number is indicated for a cone angle of 15°.

Surface Total-Pressure Gradient

The total-pressure gradient normal to the surface of blunted cones is of fundamental importance to studies of entropy and shock layers. Although these gradients may be obtained from the numerical solutions, in practice, accurate evaluations may be difficult unless the characteristic net has a sufficiently fine mesh. Because of this difficulty and since total-pressure gradients can be computed analytically, it is worthwhile to examine the analytical method and then compare its results with some appropriate values computed from the numerical solutions.

Analytical method.- A derivation of the total-pressure gradient at the surface of blunted bodies is given in appendix A by a one-dimensional analysis of the surface stream tube. There it is shown that the dimensionless surface total-pressure gradient is given by

$$\left[\frac{d\left(\frac{p_t}{p_{stag}}\right)}{d\left(\frac{\eta}{R}\right)}\right]_{\eta=0} = \frac{r}{R}\left(\frac{R}{R_s}\right)^2\left(\frac{2\gamma}{\gamma-1}\right)\frac{M}{M_2}\left(\frac{1+\frac{\gamma-1}{2}M_2^2}{1+\frac{\gamma-1}{2}M^2}\right)^{\frac{\gamma+1}{2(\gamma-1)}}\left[\frac{2M_\infty^2}{2\gamma M_\infty^2-(\gamma-1)}+\frac{(\gamma-1)M_\infty^2}{(\gamma-1)M_\infty^2+2}-1\right] \tag{4}$$

where

$$M_2^2 = \frac{(\gamma-1)M_\infty^2+2}{2\gamma M_\infty^2-(\gamma-1)} \tag{5}$$

Subsequent to the analysis given here, it was found that a solution for surface entropy gradient had been previously given in reference 17 by a somewhat different approach. It can be demonstrated, by transforming from entropy to total-pressure gradient, that the results of reference 17 are the same as equation (4).

It is evident from equation (4) that the total-pressure gradient depends on local Mach number and body radius, and the radius of curvature of the shock at the axis of symmetry. While local Mach number and shock radius of curvature can be estimated by simple theories and correlations, they are given accurately by the numerical solutions. Therefore, to present the most accurate values of total-pressure gradients, computations were made with equation (4) using values of local Mach number and shock radius of curvature from the numerical solutions. Also, the ratio of local body radius to nose radius, r/R, was computed for various cone angles and in terms of the axial coordinate, x/R, by equation (6).

$$\frac{r}{R} = \frac{x}{R} \tan \delta + \frac{1 - \sin \delta}{\cos \delta} \tag{6}$$

The results are presented in figures 14 and 15 for specific-heat ratios of 1.4 and 1.667, respectively, in terms of the axial coordinate, x/R. Also shown are values of total-pressure gradient computed from the numerical solutions assuming a linear variation of total pressure from the surface to the nearest point in the flow field. For shallow cone angles, figures 14 and 15 show good agreement of the numerical solutions with the analytical method. Differences are believed due to inaccuracies in the assumption of a linear total-pressure variation when computing the numerical values. This is highly dependent on cone angle and precludes presenting extensive results for cones of large angles.

Approximate method and correlations.- Estimating total-pressure gradients expediently using equation (4) requires other methods than numerical solutions to evaluate M and R/R_S. One possibility that will be considered is to estimate M and R/R_S from available correlations and approximations of pressure distribution. An accurate correlation of R/R_S from numerical solutions has been achieved in reference 18 from which

$$\frac{R}{R_S} = \frac{1.28}{1 + \sqrt{\frac{8}{3} \frac{\rho_\infty}{\rho_2}}} \tag{7}$$

where

$$\frac{\rho_\infty}{\rho_2} = \frac{(\gamma-1)M_\infty^2 + 2}{(\gamma+1)M_\infty^2} \tag{8}$$

is the density ratio across a normal shock. Local Mach number may be evaluated by

$$M^2 = \frac{2}{\gamma - 1}\left\{\frac{\gamma + 1}{2} M_\infty^2 \left[\frac{\gamma + 1}{2\gamma M_\infty^2 - (\gamma-1)}\right]^{\frac{1}{\gamma}}\left(\frac{1}{\frac{\gamma}{2} M_\infty^2 C_p + 1}\right)^{\frac{\gamma-1}{\gamma}} - 1\right\} \tag{9}$$

if the distribution of pressure coefficient is known, and it is assumed that the flow has expanded isentropically after crossing a normal shock. This distribution can be estimated from references 8 and 9, for example, or determined experimentally. A more approximate method that will be considered here is to neglect the overexpansion and assume the pressure distribution is the same as that of sharp-cone theory. To test the adequacy of this assumption, computations were made for a wide range of cone angles and values of r/R using equations (7) and (9) with sharp-cone values of pressure coefficient. The results are presented in figure 16 in terms of the correlation parameters

$$\overline{\left[\frac{d\left(\frac{p_t}{p_{stag}}\right)}{d\left(\frac{\eta}{R}\right)}\right]_{\eta=0}} = \frac{\left[\frac{d(p_t/p_{stag})}{d(\eta/R)}\right]_{\eta=0}}{\left(\frac{R}{R_s}\right)^2\left(\frac{2\gamma}{\gamma-1}\right)\left[\frac{2M_\infty^2}{2\gamma M_\infty^2 - (\gamma-1)} + \frac{(\gamma-1)M_\infty^2}{(\gamma-1)M_\infty^2 + 2} - 1\right]} \tag{10}$$

and

$$\overline{r} = \frac{r}{R}\left(\frac{M}{M_2}\right)\left(\frac{1 + \frac{\gamma - 1}{2} M_2^2}{1 + \frac{\gamma - 1}{2} M^2}\right)^{\frac{\gamma+1}{2(\gamma-1)}} \tag{11}$$

The values of $\left[\frac{d(p_t/p_{stag})}{d(\eta/R)}\right]_{\eta=0}$ used in correlating equation (10) were computed from equation (4) with numerical solutions for R/R_s and M; therefore, deviations from the straight line of perfect correlation of figure 16 is a reflection primarily of inaccuracies in estimating M by using sharp-cone pressure. For shallow cone angles and small values of $\overline{r}$ comparatively large deviations from perfect correlation are shown in figure 16. On the other hand for large values of $\overline{r}$ the approximate method gives accurate results.

DISCUSSION OF EXPERIMENTAL RESULTS FOR ANGLE OF ATTACK

The experimental data presented are surface-pressure distributions, pitot traverses of the shock layer, and shadowgraphs of the flow. Since theory cannot adequately predict the effects of large angles of attack, emphasis will be mainly on these effects.

Surface-Pressure Distribution

Surface-pressure distributions for the 15° blunted-cone model are presented in figures 17, 18, and 19 for Mach numbers 5.25, 7.4, and 10.6, respectively. In a similar manner, pressure data are given in figures 20, 21, and 22 for the 30° blunted-cone model. Although anomalous scatter exists in some of the data, the effects of α and φ are, in general, consistent for all Mach numbers. The data for $M_\infty = 10.6$ appear to have the least scatter and for this reason are perhaps the most reliable. At small angles of attack, the drop-off in the pressure distribution near the base of the 30° blunted-cone model (see figs. 20, 21, and 22) is believed due to thinning of the boundary layer by the strong expansion at the base. However, at large angles of attack, the flow may be locally subsonic on windward surfaces, and this may also be a factor.

The overexpansion of pressure below the sharp-cone value, as predicted by the characteristic solutions for $\alpha = 0$ (fig. 5), is borne out by the experimental data. For surfaces whose inclination to free stream is increased (by varying α and φ), the minimum pressure point moves toward the nose while the opposite is true if the surface inclination is decreased. To aid in interpreting these effects, the inclinations of conical surface elements to the free stream have been computed by equation (12) and are given in table I. The geometrical relationship of the angles pertinent to these computations are shown in sketch (b)

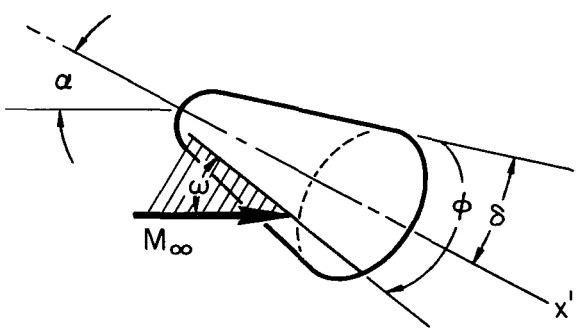

Sketch (b)

$$\sin \omega = \sin \delta \cos \alpha - \cos \delta \cos \varphi \sin \alpha \qquad (12)$$

When the surface element is alined with the free stream as shown in figure 19(a), for example, with $\alpha = 15^\circ$ and $\varphi = 0^\circ$, the pressure distribution is of blast-wave type. On the other hand, for surface elements whose inclination is greatest (fig. 19(g) with $\alpha = 15^\circ$, $\varphi = 180^\circ$), the minimum pressure is followed by a compression that significantly overshoots the final asymptotic level. This overshoot is greater than the slight overshoot of the characteristic solution having the same inclination of the surface (see fig. 5(a), $\delta = 30^\circ$). Because of the extremely thin boundary layer, it is unlikely that the overshoot and the saddle-type pressure distribution along the most windward rays is a viscous effect. More likely, the entropy layer is

thinned more rapidly (by the circumferential pressure gradient) than that which occurs for the equivalent cone at $\alpha = 0^\circ$, causing a magnification of the overshoot.

At $\varphi = 90^\circ$, pressure data are given only for α of 0° and 15° for clarity; pressures at intermediate angles of attack can be estimated by linear interpolation. For the 15° model the pressure distribution along this ray appears insensitive to increasing angle of attack, but a small decrease in pressure can be observed on the 30° model. These effects are consistent with the larger decrease of inclination of the 90° ray of the 30° model as angle of attack was increased (see table I).

Pitot Traverses of the Shock Layer

Pitot traverses of the shock layer were made at stations $x'/R = 3.59$ and 16.67 of the 15° blunted-cone model to investigate the effects of angle of attack on the entropy and boundary layers. The results are presented in figure 23 for $M_\infty = 10.6$ and $R^*_\infty = 1.0 \times 10^6$. In order to simplify the presentation, the data obtained for $\varphi > 90^\circ$ and $\alpha > 0^\circ$ are shown reflected in the model horizontal plane of symmetry as if obtained for $\alpha < 0^\circ$. The traverses were made normal to the model surface and except on leeward surfaces for high angles of attack, the shock was penetrated as shown by the abrupt change in pitot-pressure coefficient to the free-stream value of about 1.83. No corrections have been applied to the pitot measurements for the effect of vorticity on the effective pitot position or for pitot misalinement to the local flow. The former correction was small and unimportant for this investigation, while the latter correction could not be made since the local stream direction was unknown. However, for stream-angle deviations less than about 15°, the correction for pitot misalinement should be unimportant. (The effect of stream misalinement is to measure pitot pressures less than true values.) Also shown in figure 23 are the maximum possible theoretical values of pitot-pressure coefficient that can be attained in sharp-wedge and axisymmetric conical flows. These maximums occur for wedge and cone angles of about 21.2° and 23.5°, respectively. The maximum possible conical pitot-pressure coefficient is exceeded by about 10 percent for $\alpha = -5^\circ$ and $\varphi = 30^\circ$ at station $x'/R = 16.67$ (see fig. 23(b)). It is interesting that for the many possible processes occurring in blunted-cone flows when at angle of attack, the maximum pitot-pressure coefficient is only slightly greater than the maximum conical-flow value.

Interpretation of pitot traverses.- Without knowledge of local static pressure or Mach number, measurements of pitot pressure require careful interpretation. Nevertheless, if the static-pressure variations across the shock layer are assumed to be small, some observations of the nature of the flow can be made. On this basis, an examination of the data indicates it is possible to classify most of the traverses into two rather broad categories. Those traverses for which pitot pressure is a maximum at the shock are classified as of blast-wave type having thick entropy layers. On the other hand, those for which pitot pressure is a maximum within the shock layer are classified as of blunted-cone type, occurring after the inflection in the shock where some thinning of the entropy layer has occurred. Depending on α and φ, both types of

distributions of pitot pressure were observed at the fore and aft stations as shown in figure 23. It can be observed that for positive angles of attack and for all circumferential angles, the traverses at station $x'/R = 3.59$ can be approximately correlated by normalizing the ordinate by the distance to the shock. This self-similar property is fundamental to blast-wave theory and indicates that crossflow effects are small, and the flow is mainly dominated by nose bluntness. On the other hand, at station $x'/R = 16.67$, the flow is of blast-wave type only for a limited range of α and φ (approximately $\alpha \geq 10^\circ$ and $\varphi \leq 30^\circ$). For this station at negative angles of attack, the entropy layer was sufficiently thinned by the circumferential pressure gradient that the streamline of maximum total pressure lies close to the model surface. For negative angles of attack, the entropy layer grows in thickness with increasing φ, and if allowance is made for orientation of φ and α, it is easy to visualize from figure 23 the rapid growth in thickness as the leeward surface is approached.

At low angles of attack on windward surfaces the boundary layer was barely discernible since it was only of the order of 1 or 2 probe diameters in thickness at the aft station (see fig. 23). For leeward surfaces ($\alpha \geq 5^\circ$ and $\varphi \leq 30^\circ$) the boundary layer was sufficiently thickened by the circumferential flow that a definite profile was measured. Increasing angle of attack caused significant thickening of the boundary layer, similar to the effect on the entropy layer.

Effect of Angle of Attack on Boundary-Layer Transition

The effect of varying angle of attack on the flow over the 15° blunted-cone model at $M_\infty = 7.4$ and $R^*_\infty = 3.7 \times 10^6$ is shown by the shadowgraph pictures of figure 24. Because of the limited size of the tunnel windows, several pictures of the model at different tunnel stations were made, and the shadowgraphs of figure 21 are composites made from different runs. The sequence of shadowgraphs from the top to the bottom of figure 24 shows the effect of increasing surface inclination on the flow over the top surface of the model. The results show that for $\omega = 15^\circ$, fully developed turbulent flow, as indicated by the granular structure of the boundary layer, occurred near the base of the model. (The arrows of fig. 20 designate the approximate beginning of turbulence.) Preceding the turbulent flow is a region of transitional or incipient turbulent flow that is characterized by what appear to be vortex filaments with their axes somewhat alined with the flow. Laminar boundary layers cannot be detected under these test conditions and must be inferred from the absence of indications of transitional or turbulent flow.

Increasing surface inclination moved transition forward as indicated by the white arrows. It is noteworthy that the development of turbulent flow occurred after the inflection of the shock and near the location where the streamline of maximum total pressure approaches the edge of the boundary layer. In this regard, it is of interest to observe from the shock-layer pitot surveys of figure 23 the close approach of the maximum total-pressure streamline with increasing incidence at station $x'/R = 16.67$. Since the maximum total-pressure streamline is one of about maximum Reynolds number per foot (see fig. 13), it is clear the effective Reynolds number was increased by

growth of the boundary layer. To investigate this in more detail, the variation of Reynolds numbers per foot in the shock layer of 15° and 30° cones for about the same test conditions of the shadowgraphs have been computed from the inviscid characteristics solutions; the results are given in figure 25. Also shown to emphasize bluntness effects are values of unit Reynolds numbers for sharp cones. If the blunted 15° model is assumed to have a laminar boundary-layer run of about 1-1/2 feet, it would appear from figure 25(a) that the surface Reynolds number is insufficient to cause turbulent flow. On the other hand, if it is assumed the effective Reynolds number is the Reynolds number of the maximum total-pressure streamline, a Reynolds number of about 6×10^6 is estimated for $M_\infty = 7$. If the slightly abraded model surface is considered a secondary factor, turbulent flow might be expected at hypersonic Mach numbers for this Reynolds number.

COMPARISON OF NUMERICAL AND EXPERIMENTAL RESULTS

Comparisons are made of the experimental pressure distribution and pitot-pressure traverses with the inviscid numerical solutions. Differences other than scatter, between theory and experiment are indicative of viscous effects since the slight differences in Mach number between theory and experiment are unimportant.

Pressure Distribution

$\alpha = 0°$.- A comparison of the experimental and theoretical pressure distributions for the spherical nose is made in figure 26. The large number of experimental data points was obtained from just a few orifices (see fig. 26) by pitching the 15° model to 15° angle of attack. Therefore, only the data for $x'/R < 0.74$ can be legitimately compared with theory; the data for $x'/R > 0.74$ may be subject to a slight effect of crossflow. In general, the agreement of experiment and theory is good even for $x'/R > 0.74$. Shown for interest at a Mach number of 10 are the plane-flow numerical solution and the simpler analytical theory of reference 14. This theory matches pressure gradients (from modified Newtonian theory) over the forward part of the nose with a Prandtl-Meyer expansion to predict pressures over the aft part of the nose. For the conditions given, namely, $M_\infty = 10$ and $\gamma = 1.4$, the simple method closely predicts the more accurate axisymmetric numerical solution but significantly underestimates the plane-flow solution. The poor agreement with the plane-flow solution is believed due mainly to the inability of modified Newtonian theory to accurately predict plane-flow pressure distribution and pressure gradients over the forward part of the nose where the matching of Prandtl-Meyer and Newtonian pressure gradients were made.

Pressure distributions for conical surfaces predicted by numerical theory are compared with experiment in figure 27. Previously unpublished data obtained in the Ames 10- by 14-Inch Wind Tunnel at a Mach number of about 5 are also shown. Although, in general, the agreement of theory and experiment is

good, better agreement with theory is indicated for data obtained with the 15° model than with the 30° model. In general, viscous effects caused a slight increase in pressure coefficient as expected.

$\alpha > 0^{\circ}$.- Accurate inviscid solutions of blunted-cone flows at large angles of attack cannot be obtained, at present, by either analytical or numerical theory. A possible approach to the problem of large angles of attack is to consider the pressure distribution to depend solely on surface inclination. This method, which is essentially an extension of the tangent-cone approximation, specifies the same pressure distribution for a given ray of a blunted cone at angle of attack as that of another blunted cone of larger cone angle at 0° angle of attack but whose rays have the same incidence to the free stream. On this basis, experimental data of blunted 15° and 30° cones at angle of attack are compared with the numerical solutions in figure 28 for rays lying in the vertical plane of symmetry. For a valid comparison, it is essential to transform the body axial positions of the orifices of the models to new equivalent positions in the wind-axis system of the numerical solutions. This transformation was previously derived in reference 12 and is given by equation (13)

$$\frac{x}{R} = \frac{x'/R \pm (\sin \alpha / \cos \omega)}{\cos \alpha + \sin \alpha \tan \omega} + 1 \qquad (13)$$

The positive sign of the numerator applies for leeward rays and the negative sign for windward rays. The angle, ω, is positive if the inclination is clockwise to the wind axis and negative if counterclockwise. As shown in figure 28, the agreement of the data with the numerical solutions is surprisingly good for both models. At low angles of attack, the agreement is about as good as the more rigorous linearized numerical solution presented in the comparisons made in reference 10. Areas of relatively poor agreement are the greater overshoot of data of the 15° model windward ray and the slightly greater pressures of the 30° model leeward ray when at angle of attack.

Pitot Traverses of the Shock Layer

Theoretical pitot traverses of the shock layer at $x/R = 3.59$ and 16.67 are compared with the experimental traverses of the 15° model in figure 29 for an angle of attack of 0°. Also shown is the sharp-cone (conical theory) solution based on the same distance to the shock. At $x/R = 3.59$, the agreement of theory with experiment is excellent, and the effect of the thin boundary layer on the experimental data was insignificant. While agreement of theory with experiment at $x/R = 16.67$ was not as good as the more forward station, the experimental and theoretical pitot profiles are quite similar. In particular, the distance to the shock and the type of distribution of pitot pressure in the entropy layer are in close agreement indicating that boundary-layer effects were generally small. The differences shown in maximum pitot pressure at $x/R = 16.67$ may be partly a viscous effect due to shearing within the shock layer. Of interest is the thinning of the entropy layer that occurred between $x/R = 3.59$ and 16.67 and the approach of theory and experiment to conical flow at $x/R = 16.67$.

CONCLUDING REMARKS

Results of an experimental and theoretical investigation of the pressure distribution and shock-layer properties of spherically blunted cones have been presented. The inviscid theoretical solutions demonstrate the unique characteristics of blunted-cone flows. The more pertinent features are an overexpansion of surface pressure below the sharp-cone value and an inflection of the shock. Associated with the shock inflection is a minimum shock angle which results in a streamline of maximum total pressure and unit Reynolds number within the shock layer. These theoretical results were borne out by experimental data of 15° and 30° blunted cones having bluntness ratios of 6.0 and 5.45, respectively. Thinning of the entropy layer at a distance downstream of the nose brings the maximum total-pressure streamline in close proximity to the blunted-cone surface. This effect is accentuated by increasing inclination of windward surfaces.

A preliminary investigation indicated the shock inflection may be a factor in the development of turbulent flow by increasing the effective Reynolds number at the edge of the boundary layer. It was observed that increasing the angle of attack of the 15° blunted-cone model moved both the inflection of the shock and transition of the flow towards the nose on windward surfaces.

Ames Research Center
National Aeronautics and Space Administration
Moffett Field, Calif., May 19, 1965

APPENDIX A

DERIVATION OF THE LOCAL TOTAL-PRESSURE GRADIENT AT THE SURFACE OF A BLUNTED AXISYMMETRIC BODY

An equation is derived for the local total-pressure gradient at the surface of a blunted body. The derivation is based on a one-dimensional analysis of the flow that has passed through the normal-shock part of the bow wave. Sketch (c) illustrates the pertinent geometrical features of the analysis and

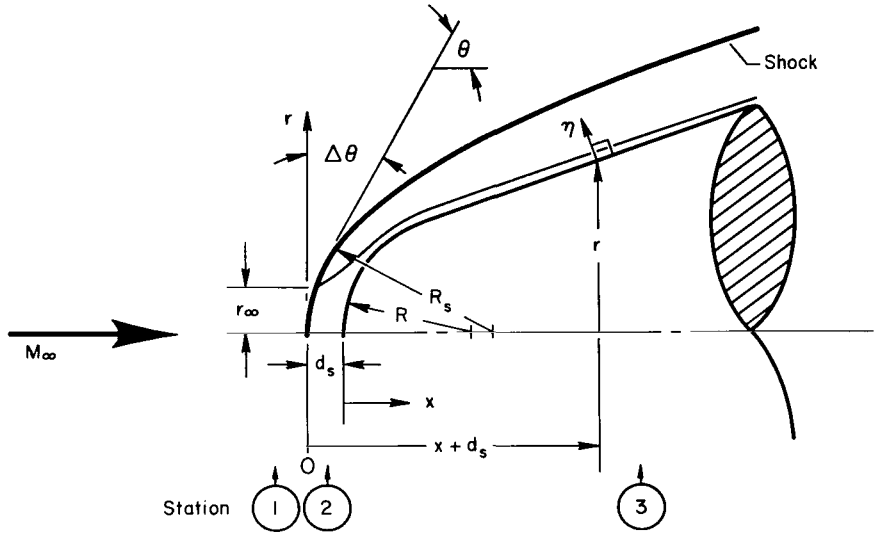

Sketch (c)

shows a streamtube adjacent to the body surface. The one-dimensional analysis is applied to the flow within this streamtube as r_∞ and $\Delta\theta \to 0$. For convenience, the origin of the rectangular coordinates has been selected on the center line at the shock. Since total pressure is constant along a streamline behind the shock, the local total pressure can be expressed as a function of shock angle by a Taylor series expansion

$$p_t = p_{t_2} = p_{stag} + \frac{dp_{t_2}}{d\theta}\Delta\theta + \frac{1}{2}\frac{d^2p_{t_2}}{d\theta^2}\Delta\theta^2 + \cdots \qquad (A1)$$

It is necessary to retain the term $(1/2)(d^2p_{t_2}/d\theta^2)\Delta\theta^2$ because, as will be shown later, $dp_{t_2}/d\theta$ vanishes as $\Delta\theta \to 0$ and $\theta \to \pi/2$.

At a large axial distance from the nose, station (3), the total pressure, to first order, varies linearly with distance from the body surface; therefore,

$$p_t = p_{stag} + \frac{dp_t}{d\eta}\,\eta \tag{A2}$$

Substituting equation (A2) in equation (A1) gives (since $(dp_{t_2}/d\theta)_{\theta=\pi/2} = 0$) in the limit $\eta \to 0$

$$\left(\frac{dp_t}{d\eta}\right)_{\eta=0} = \left(\frac{1}{2}\,\frac{d^2p_{t_2}}{d\theta^2}\,\frac{\Delta\theta^2}{\eta}\right) \tag{A3}$$

From streamtube geometry it is apparent that

$$\frac{A_2}{A} = \frac{\pi r_\infty^2}{2\pi r \eta} = \frac{r_\infty^2}{2r\eta} \tag{A4}$$

where by continuity

$$\frac{A_2}{A} = \frac{M}{M_2}\left(\frac{1 + \frac{\gamma - 1}{2}M_2^2}{1 + \frac{\gamma - 1}{2}M^2}\right)^{\frac{\gamma+1}{2(\gamma-1)}} \tag{A5}$$

and

$$\frac{r_\infty}{R_s} = \sin\Delta\theta \cong \Delta\theta \tag{A6}$$

Solving equations (A4), (A5), and (A6) for $\Delta\theta^2/\eta$ gives

$$\frac{\Delta\theta^2}{\eta} = \frac{2r}{R_s^2}\,\frac{M}{M_2}\left(\frac{1 + \frac{\gamma - 1}{2}M_2^2}{1 + \frac{\gamma - 1}{2}M^2}\right)^{\frac{\gamma+1}{2(\gamma-1)}} \tag{A7}$$

and substituting equation (A7) in equation (A3) gives

$$\left(\frac{dp_t}{d\eta}\right)_{\eta=0} = \frac{r}{R_s^2}\,\frac{M}{M_2}\left(\frac{1 + \frac{\gamma - 1}{2}M_2^2}{1 + \frac{\gamma - 1}{2}M^2}\right)^{\frac{\gamma+1}{2(\gamma-1)}}\left(\frac{d^2p_{t_2}}{d\theta^2}\right)_{\theta=\pi/2} \tag{A8}$$

The derivative $d^2p_t/d\theta^2$ is evaluated from oblique-shock equations. Because of the complexity of obtaining this second derivative directly, it is convenient to introduce entropy as an intermediate variable. Therefore, immediately behind the shock

$$\frac{p_{t_2}}{p_{t_\infty}} = e^{-\frac{\Delta s}{R_o}} = \left[\frac{(\gamma+1)M_\infty^2 \sin^2\theta}{(\gamma-1)M_\infty^2 \sin^2\theta + 2}\right]^{\frac{\gamma}{\gamma-1}} \left[\frac{\gamma+1}{2\gamma M_\infty^2 \sin^2\theta - (\gamma-1)}\right]^{\frac{1}{\gamma-1}} \quad (A9)$$

where

$$\frac{\Delta s}{R_o} = \frac{1}{\gamma - 1} \ln\left[\frac{2\gamma M_\infty^2 \sin^2\theta - (\gamma-1)}{\gamma + 1}\right] - \frac{\gamma}{\gamma - 1} \ln\left[\frac{(\gamma+1)M_\infty^2 \sin^2\theta}{(\gamma-1)M_\infty^2 \sin^2\theta + 2}\right] \quad (A10)$$

The pertinent derivatives are

$$\frac{dp_{t_2}}{d\theta} = \frac{dp_{t_2}}{d(\Delta s/R_o)} \frac{d(\Delta s/R_o)}{d\theta} \quad (A11)$$

and by the chain rule

$$\frac{d^2p_{t_2}}{d\theta^2} = \frac{dp_{t_2}}{d(\Delta s/R_o)} \frac{d^2(\Delta s/R_o)}{d\theta^2} + \frac{d^2p_{t_2}}{d(\Delta s/R_o)^2} \left[\frac{d(\Delta s/R_o)}{d\theta}\right]^2 \quad (A12)$$

Also, from equation (A9)

$$\frac{dp_{t_2}}{d(\Delta s/R_o)} = -p_{t_\infty} e^{-(\Delta s/R_o)} \quad (A13)$$

from which

$$\frac{d^2p_{t_2}}{d(\Delta s/R_o)^2} = p_{t_\infty} e^{-(\Delta s/R_o)} \quad (A14)$$

and therefore

$$\frac{d^2p_{t_2}}{d\theta^2} = p_{t_\infty} e^{-(\Delta s/R)} \left\{\left[\frac{d(\Delta s/R_o)}{d\theta}\right]^2 - \frac{d^2(\Delta s/R_o)}{d\theta^2}\right\} \quad (A15)$$

Evaluation of Derivatives

Differentiating equation (A10) gives

$$\frac{d(\Delta s/R_O)}{d\theta} = \frac{2\gamma}{\gamma - 1}\left[\frac{2M_\infty^2 \sin\theta\cos\theta}{2\gamma M_\infty^2 \sin^2\theta - (\gamma-1)} + \frac{(\gamma-1)M_\infty^2 \sin\theta\cos\theta}{(\gamma-1)M_\infty^2 \sin^2\theta + 2} - \frac{\cos\theta}{\sin\theta}\right] \tag{A16}$$

and

$$\frac{d^2(\Delta s/R_O)}{d\theta^2} = \frac{2\gamma}{\gamma - 1}\left\{\frac{2M_\infty^2(\cos^2\theta - \sin^2\theta)}{2\gamma M_\infty^2 \sin^2\theta - (\gamma-1)} - \frac{8\gamma M_\infty^4 \sin^2\theta\cos^2\theta}{[2\gamma M_\infty^2 \sin^2\theta - (\gamma-1)]^2}\right.$$

$$\left. + \frac{(\gamma-1)M_\infty^2(\cos^2\theta - \sin^2\theta)}{(\gamma-1)M_\infty^2 \sin^2\theta + 2} - \frac{2(\gamma-1)^2 M_\infty^4 \sin^2\theta\cos^2\theta}{[(\gamma-1)M_\infty^2 \sin^2\theta + 2]^2} + \frac{1}{\sin^2\theta}\right\} \tag{A17}$$

The derivative $d^2p_{t_2}/d\theta^2$ as a function of shock angle can be evaluated by substituting equations (A9), (A16), and (A17) in equation (A15). Of importance to the present analysis, however, is the value of $d^2p_{t_2}/d\theta^2$ when $\theta \to \pi/2$. For this case, equation (A16) gives $[d(\Delta s/R_O)/d\theta]_{\theta=\pi/2} = 0$ and, therefore, from equation (A11) $(dp_{t_2}/d\theta)_{\theta=\pi/2} = 0$ as previously specified (see eq. (A3)). From equation (A17)

$$\left[\frac{d^2(\Delta s/R_O)}{d\theta^2}\right]_{\theta=\pi/2} = \frac{2\gamma}{\gamma - 1}\left[1 - \frac{2M_\infty^2}{2\gamma M_\infty^2 - (\gamma-1)} - \frac{(\gamma-1)M_\infty^2}{(\gamma-1)M_\infty^2 + 2}\right] \tag{A18}$$

and from equation (A9)

$$\left(e^{-\frac{\Delta s}{R_O}}\right)_{\theta=\frac{\pi}{2}} = \left[\frac{(\gamma+1)M_\infty^2}{(\gamma-1)M_\infty^2 + 2}\right]^{\frac{\gamma}{\gamma-1}}\left[\frac{\gamma+1}{2\gamma M_\infty^2 - (\gamma-1)}\right]^{\frac{1}{\gamma-1}} \tag{A19}$$

The second derivative, $(d^2p_t/d\theta^2)_{\theta=\pi/2}$, is given by substituting equations (A18) and (A19) in equation (A12) from which

$$\left(\frac{d^2p_{t_2}}{d\theta^2}\right)_{\theta=\frac{\pi}{2}} = -\left(\frac{2\gamma}{\gamma-1}\right)p_{t_\infty}\left[1 - \frac{(\gamma-1)M_\infty^2}{(\gamma-1)M_\infty^2 + 2}\right.$$

$$\left. - \frac{2M_\infty^2}{2\gamma M_\infty^2 - (\gamma-1)}\right]\left[\frac{(\gamma+1)M_\infty^2}{(\gamma-1)M_\infty^2 + 2}\right]^{\frac{\gamma}{\gamma-1}}\left[\frac{\gamma+1}{2\gamma M_\infty^2 - (\gamma-1)}\right]^{\frac{1}{\gamma-1}} \tag{A20}$$

which when substituted in equation (A8) gives the total-pressure gradient at the surface of a blunted body.

In order to make comparisons of the total-pressure gradients by equation (A8) with those from the numerical method of characteristics, it is convenient to have equation (A8) in dimensionless form. The final result (eq. (A21)) together with equation (A22) gives the total-pressure gradient at the surface of a blunted body as a function of free-stream conditions, local Mach number, and blunted-body geometry.

$$\left[\frac{d\left(\frac{p_t}{p_{stag}}\right)}{d\left(\frac{\eta}{R}\right)}\right]_{\eta=0} = \frac{r}{R}\left(\frac{R}{R_s}\right)^2\left(\frac{2\gamma}{\gamma-1}\right)\left(\frac{M}{M_2}\right)\left(\frac{1+\frac{\gamma-1}{2}M_2^2}{1+\frac{\gamma-1}{2}M^2}\right)^{\frac{\gamma+1}{2(\gamma-1)}}\left[\frac{2M_\infty^2}{2\gamma M_\infty^2-(\gamma-1)}+\frac{(\gamma-1)M_\infty^2}{(\gamma-1)M_\infty^2+2}-1\right] \tag{A21}$$

$$M_2^2 = \frac{(\gamma-1)M_\infty^2+2}{2\gamma M_\infty^2-(\gamma-1)} \tag{A22}$$

An expression similar to equation (A21) was derived in reference 17 for entropy gradient rather than total-pressure gradient by a somewhat different approach. To compare results from reference 17 with equation (A21), a transformation from entropy gradient to total-pressure gradient is required; this transformation is

$$\left[\frac{d(\Delta s/R_o)}{d(\eta/R)}\right]_{\eta=0} = -\left[\frac{d(p_t/p_{stag})}{d(\eta/R)}\right]_{\eta=0} \tag{A23}$$

The results from reference 17 in the nomenclature of this appendix when transformed to total-pressure gradient become

$$\left[\frac{d\left(\frac{p_t}{p_{stag}}\right)}{d\left(\frac{\eta}{R}\right)}\right]_{\eta=0} = \frac{\gamma\left(\frac{\gamma+1}{2}\right)^{\frac{\gamma+1}{\gamma-1}}}{\left(\frac{\gamma-1}{2}\right)^{\frac{\gamma}{\gamma-1}}}\left(\frac{r}{R}\right)\left(\frac{R}{R_s}\right)^2\left[\frac{(M_\infty^2-1)^2M_\infty^{\frac{\gamma+1}{\gamma-1}}}{\left(1+\frac{\gamma-1}{2}M_\infty^2\right)^{\frac{3}{2}}\left(\frac{2\gamma}{\gamma-1}M_\infty^2-1\right)^{\frac{\gamma}{\gamma-1}}}\right]\frac{M}{\left(1+\frac{\gamma-1}{2}M^2\right)^{\frac{\gamma+1}{2(\gamma-1)}}} \tag{A24}$$

Both methods (eqs. (A21) and (A24)) give the same form for the solution of total-pressure gradient but appear to differ in their dependence on M_∞, M, and γ. However, it can be shown they are the same, but the proof is tedious and will not be given.

REFERENCES

1. Allen, H. Julian; Seiff, Alvin; and Winovich, Warren: Aerodynamic Heating of Conical Entry Vehicles at Speeds in Excess of Earth Parabolic Speed. NASA TR R-185, 1963.

2. Moeckel, W. E.: Some Effects of Bluntness on Boundary-Layer Transition and Heat Transfer at Supersonic Speeds. NACA Rep. 1312, 1957.

3. Rogers, Ruth H.: Boundary Layer Development in Supersonic Shear Flow. AGARD Rep. 269, 1960.

4. Cheng, H. K.: Hypersonic Flow With Combined Leading-Edge Bluntness and Boundary-Layer Displacement Effect. Rep. AF-1285-A-4, Cornell Aeron. Lab., Inc., Aug. 1960.

5. Zakky, Victor; and Krause, Egon: Boundary Conditions at the Outer Edge of the Boundary Layer on Blunted Conical Bodies. ARL 62-386, Polytechnic Institute of Brooklyn, July 1962.

6. Yakura, James K.: Theory of Entropy Layers and Nose Bluntness in Hypersonic Flow. (International Hypersonics Conference: Hypersonic Flow Research, Cambridge, Mass., 1961.) Progress in Astronautics and Rocketry, vol. 7, Frederich R. Riddell, ed., Academic Press, 1962, pp. 421-470.

7. Dryer, Murray; and Lord, Michael: The Inviscid Shear Layer About Blunted Bodies in Hypersonic Flow. Rep. R-62-7, Martin Co., Denver, Colo., June 1962.

8. Salathé, E. P.: Entropy-Layer Theory for Pressure Distributions in Hypersonic Flow. RAD-TM-62-79, Avco Corp. Res. and Advanced Dev. Div., Oct. 1962.

9. Chernyĭ, Gorimir Gorimirovich: Introduction to Hypersonic Flow. Translated and edited by Ronald F. Probstein, Academic Press, 1961.

10. Rakich, John V.: Numerical Calculation of Supersonic Flows of a Perfect Gas Over Bodies of Revolution at Small Angles of Yaw. NASA TN D-2390, 1964.

11. Inouye, Mamoru; and Lomax, Harvard: Comparison of Experimental and Numerical Results for the Flow of a Perfect Gas About Blunt-Nosed Bodies. NASA TN D-1426, 1962.

12. Cleary, Joseph W.; and Axelson, John A.: Theoretical Aerodynamic Characteristics of Sharp and Circularly Blunt-Wedge Airfoils. NASA TR R-202, 1964.

13. Van Dyke, Milton; and Gordon, Helen D.: Supersonic Flow Past a Family of Blunt Axisymmetric Bodies. NASA TR R-1, 1959.

14. Kaufman, Louis G. II: Pressure Estimation Techniques for Hypersonic Flows Over Blunt Bodies. J. Astron. Sci., vol. X, no. 2, Summer 1963, pp. 35-41.

15. Traugott, Stephen C.: Some Features of Supersonic and Hypersonic Flow About Blunted Cones. J. Aerospace Sci., vol. 29, no. 4, April 1962, pp. 389-399.

16. Perkins, Edward W.; Jorgensen, Leland H.; and Sommer, Simon C.: Investigation of the Drag of Various Axially Symmetric Nose Shapes of Fineness Ratio 3 for Mach Numbers From 1.24 to 7.4. NACA Rep. 1386, 1958.

17. Hakkinen, R. J.: Supersonic Flow Near Two-Dimensional and Axially Symmetric Convex Corners and Curvature Discontinuities. Rep. SM-27747, Douglas Aircraft Co., Inc., July 15, 1958.

18. Inouye, Mamoru: Blunt Body Solutions for Spheres and Ellipsoids in Equilibrium Gas Mixtures. NASA TN D-2780, 1965.

TABLE I.- INCLINATION ANGLES, ω, OF CONICAL ELEMENTS

α \ φ	0	30	60	90	120	150	180
15° half-angle cone							
-5	20.00	19.31	17.45	15.02	12.46	10.66	10.00
-2	17.00	16.73	15.99	15.01	13.99	13.27	13.00
0	15.00	15.00	15.00	15.00	15.00	15.00	15.00
2	13.00	13.27	13.99	14.99	15.99	16.73	17.00
5	10.00	10.66	12.46	14.98	17.45	19.31	20.00
10	5.00	6.29	9.85	14.96	19.80	23.59	25.00
15	0.00	1.92	7.18	14.94	22.02	27.81	30.00
30° half-angle cone							
-5	35.00	34.30	32.40	30.06	27.41	25.64	25.00
-2	32.00	31.93	30.98	30.04	28.92	28.26	28.00
0	30.00	30.00	30.00	30.00	30.00	30.00	30.00
2	28.00	28.26	28.92	29.96	30.98	31.93	32.00
5	25.00	25.64	27.41	29.94	32.40	34.40	35.00
10	20.00	21.23	24.66	29.91	34.58	38.51	40.00
15	15.00	16.79	21.77	28.88	36.52	41.89	45.00

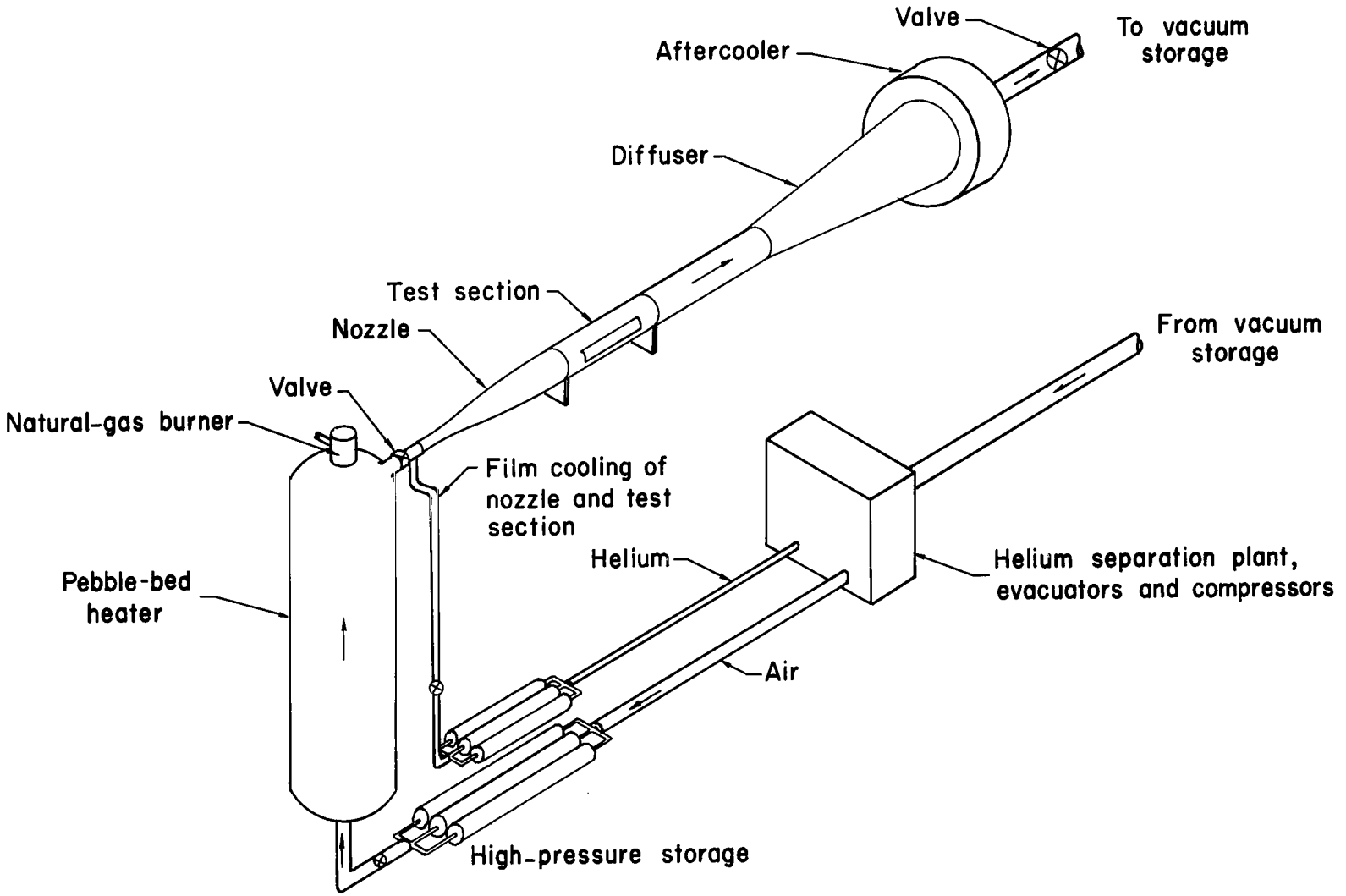

Figure 1.- Schematic arrangement of the 3.5-Foot Hypersonic Wind Tunnel.

Note: All dimensions in inches

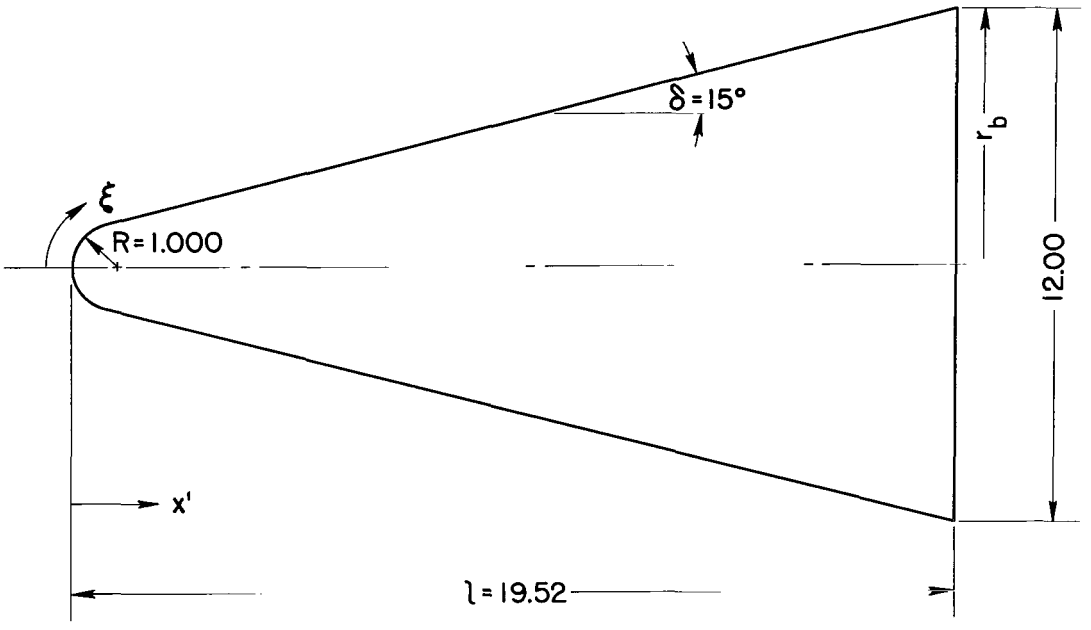

(a) 15° blunted-cone model, $r_b/R = 6$.

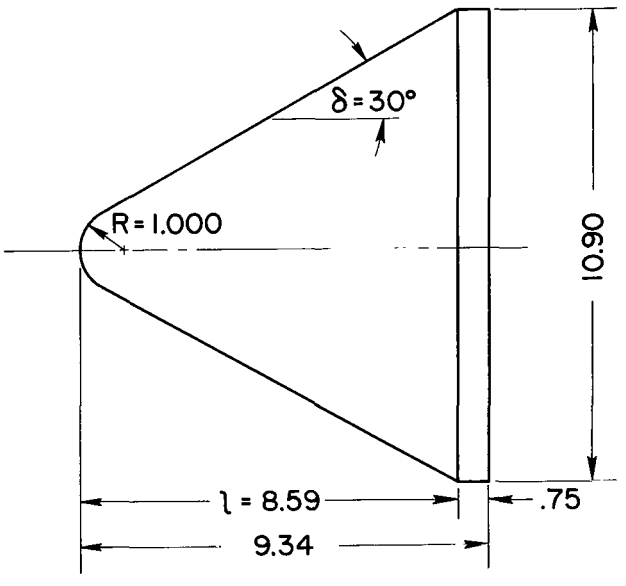

Orifice locations

15° model		30° model	
x'/R	ξ/R	x'/R	ξ/R
0	0	0	0
0.094	0.436	0.060	0.349
.357	.873	.234	.698
.741	1.310	.500	1.047
1.707	2.310	.933	1.547
2.673	3.310	1.799	2.547
4.605	5.310	2.665	3.547
6.537	7.310	3.531	4.547
8.466	9.310	4.399	5.547
10.401	11.310	5.265	6.547
12.333	13.310	6.130	7.547
14.265	15.310	7.000	8.547
16.197	17.310	7.860	9.547
18.121	19.310	8.430	10.247

$$\frac{\xi}{R} = \frac{\pi}{2} - \delta + \frac{x'/R - (1 - \sin\delta)}{\cos\delta}$$

(b) 30° blunted-cone model, $r_b/R = 5.45$.

Figure 2.- Dimensions and orifice locations for the test models.

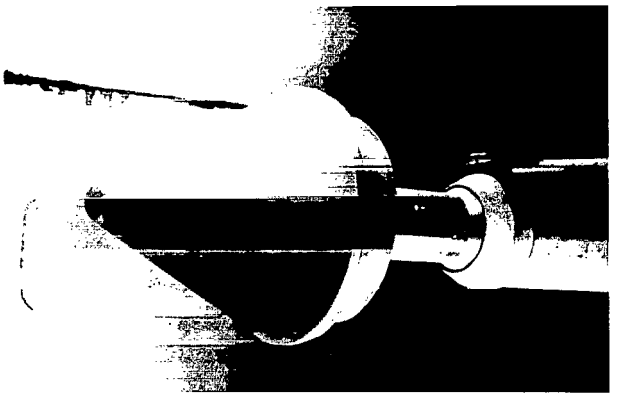

A-32127-24

(a) 30° pressure-distribution model.

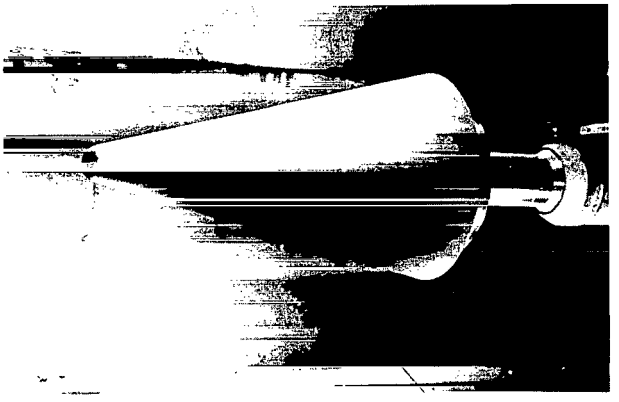

A-32127-26

(b) 15° pressure-distribution model.

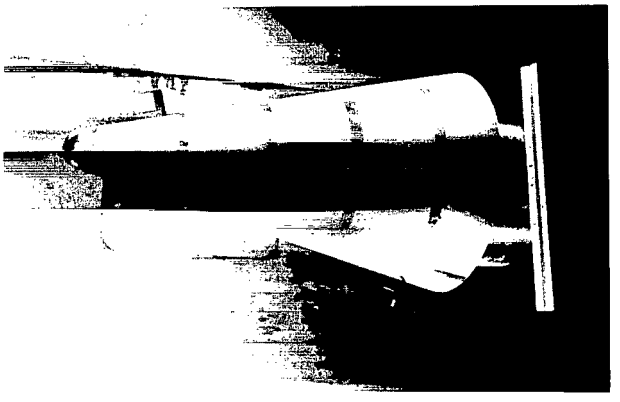

A-32127-11

(c) Movable probes installed on 15° model.

Figure 3.- Models installed in the 3.5-Foot Hypersonic Wind Tunnel.

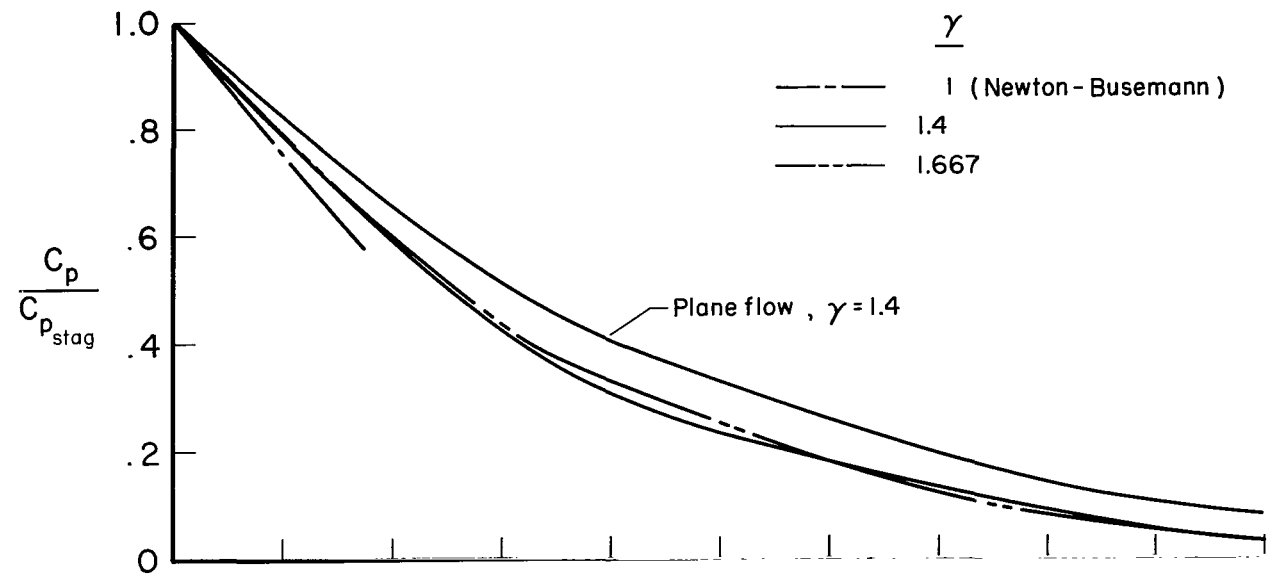

(a) $M_\infty = 10$

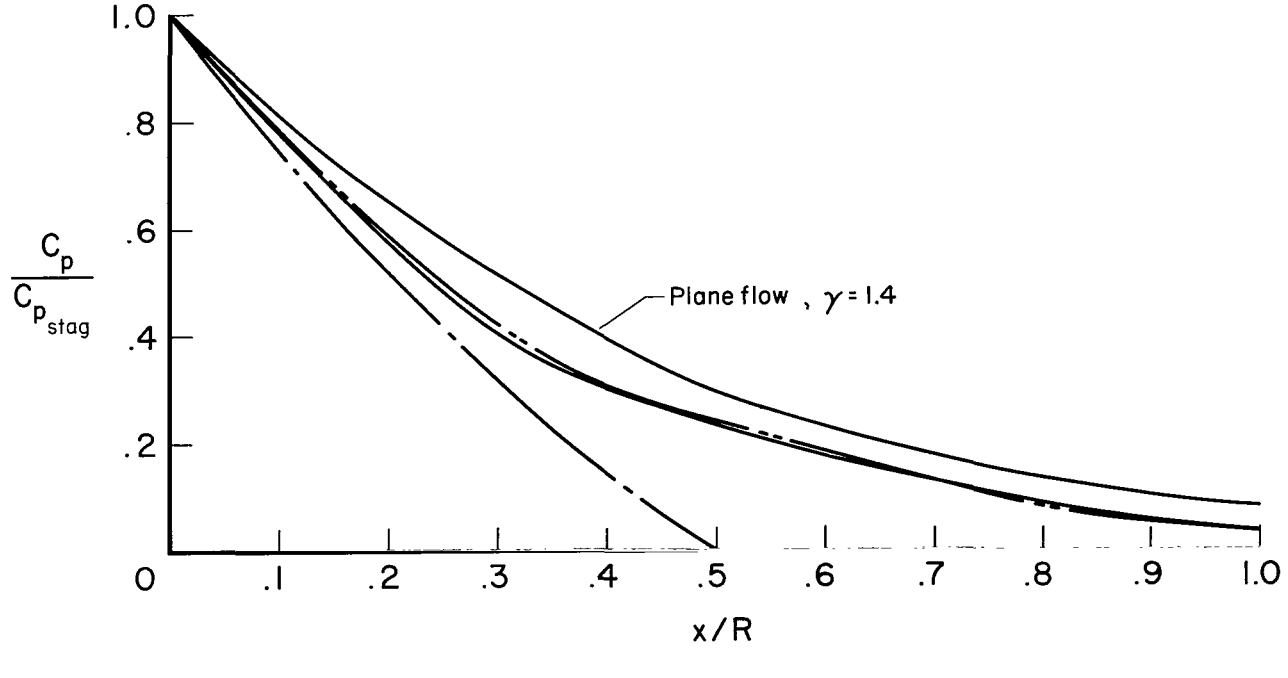

(b) $M_\infty = \infty$

Figure 4.- Theoretical pressure distribution over the hemisphere.

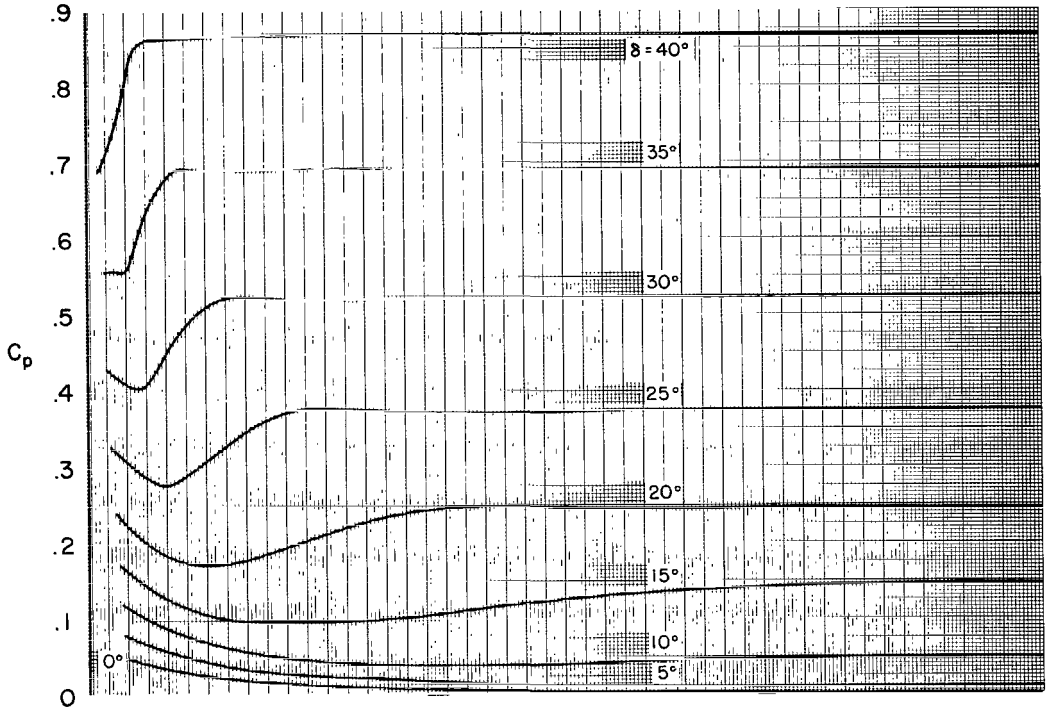

(a) $M_\infty = 10$

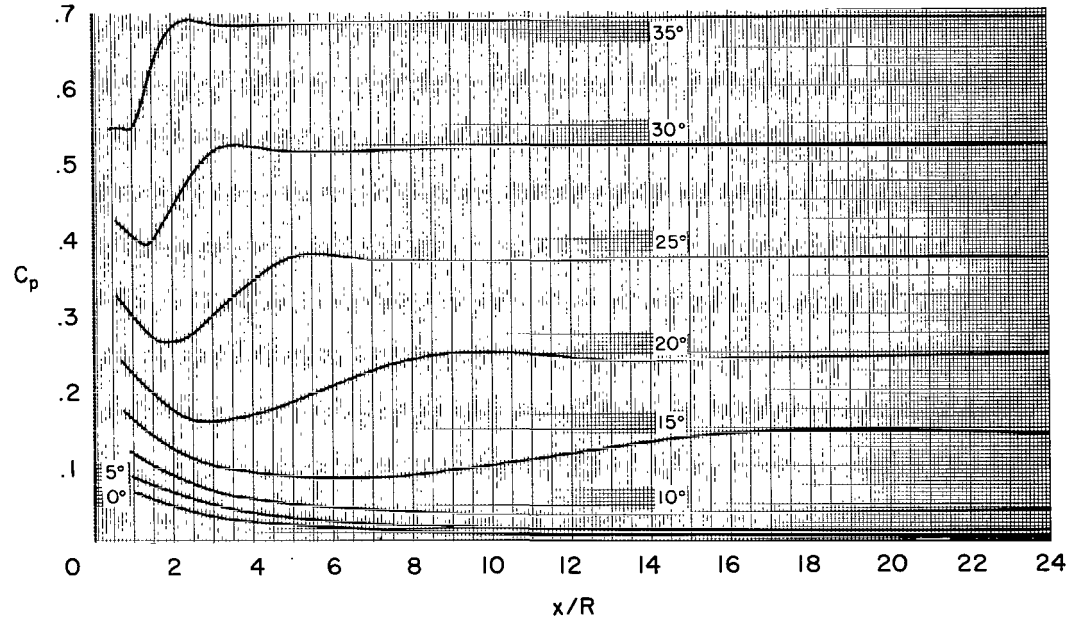

(b) $M_\infty = \infty$

Figure 5.- Theoretical pressure distribution over blunted cones for a specific-heat ratio of 1.4.

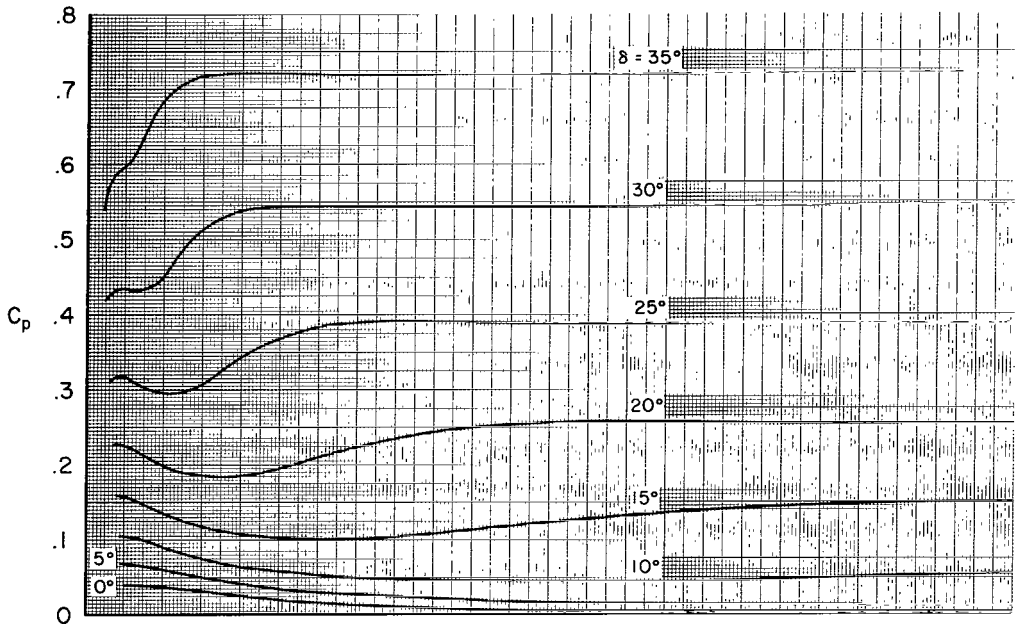

(a) $M_\infty = 10$

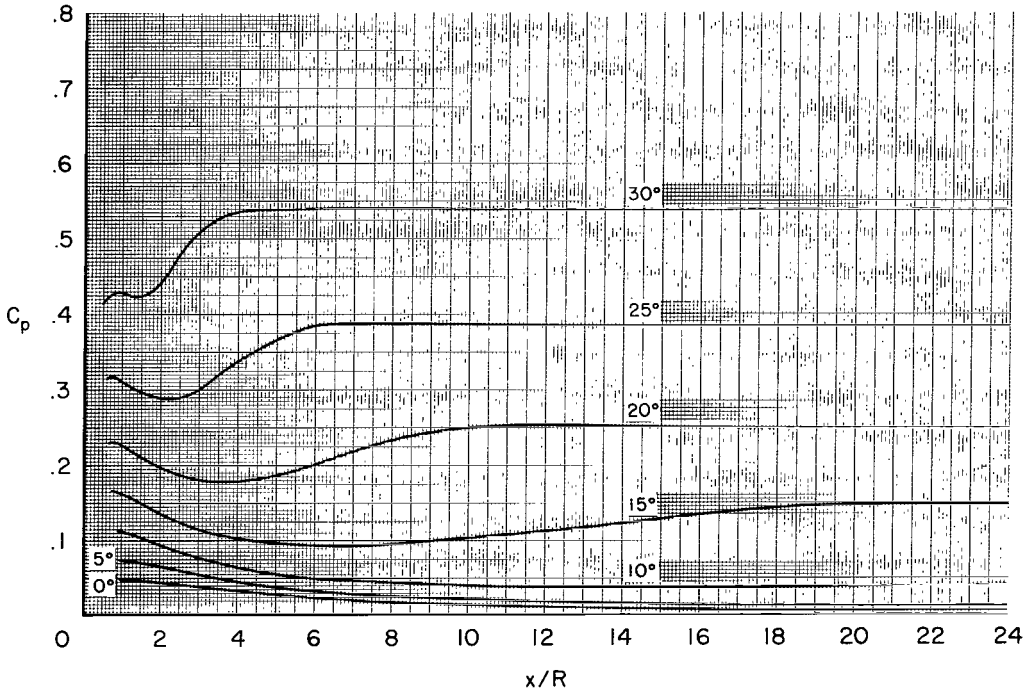

(b) $M_\infty = \infty$

Figure 6.- Theoretical pressure distribution over blunted cones for a specific-heat ratio of 1.667.

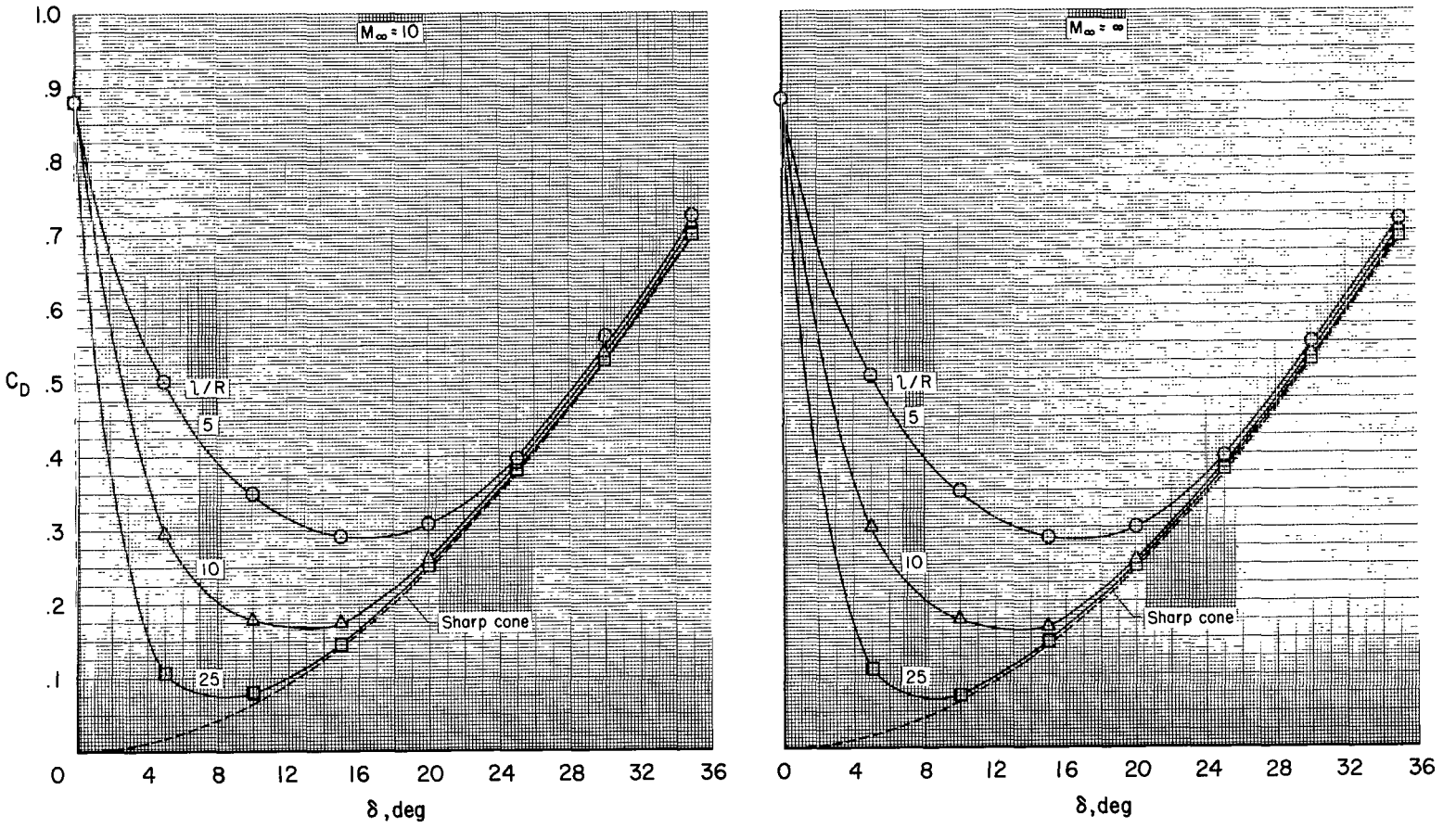

Figure 7.- Theoretical pressure drag of blunted cones for a specific-heat ratio of 1.4, $\alpha = 0^\circ$.

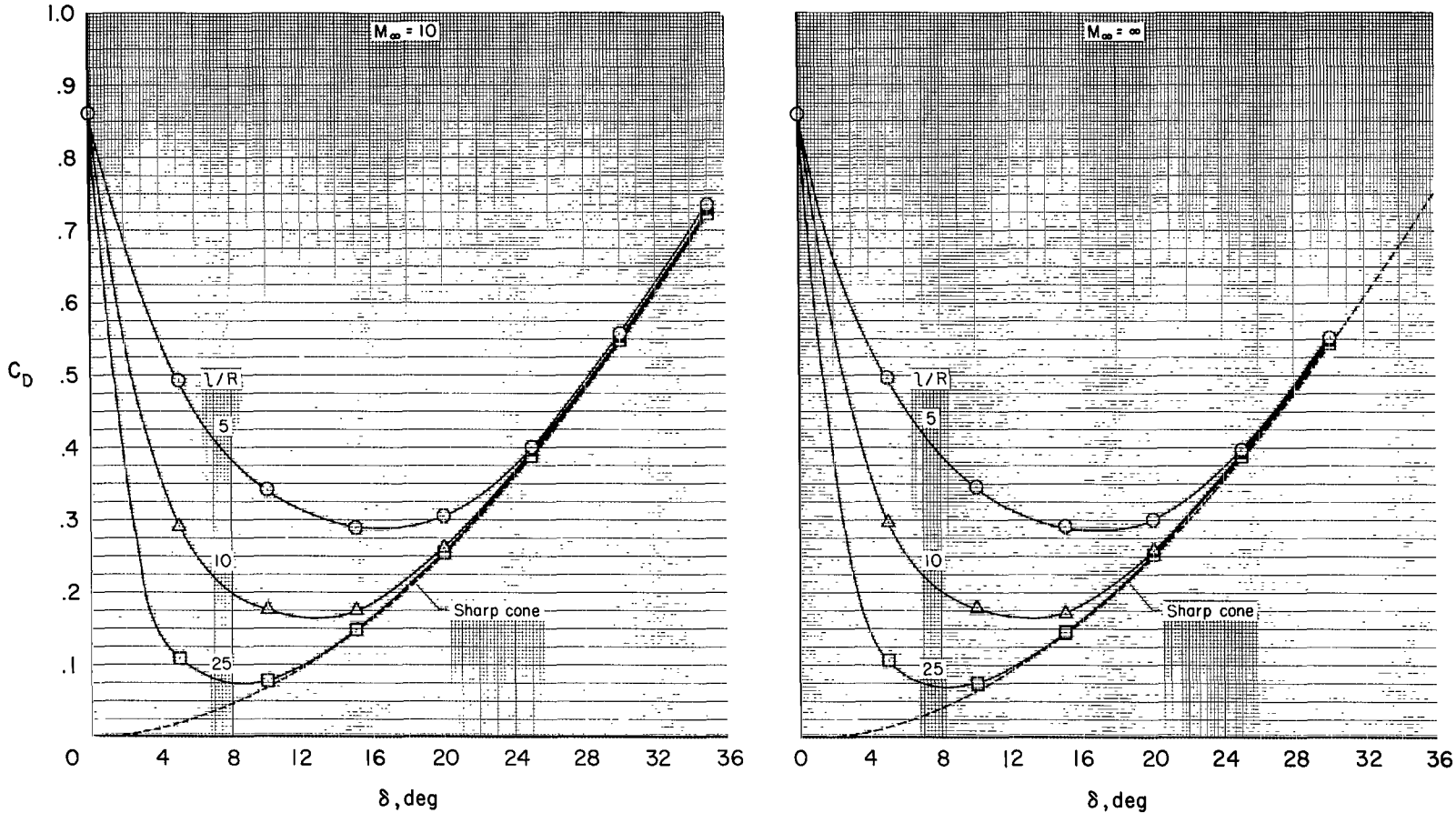

Figure 8.- Theoretical pressure drag of blunted cones for a specific-heat ratio of 1.667, $\alpha = 0^\circ$.

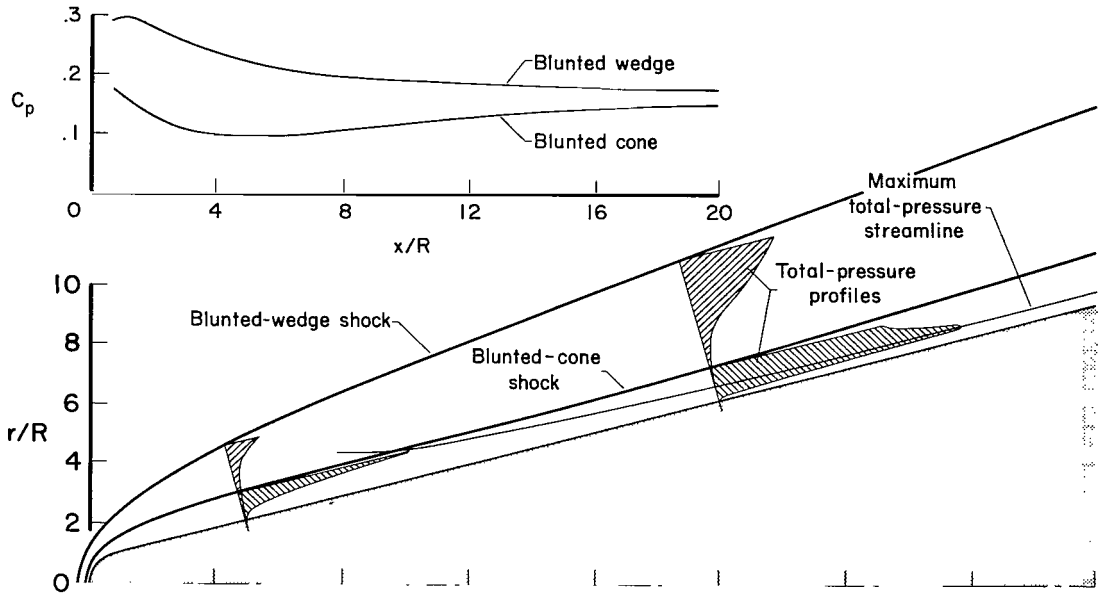

(a) $M_\infty = 10$, $\gamma = 1.4$

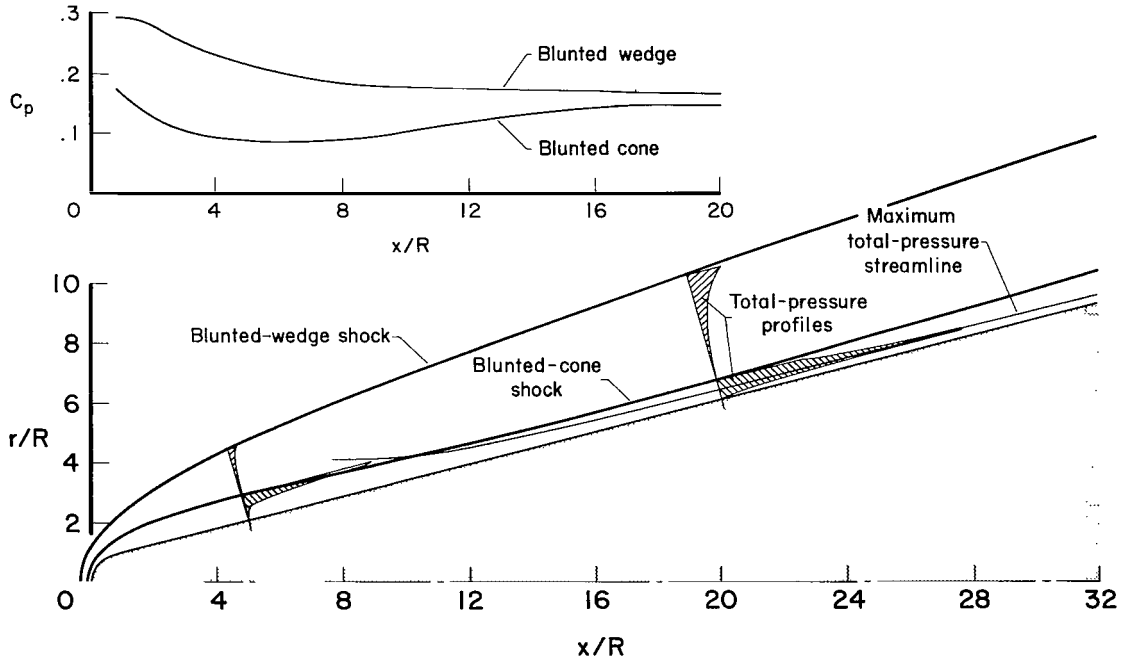

(b) $M_\infty = \infty$, $\gamma = 1.4$

Figure 9.- Comparison of the flows of geometrically similar 15° half-angle blunted cone and wedge.

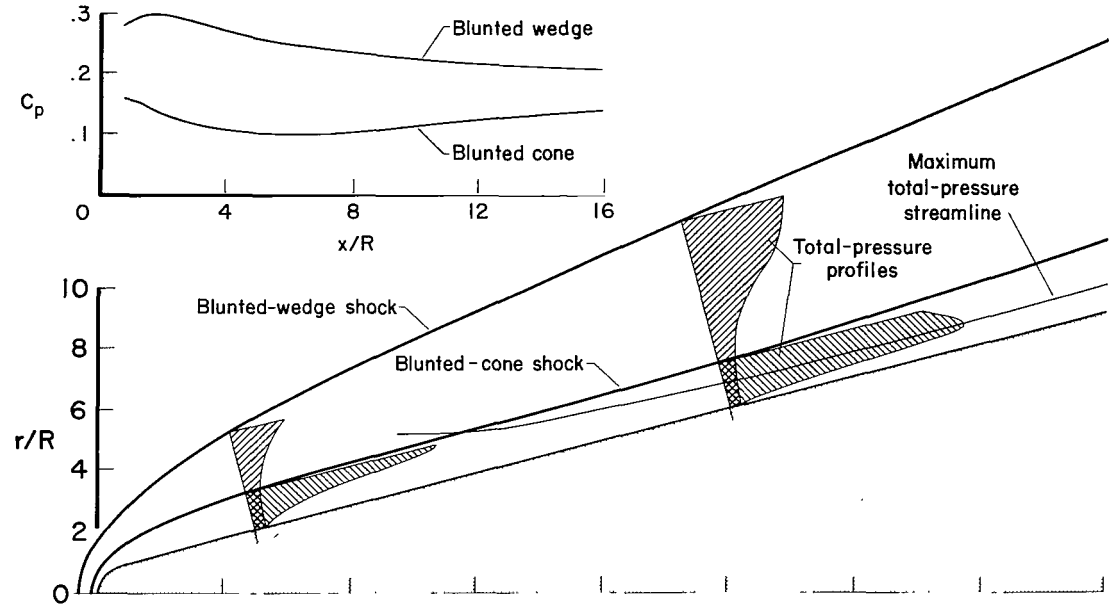

(c) $M_\infty = 10$, $\gamma = 1.667$

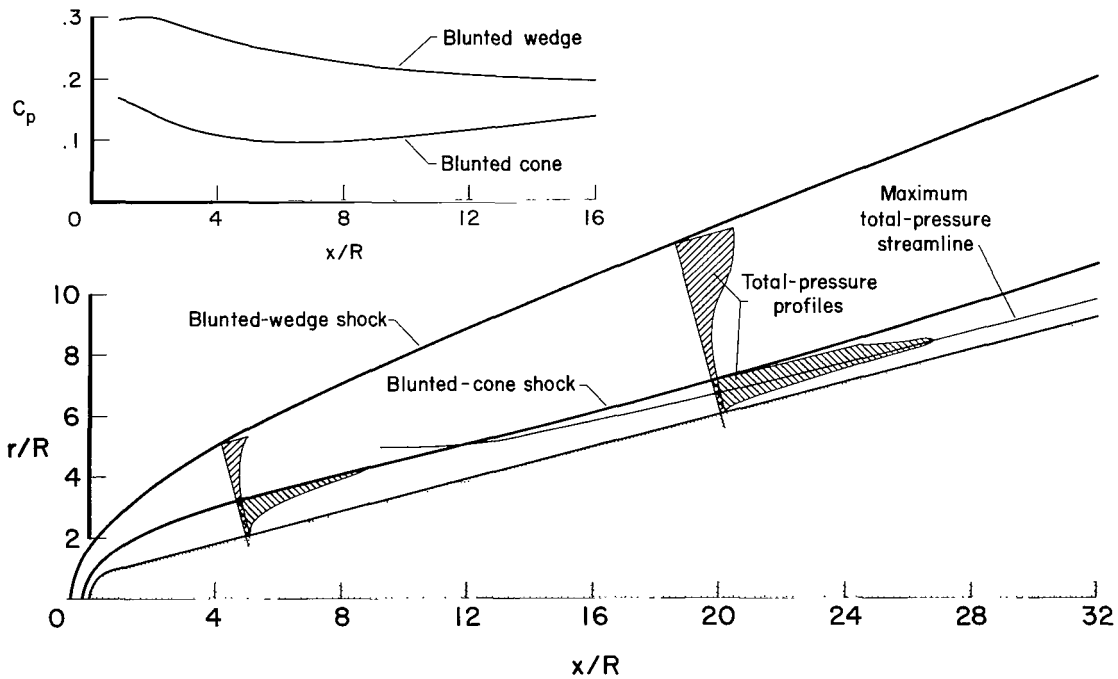

(d) $M_\infty = \infty$, $\gamma = 1.667$

Figure 9.- Concluded.

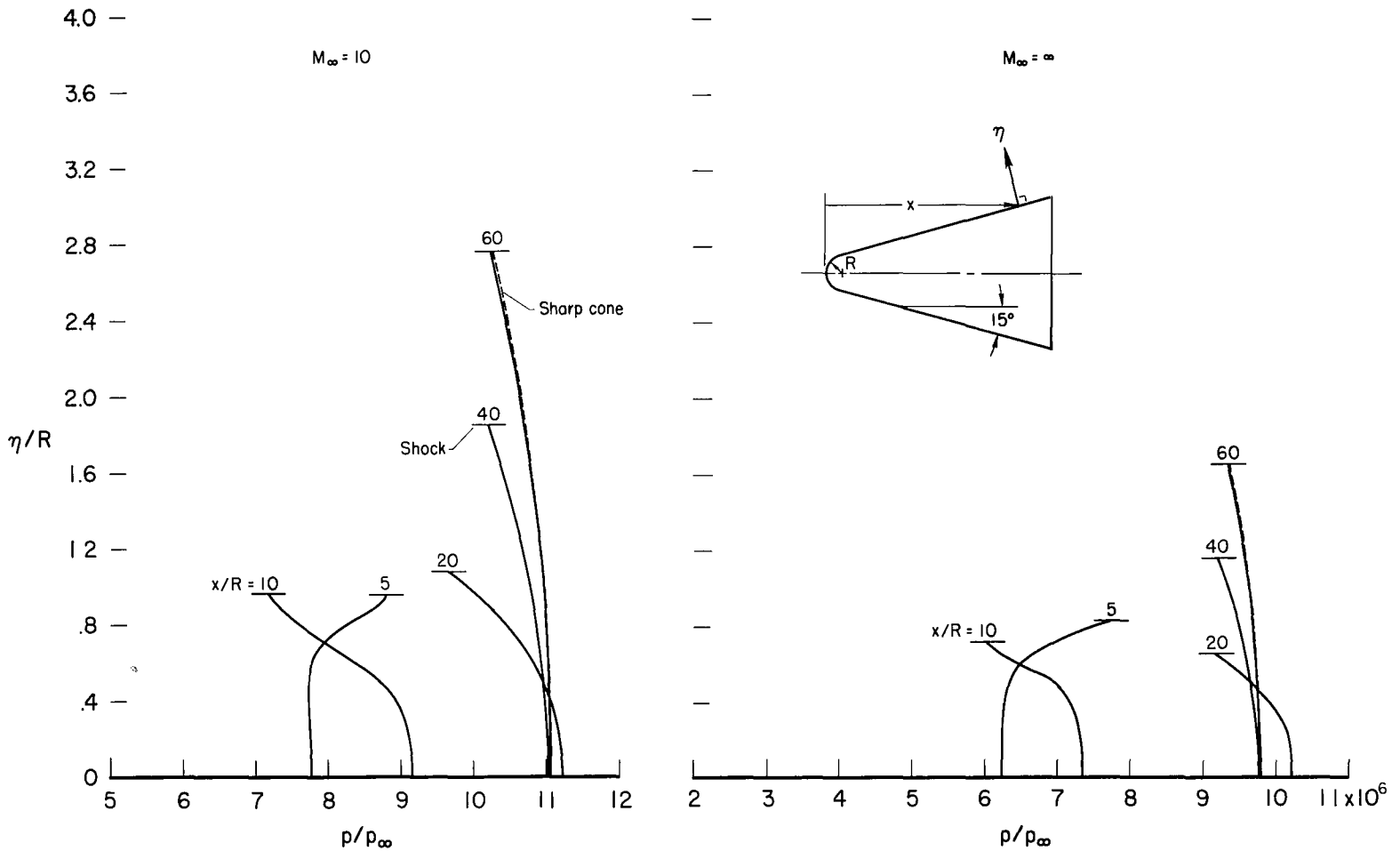

(a) Static-pressure ratio.

Figure 10.- Shock-layer properties of a 15° half-angle blunted cone, $\gamma = 1.4$.

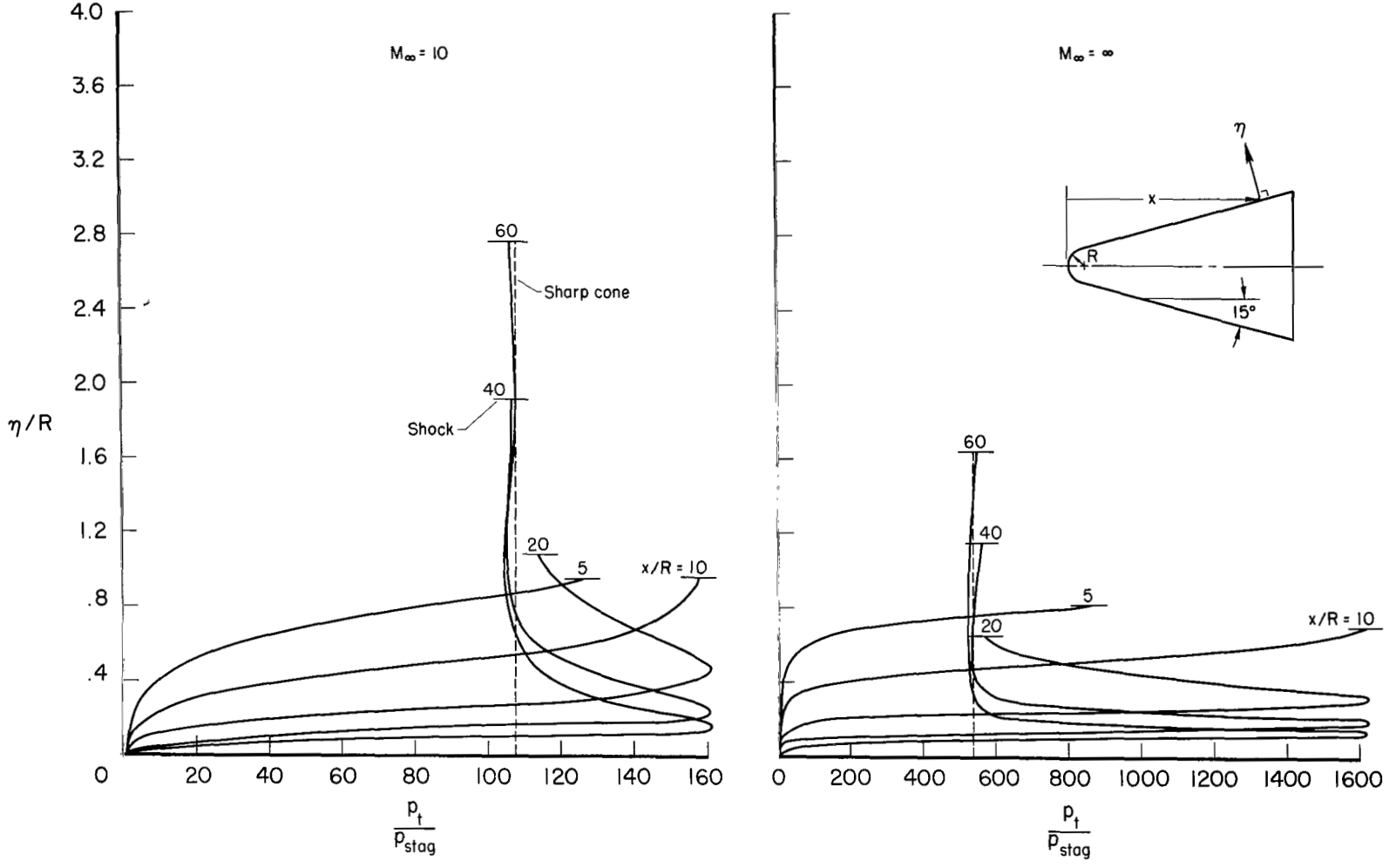

(b) Total-pressure ratio.

Figure 10.- Continued.

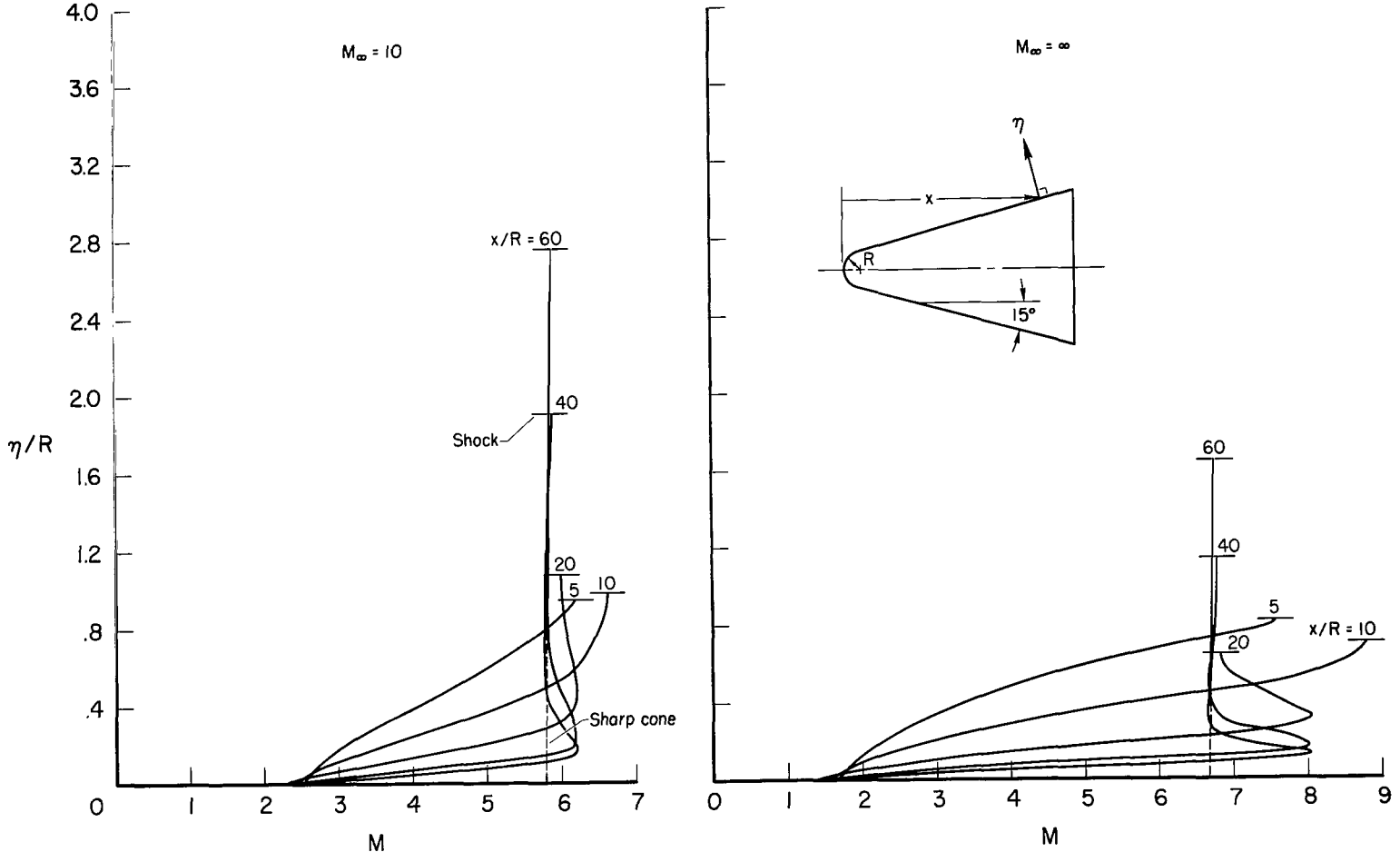

(c) Local Mach number.

Figure 10.- Continued.

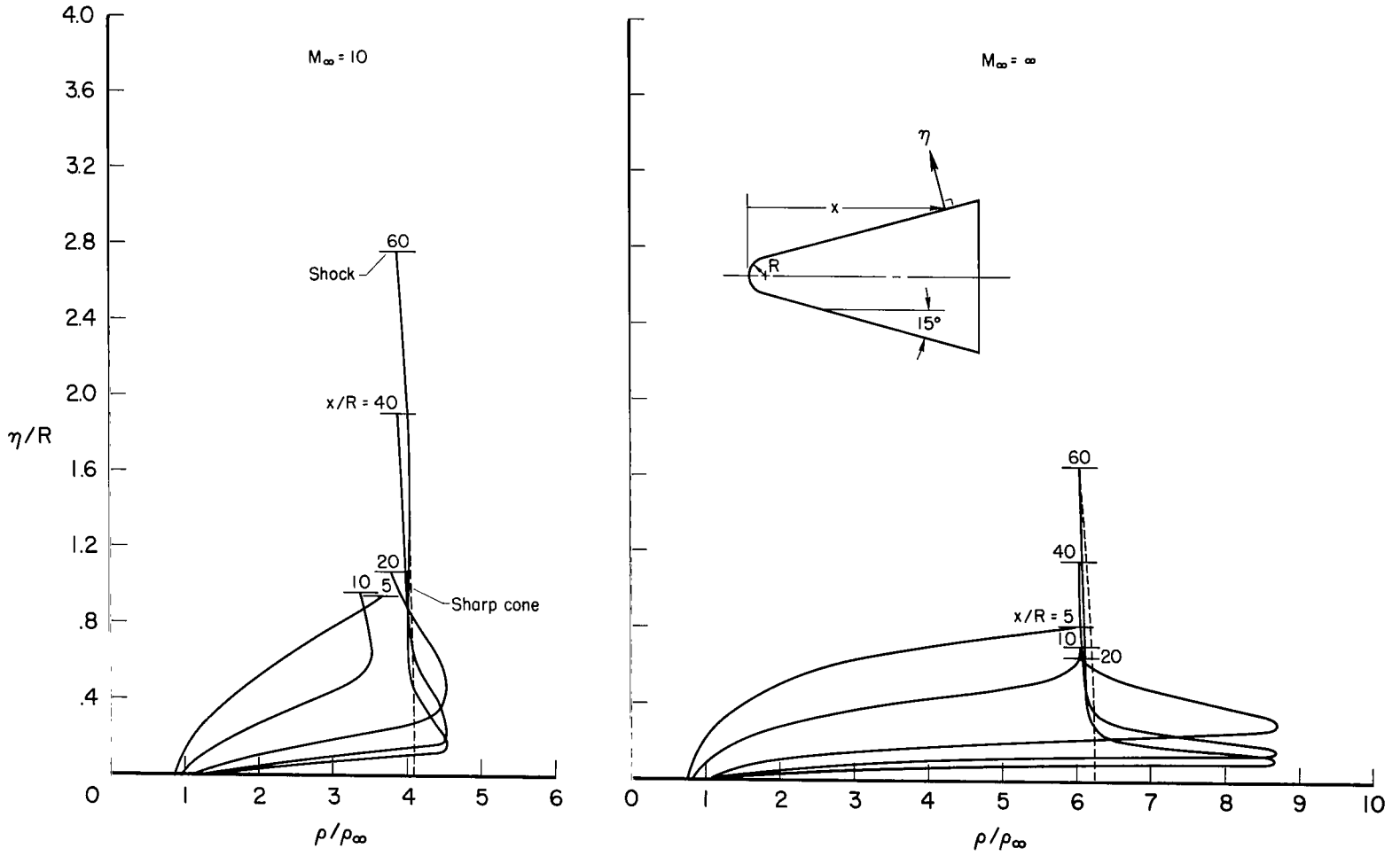

(d) Density ratio.

Figure 10.- Continued.

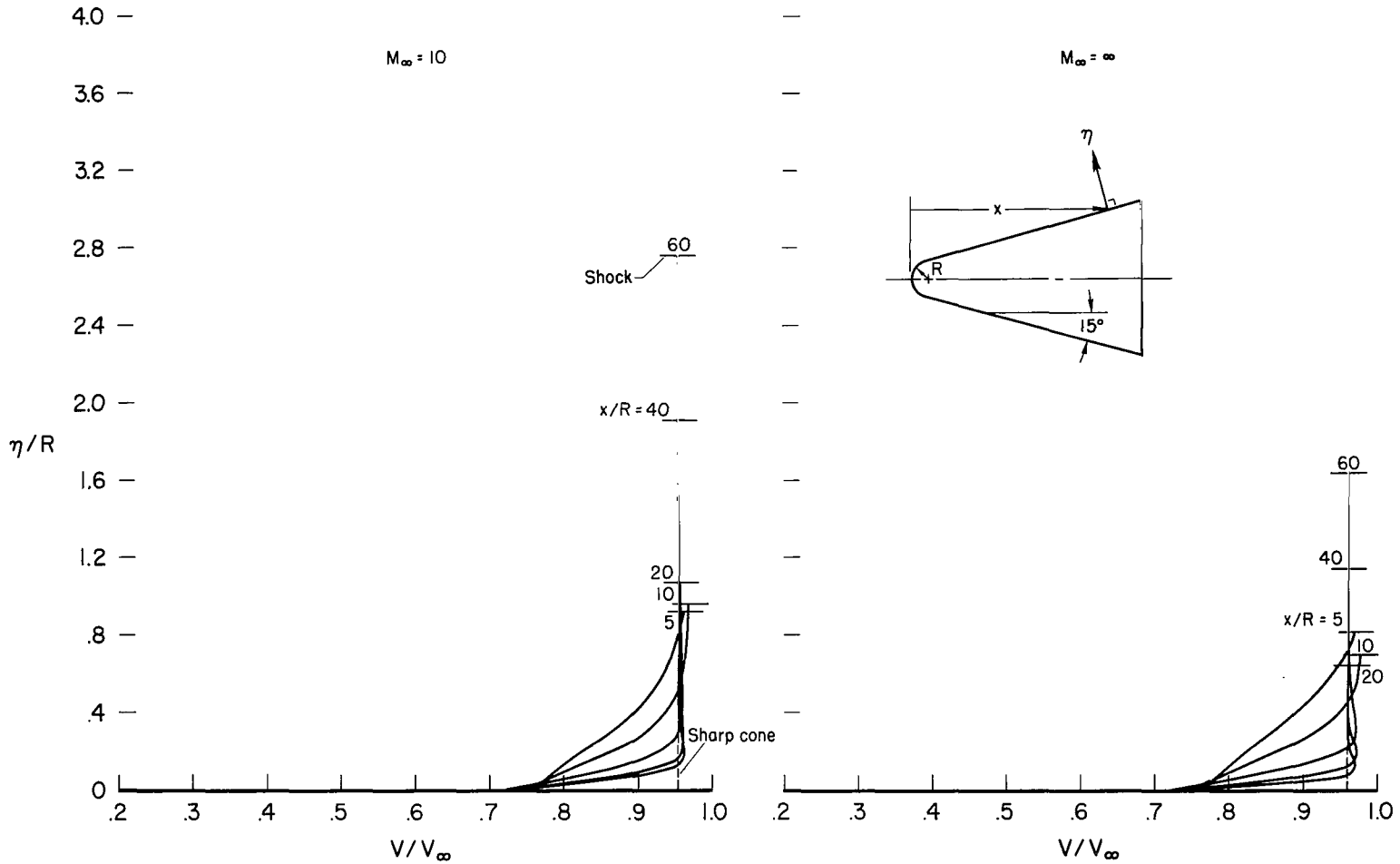

(e) Velocity ratio.

Figure 10.- Continued.

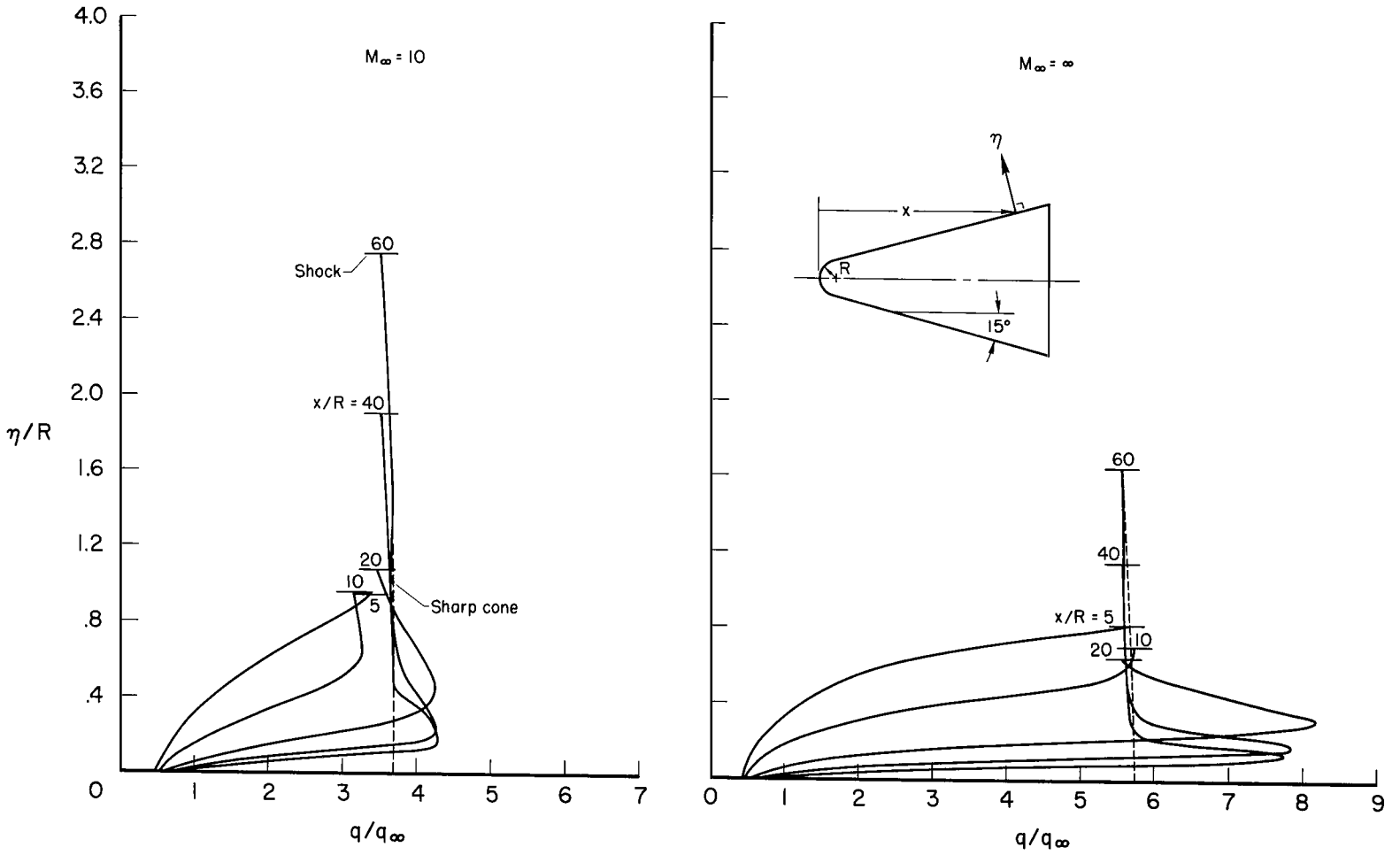

(f) Dynamic-pressure ratio.

Figure 10.- Concluded.

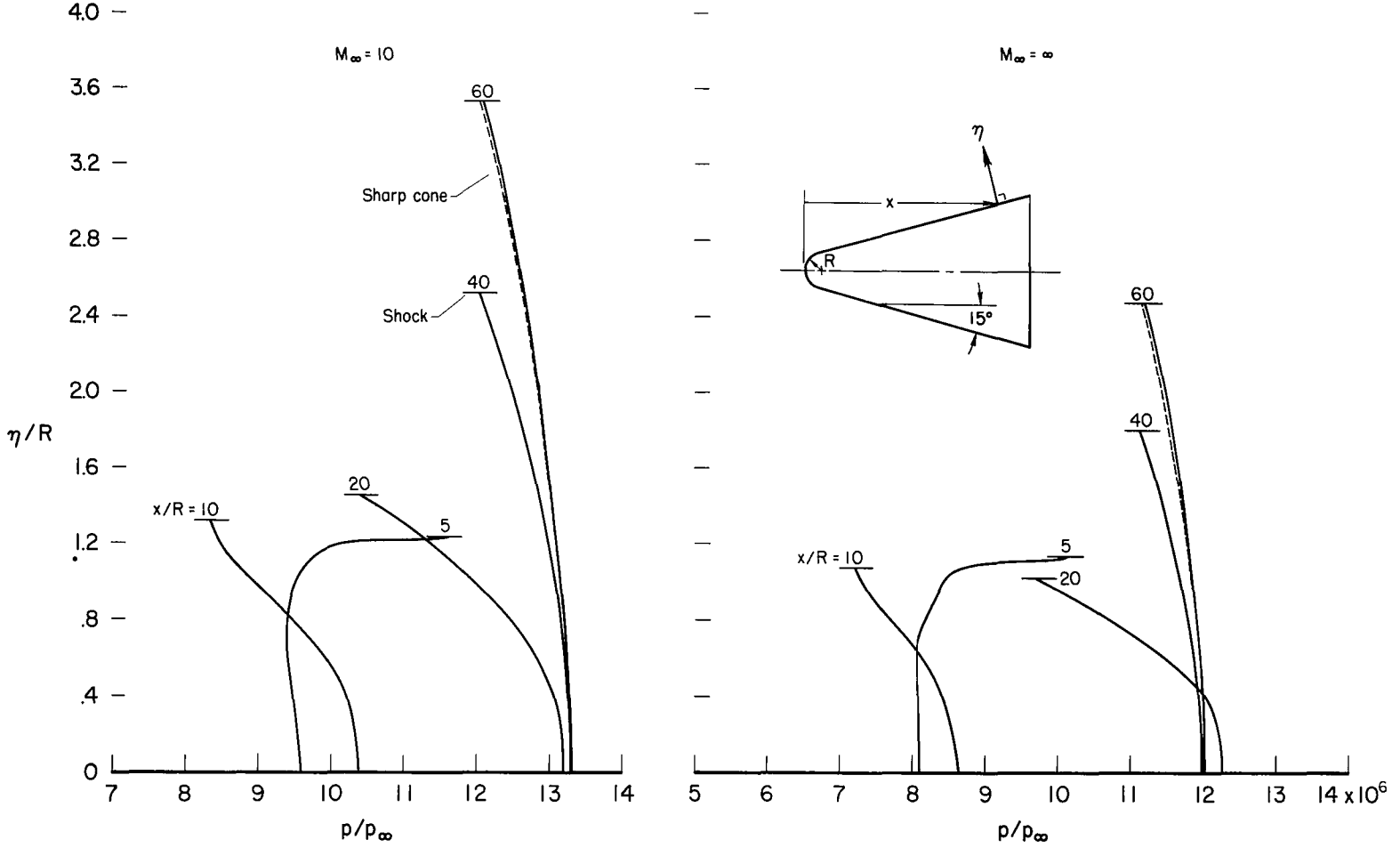

(a) Static-pressure ratio.

Figure 11.- Shock-layer properties of a 15° half-angle blunted cone, $\gamma = 1.667$.

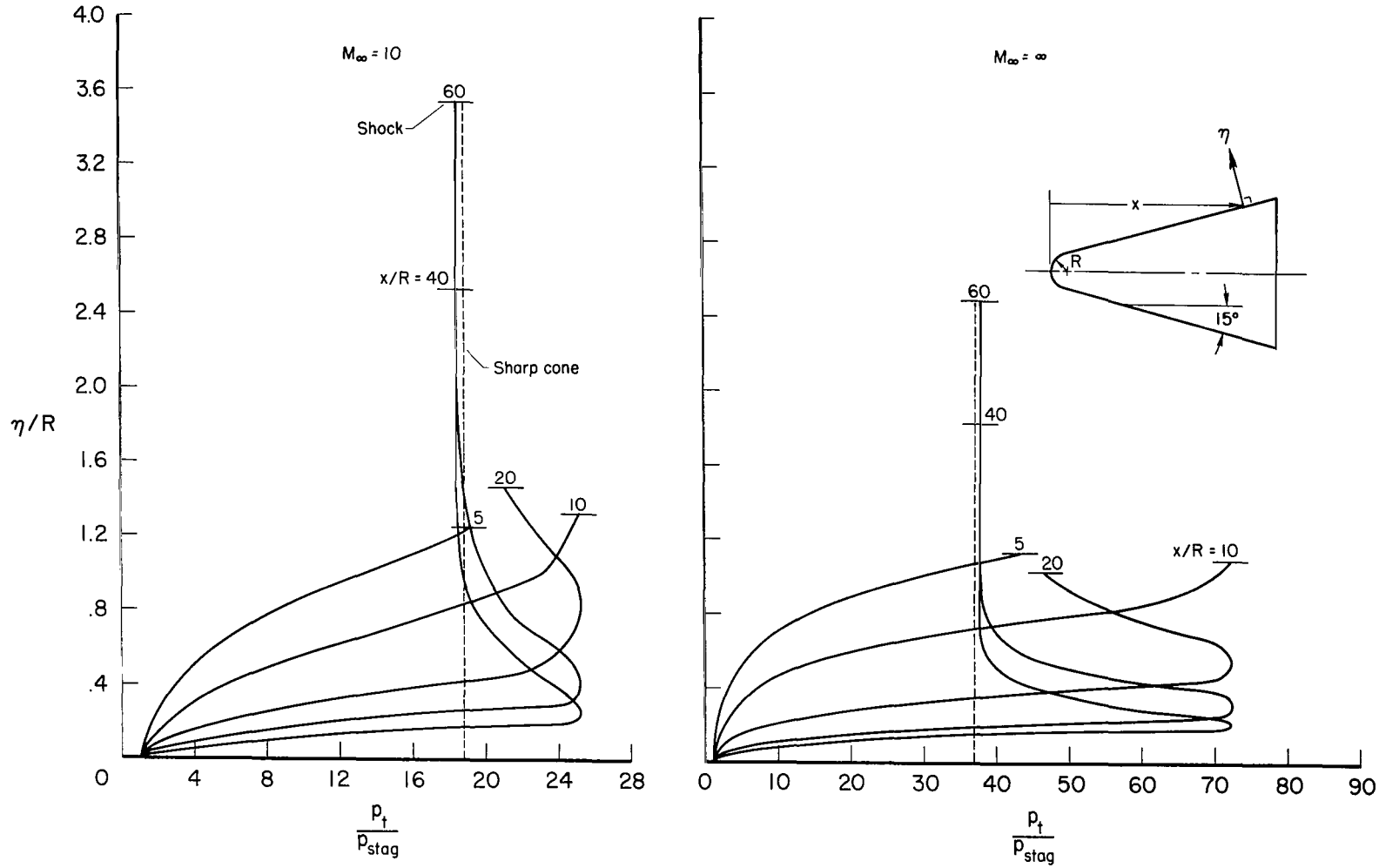

(b) Total-pressure ratio.

Figure 11.- Continued.

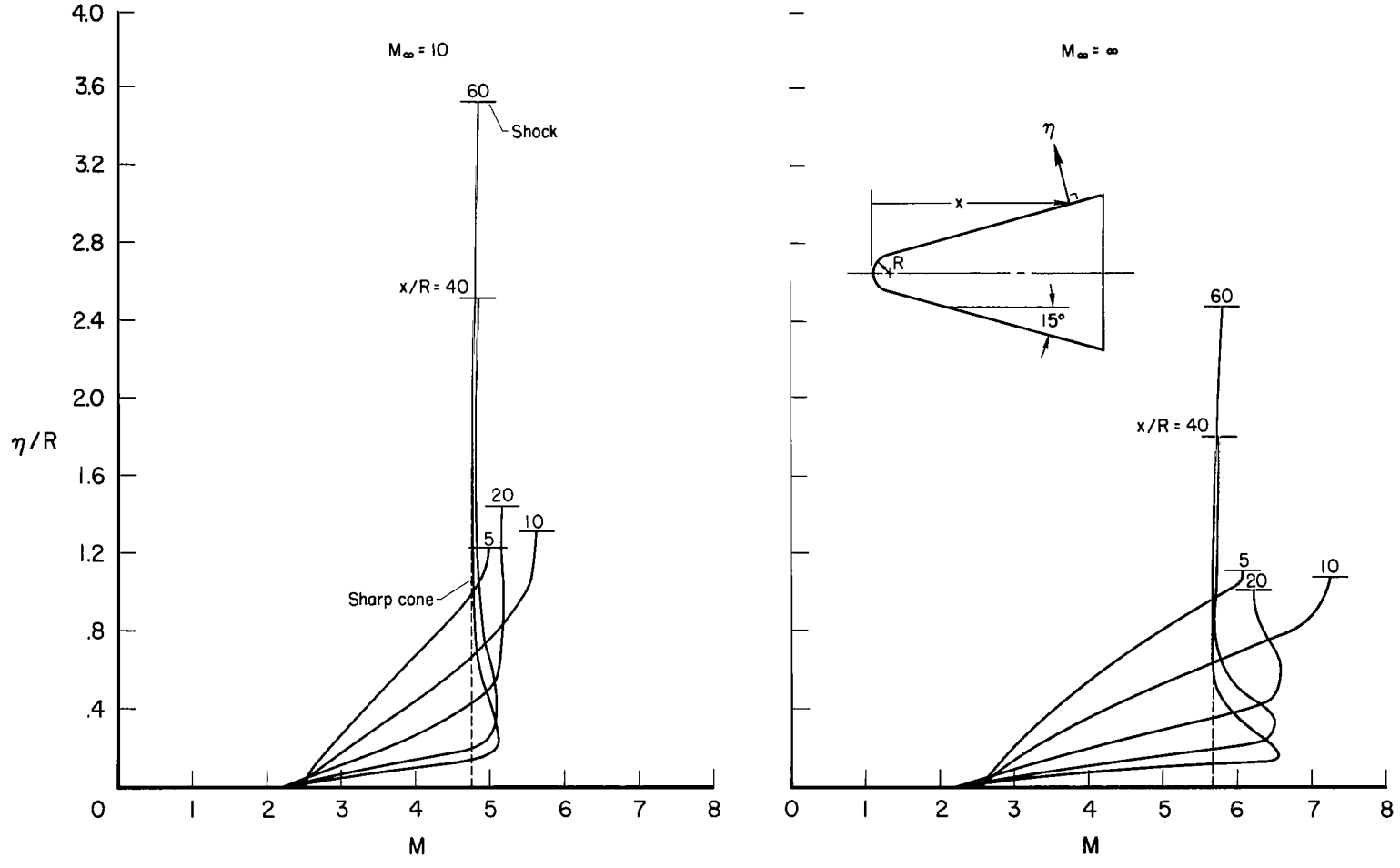

(c) Local Mach number.

Figure 11.- Continued.

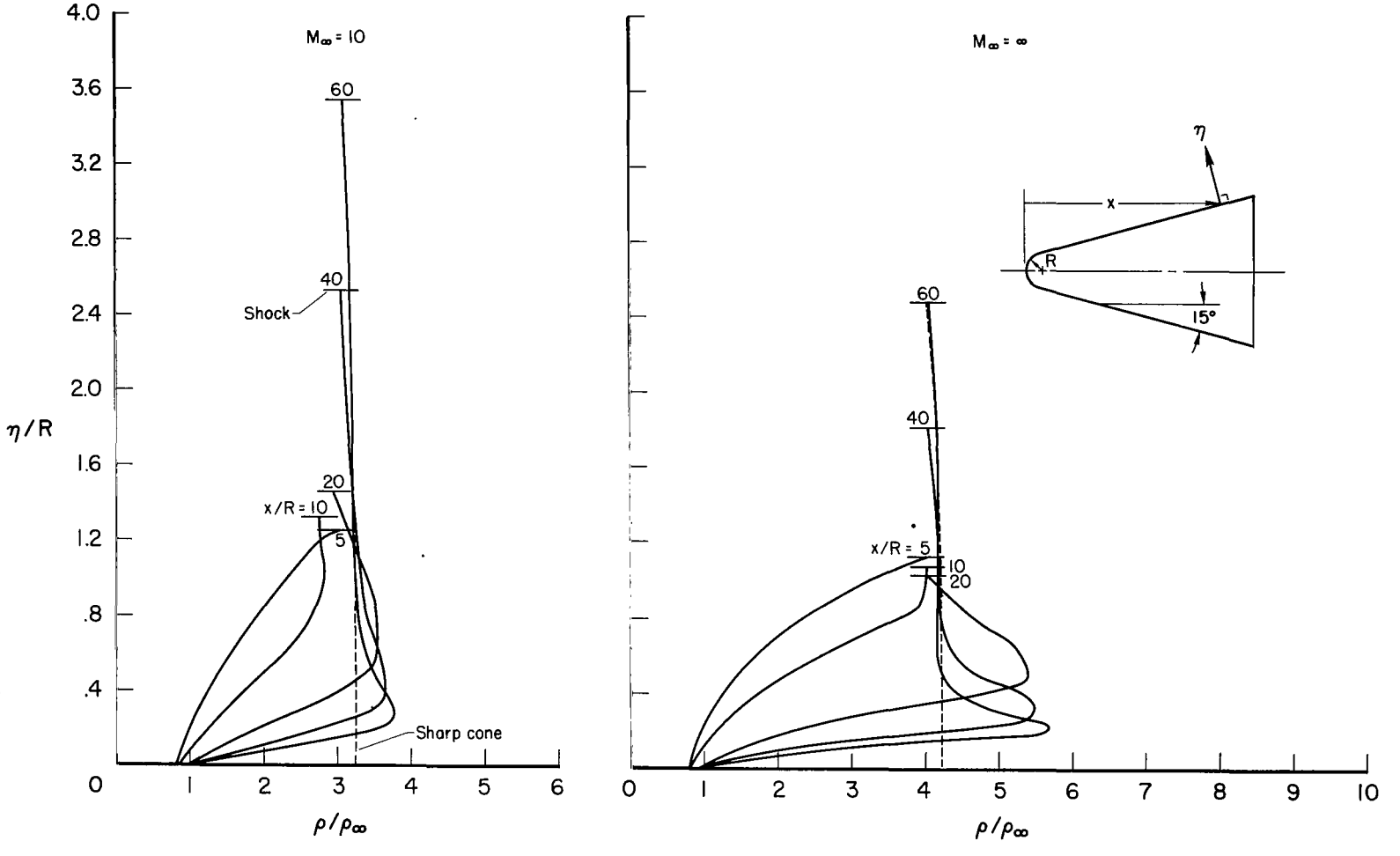

(d) Density ratio.

Figure 11.- Continued.

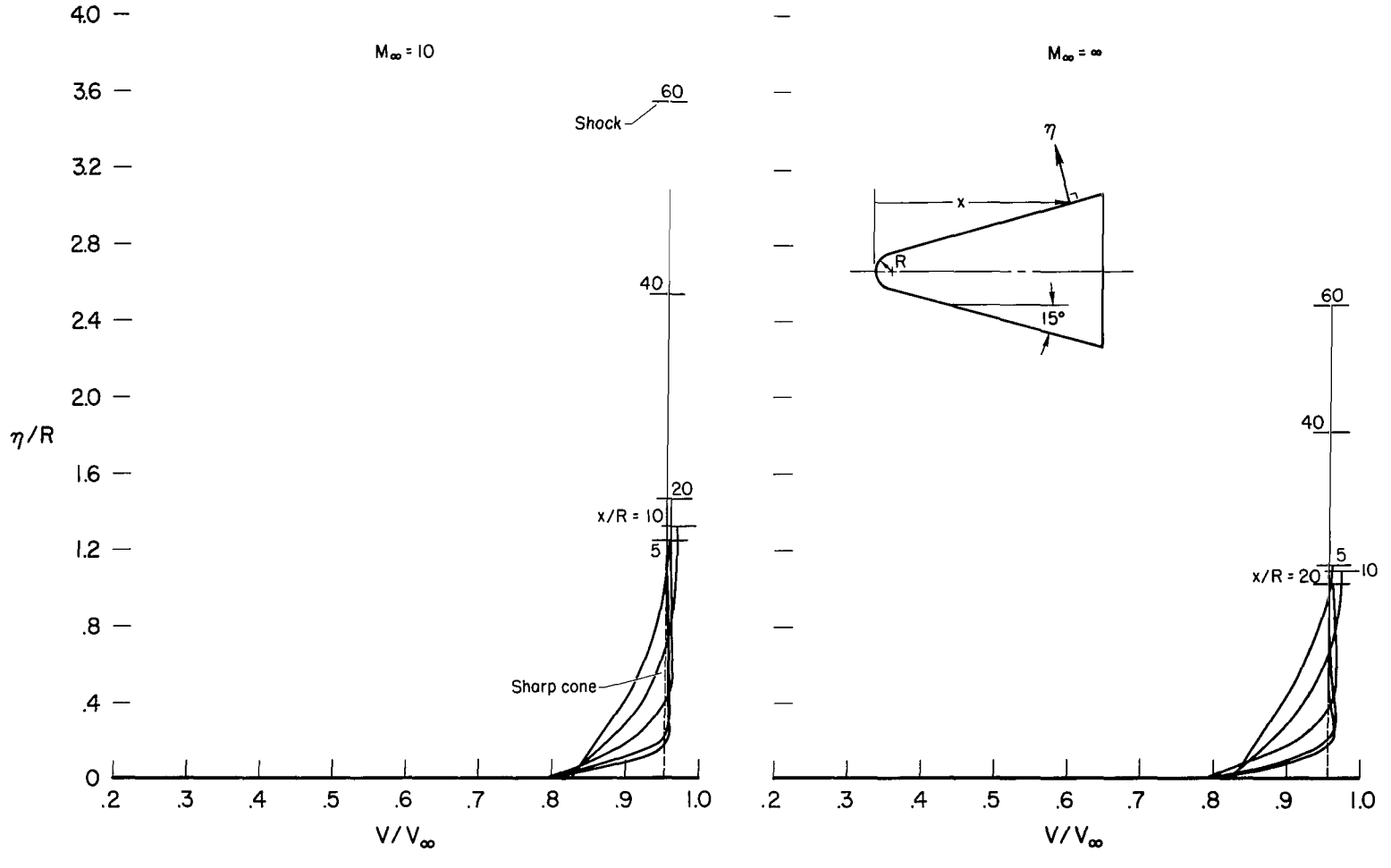

(e) Velocity ratio.

Figure 11.- Continued.

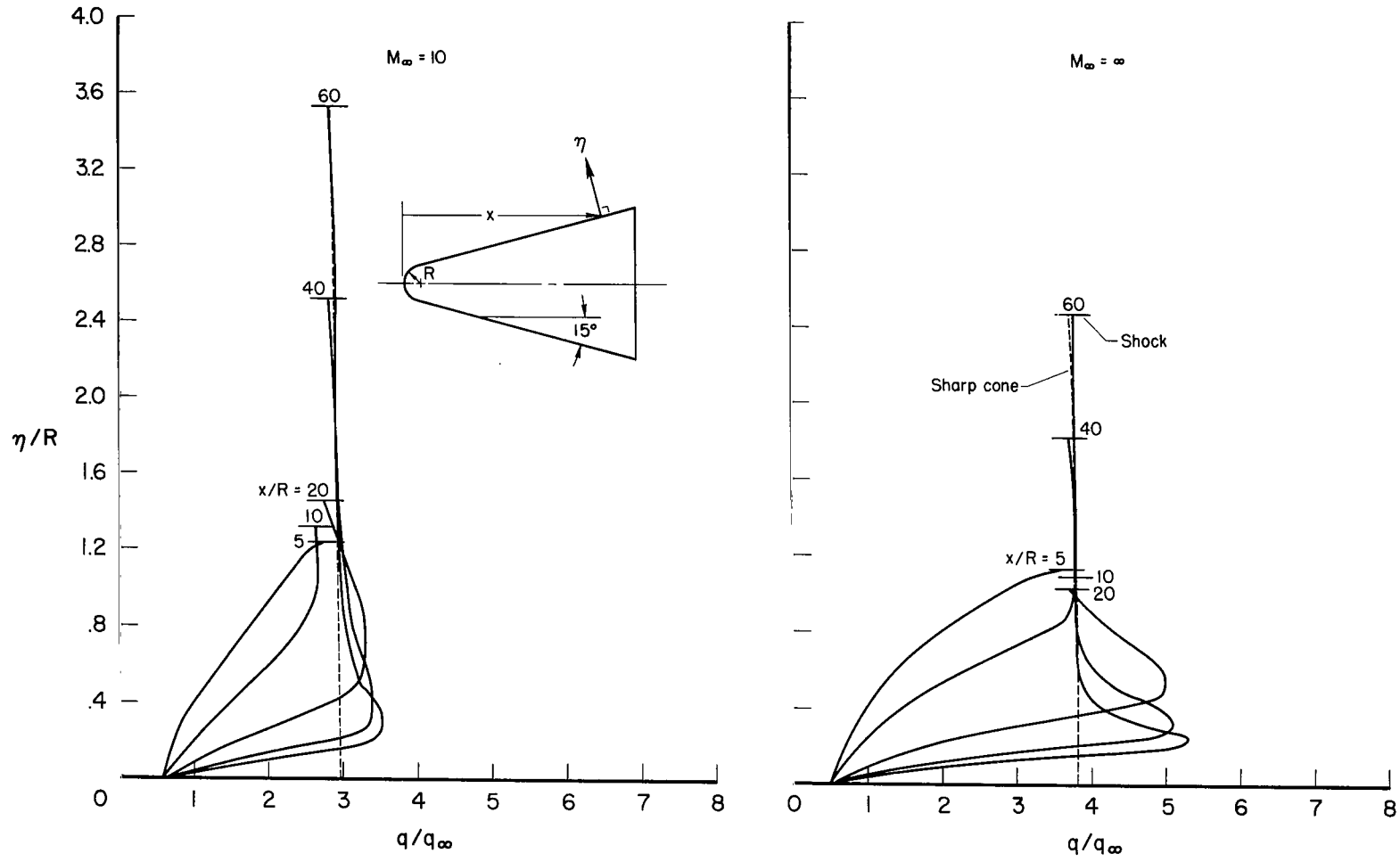

(f) Dynamic-pressure ratio.

Figure 11.- Concluded.

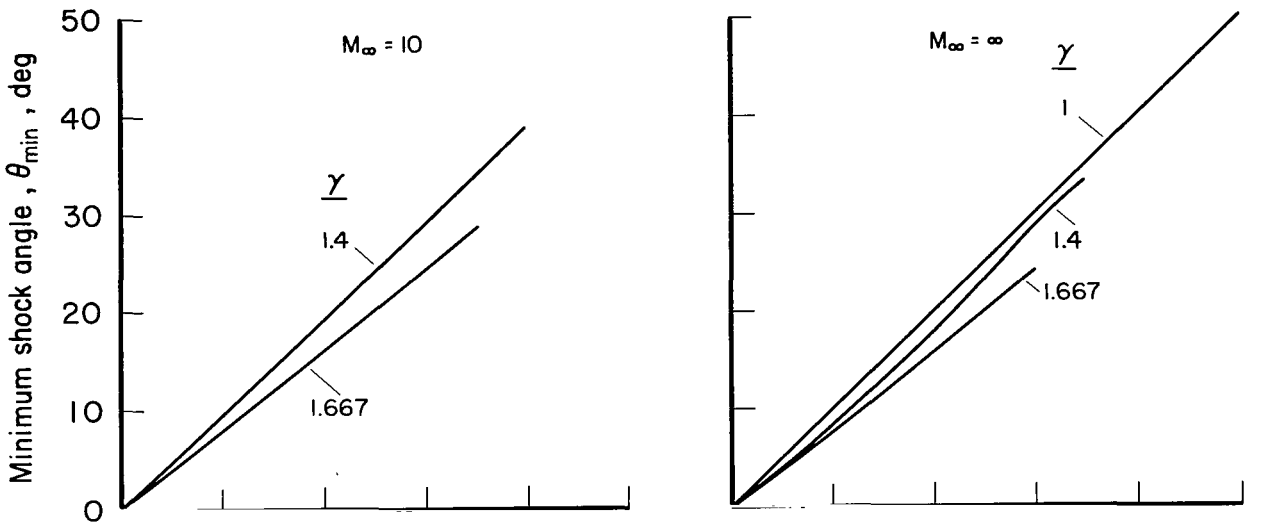

(a) Minimum shock angle.

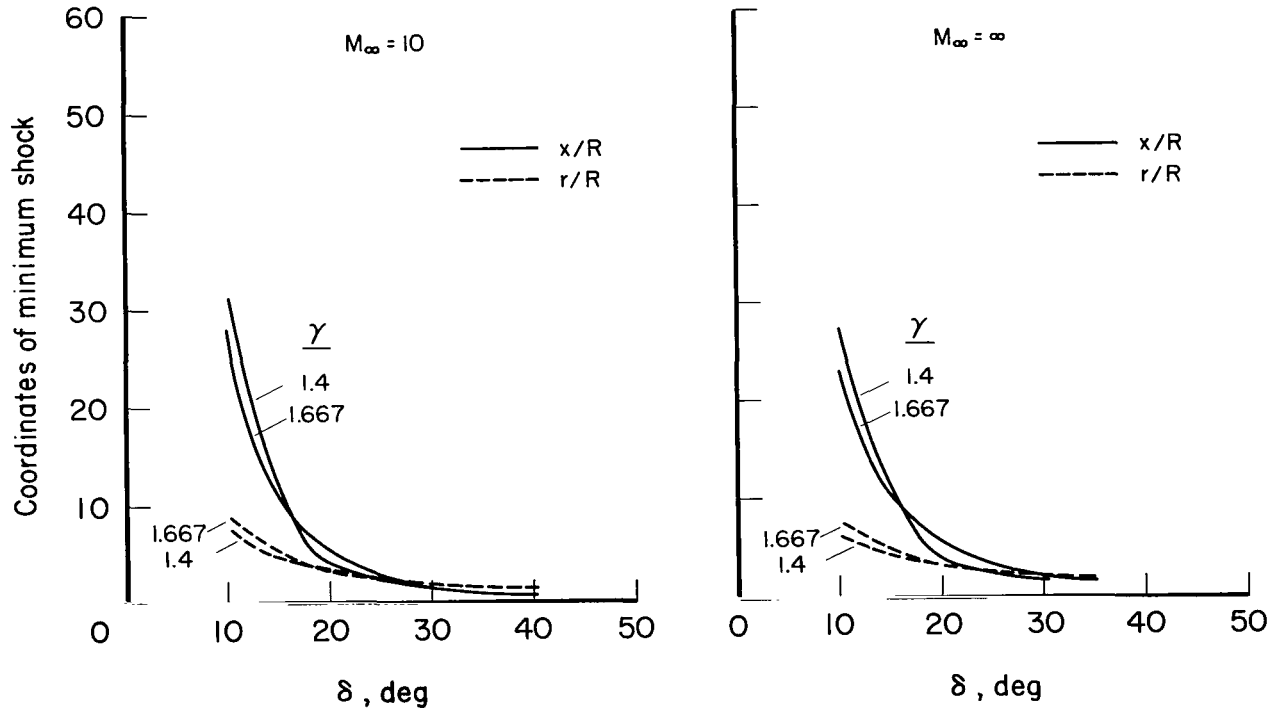

(b) Coordinates where the shock angle is minimum.

Figure 12.- Characteristics of the minimum shock angles for blunted cones.

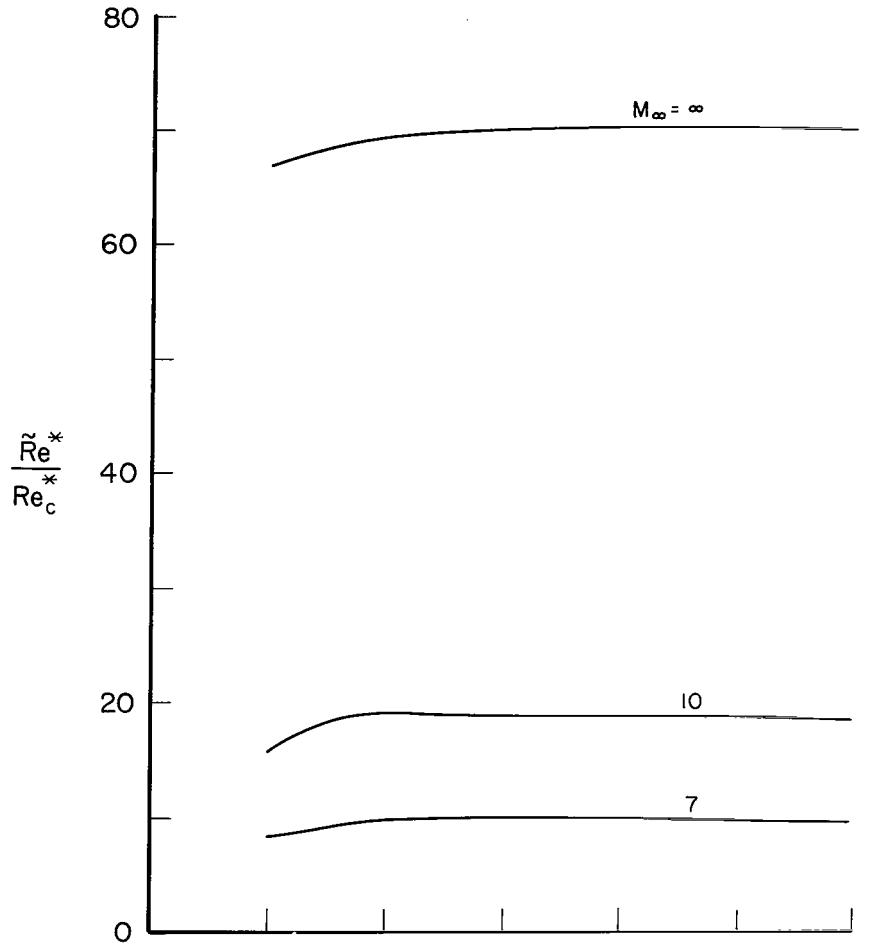

(a) $\delta = 15^\circ$

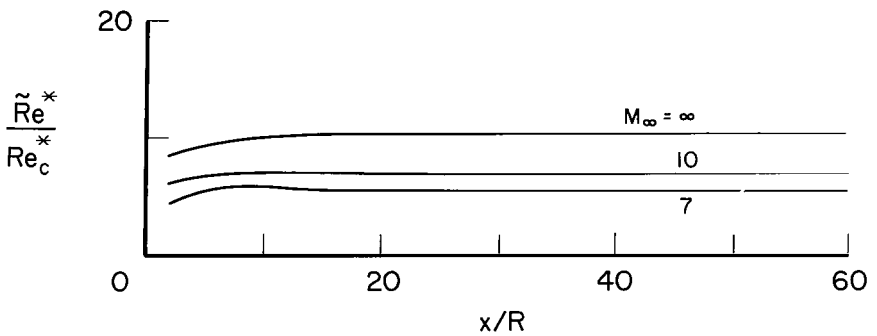

(b) $\delta = 30^\circ$

Figure 13.- Ratio of Reynolds number per foot for the maximum total pressure streamline to the Reynolds number per foot along the surface for blunted cones, $\gamma = 1.4$.

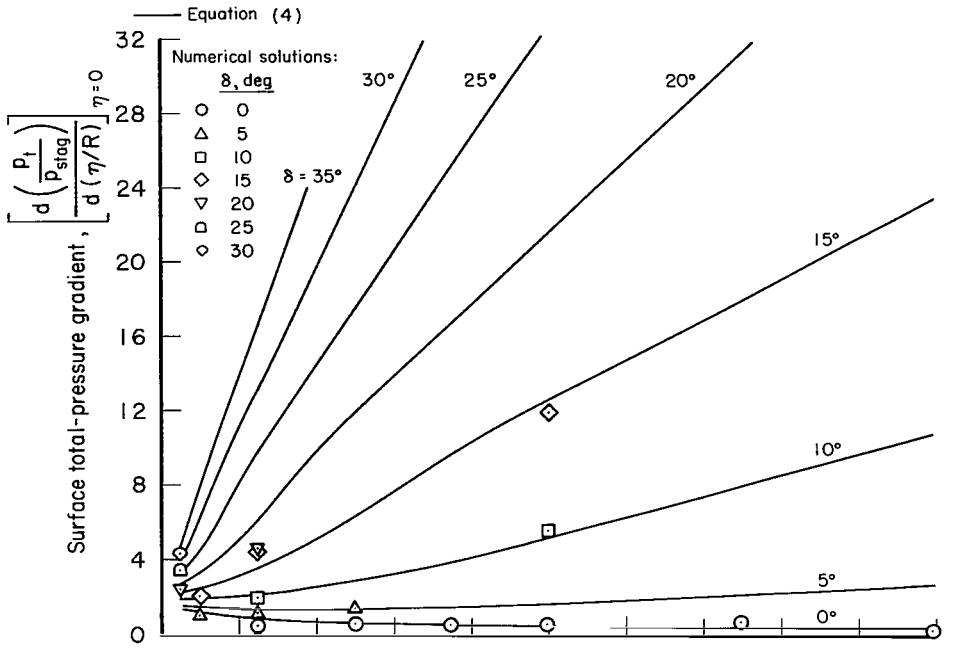

(a) $M_\infty = 10$

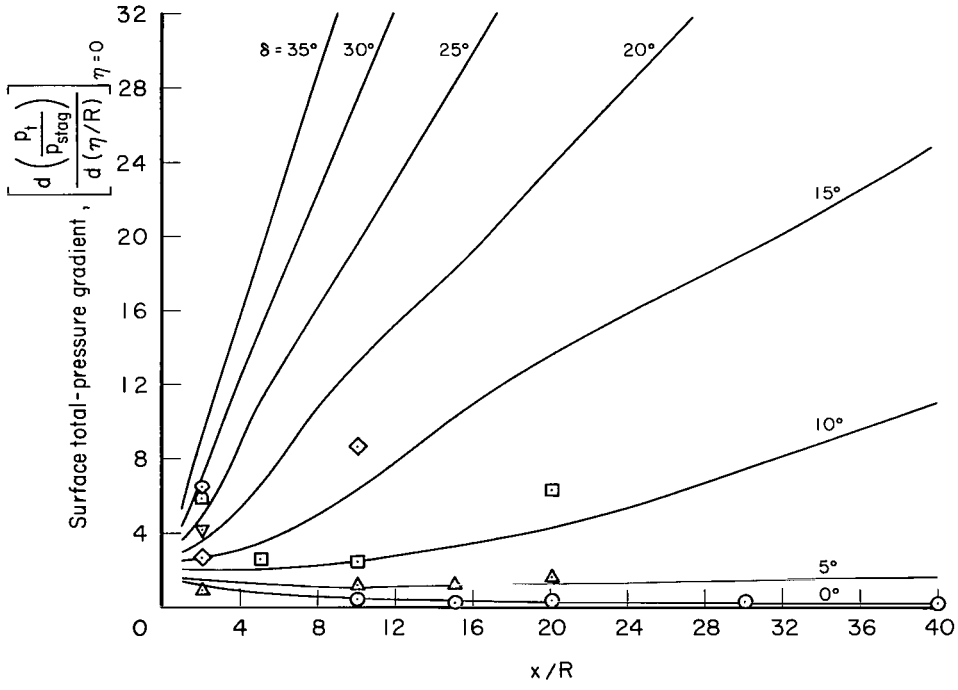

(b) $M_\infty = \infty$

Figure 14.- Total-pressure gradient at surface of blunted-cone flows for a specific-heat ratio of 1.4.

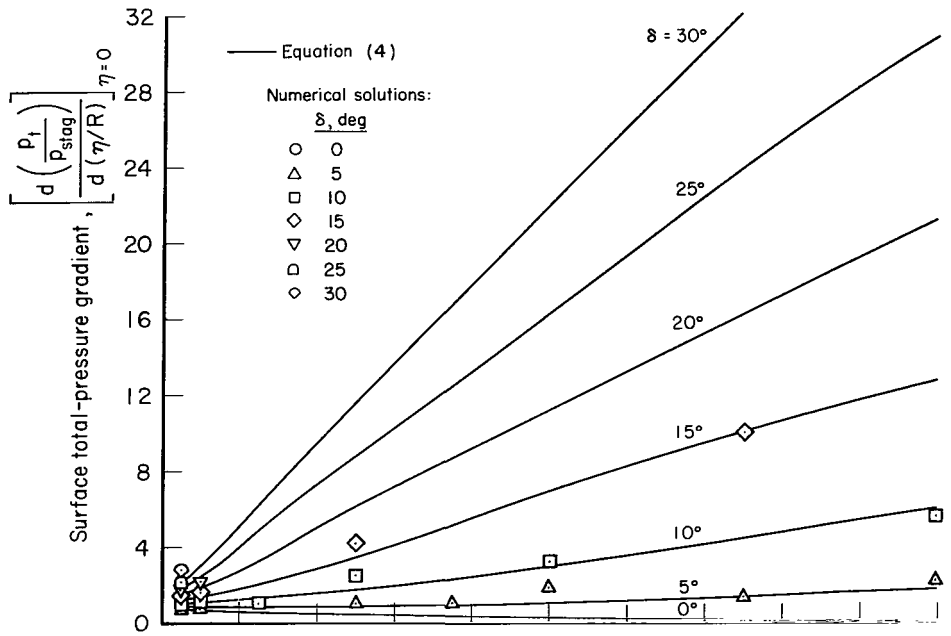

(a) $M_\infty = 10$

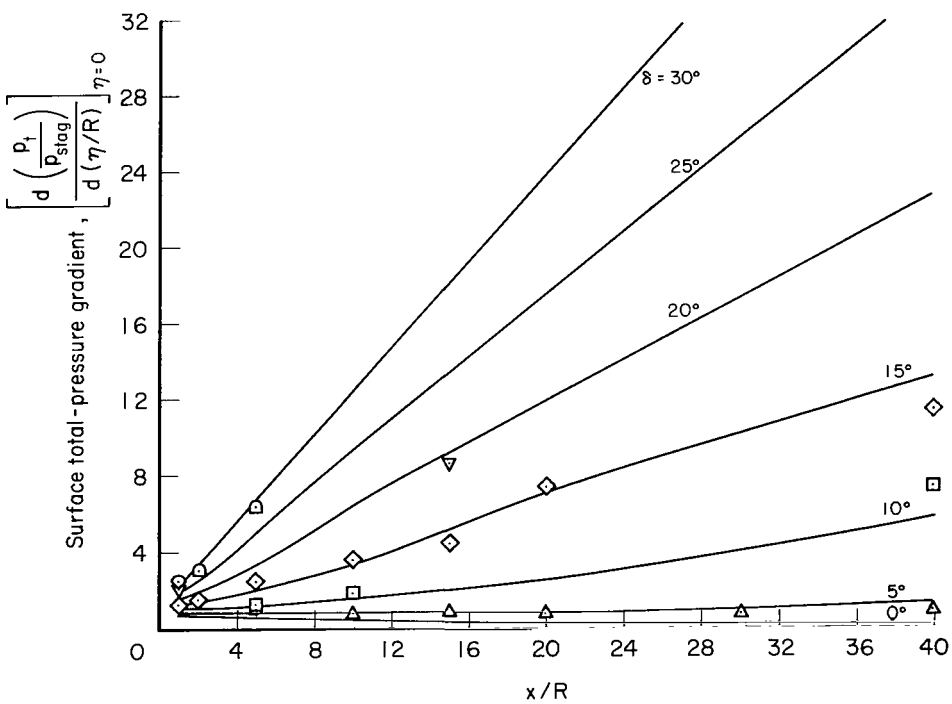

(b) $M_\infty = \infty$

Figure 15.- Total pressure gradient at surface of blunted-cone flows for a specific-heat ratio of 1.667.

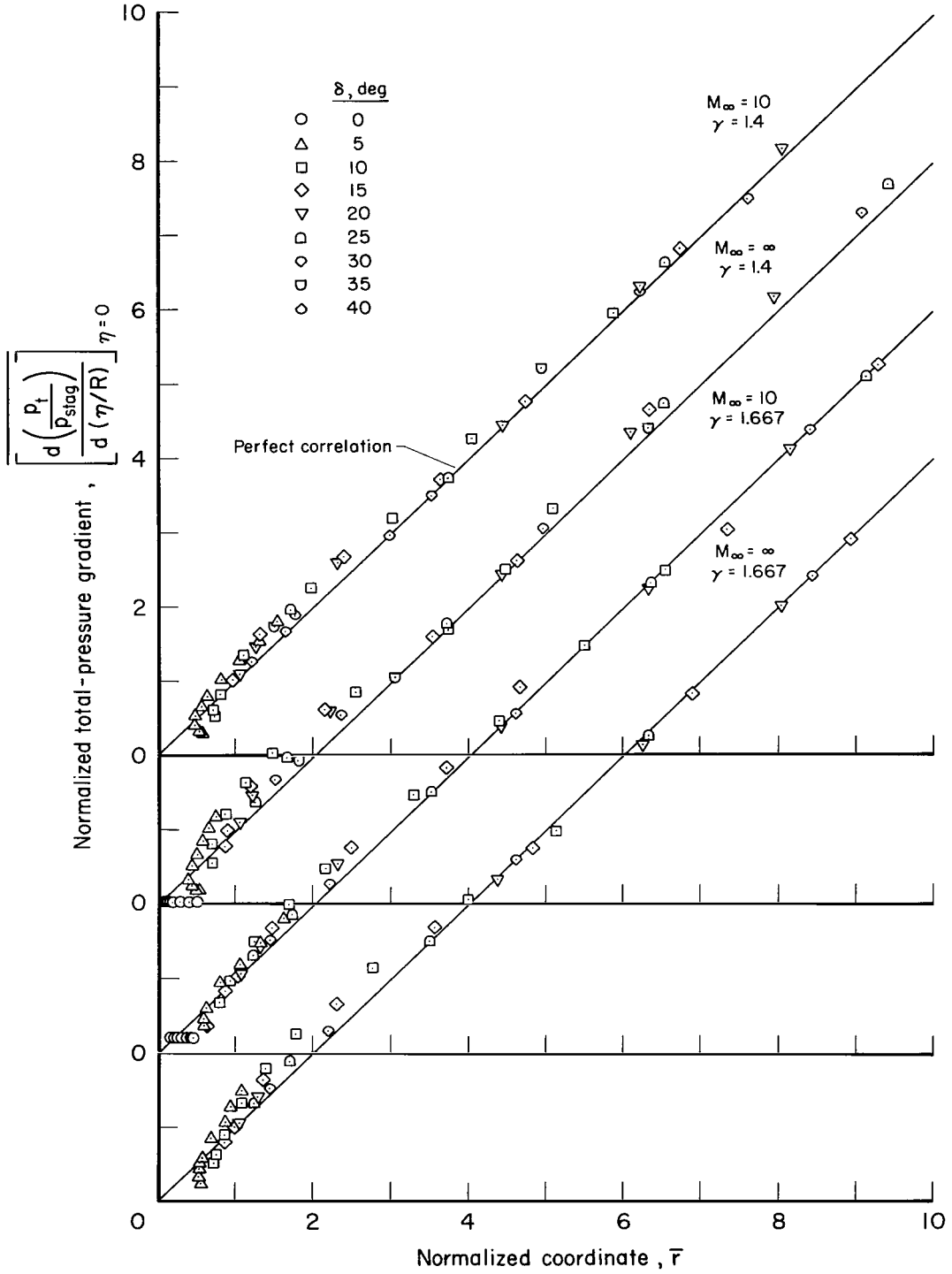

Figure 16.- Variation of normalized total-pressure gradient at surface of blunted-cone flows with normalized radial coordinate from approximate method.

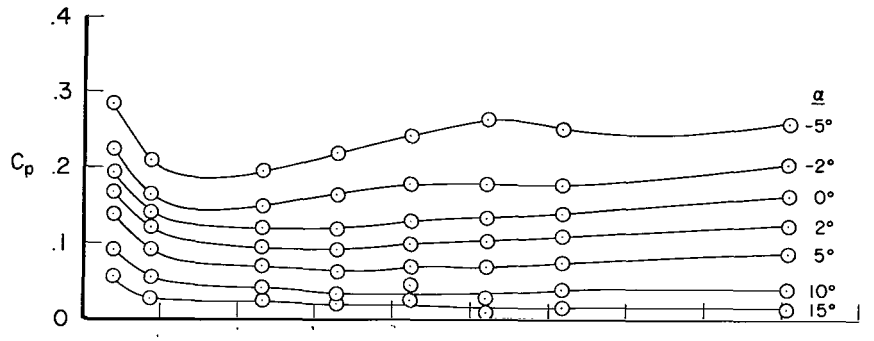

(a) $\varphi = 0^\circ$

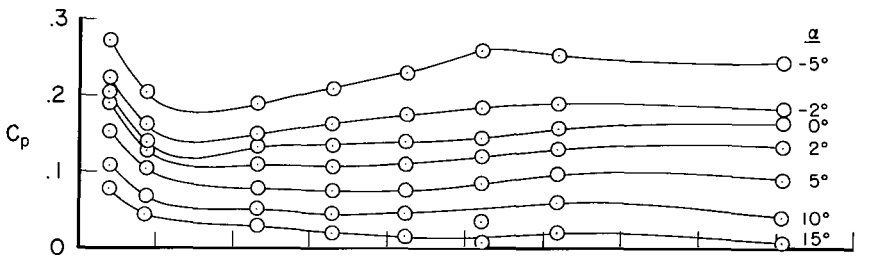

(b) $\varphi = 30^\circ$

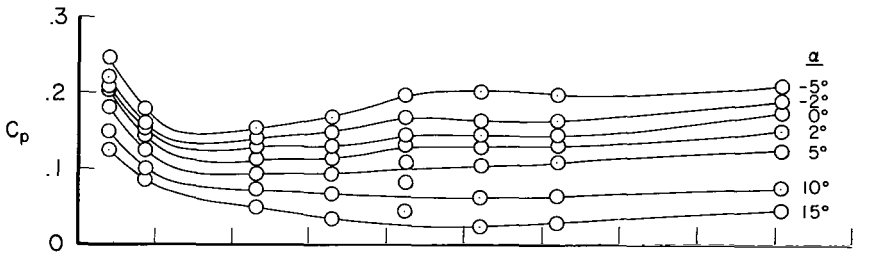

(c) $\varphi = 60^\circ$

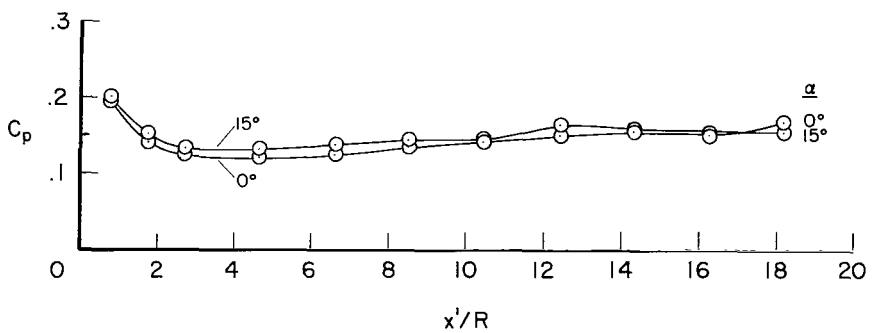

(d) $\varphi = 90^\circ$

Figure 17.- Experimental pressure distribution for a 15° half-angle blunted cone; $M_\infty = 5.25$, $Re^*_\infty = 1.4 \times 10^6$.

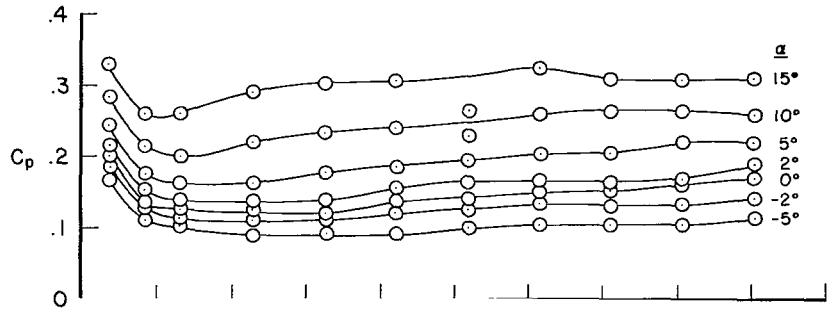

(e) $\varphi = 120^\circ$

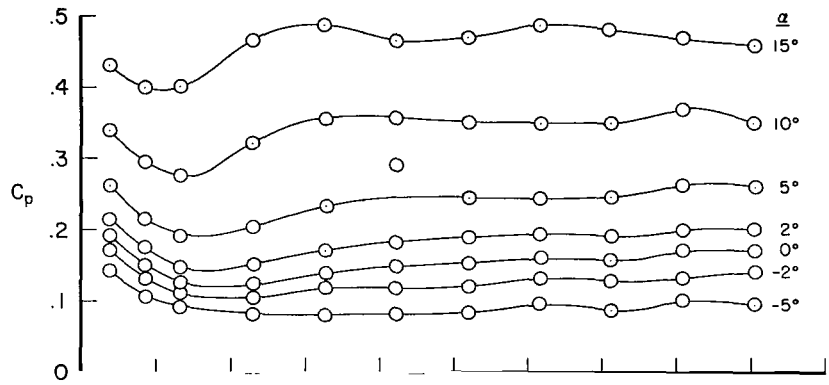

(f) $\varphi = 150^\circ$

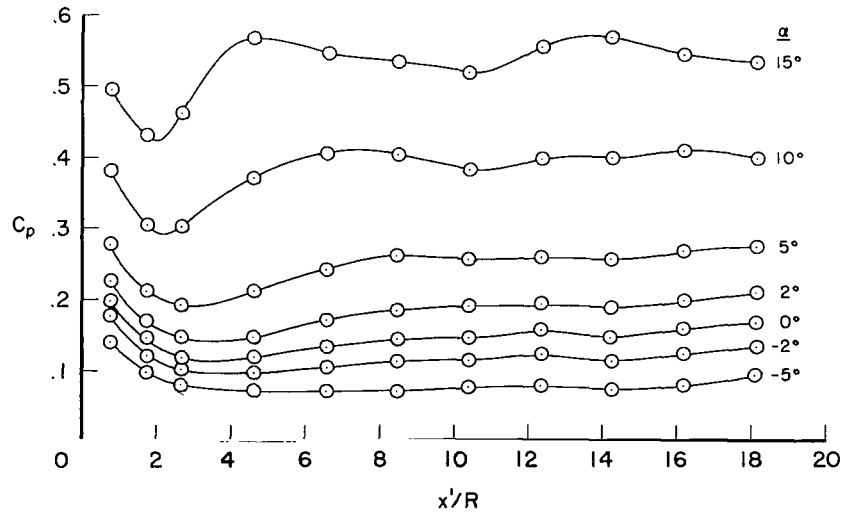

(g) $\varphi = 180^\circ$

Figure 17.- Concluded.

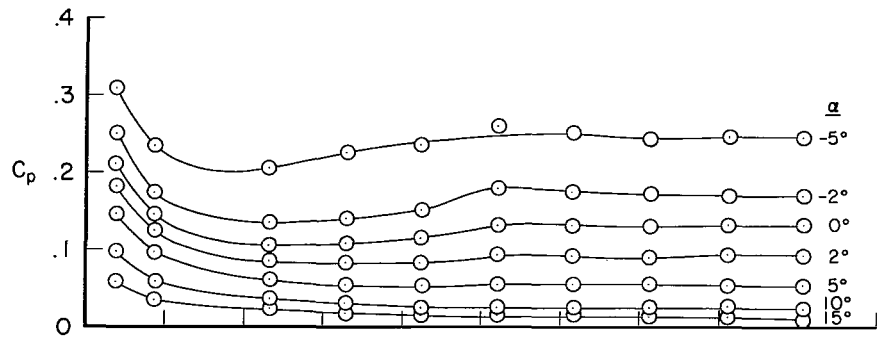

(a) $\varphi = 0^\circ$

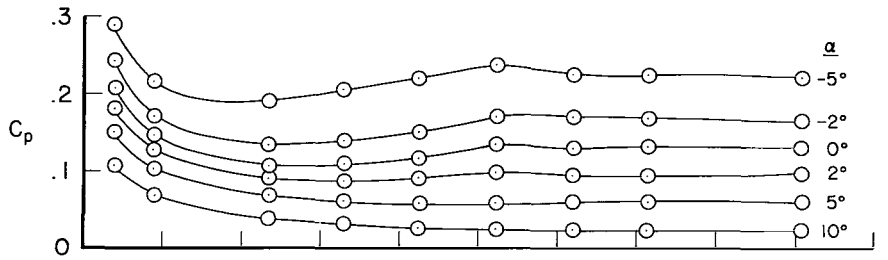

(b) $\varphi = 30^\circ$

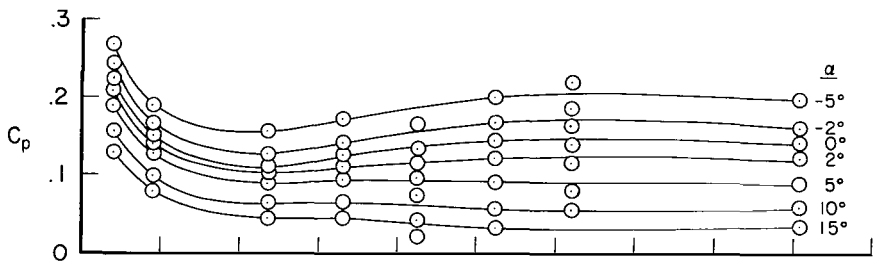

(c) $\varphi = 60^\circ$

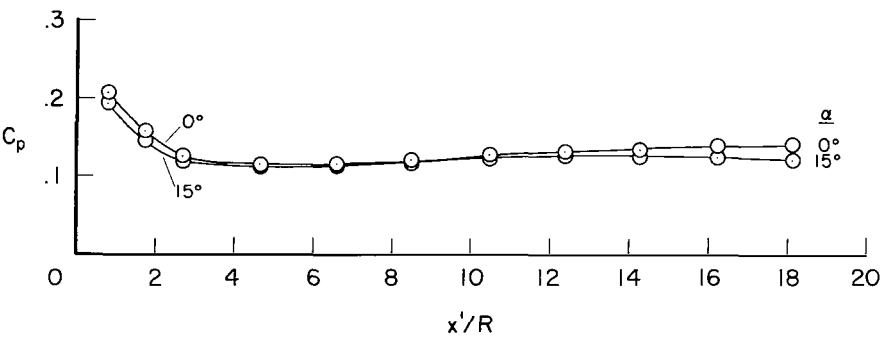

(d) $\varphi = 90^\circ$

Figure 18.- Experimental pressure distribution for a 15° half-angle blunted cone; $M_\infty = 7.4$, $Re^*_\infty = 3.2 \times 10^6$.

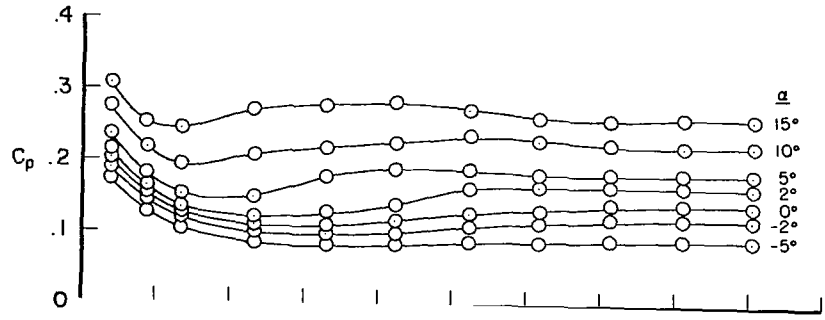

(e) $\varphi = 120^\circ$

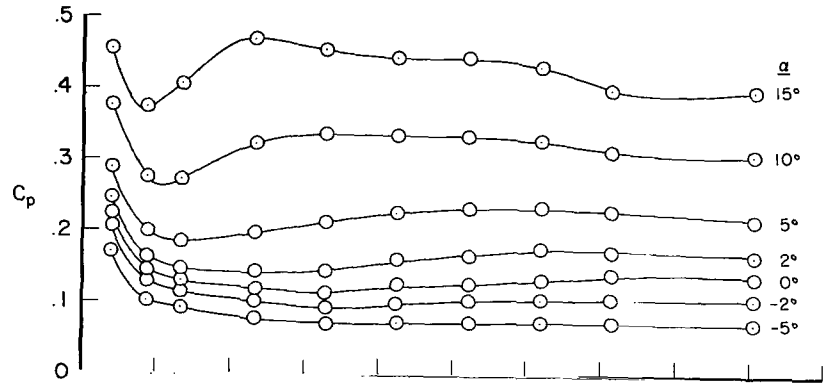

(f) $\varphi = 150^\circ$

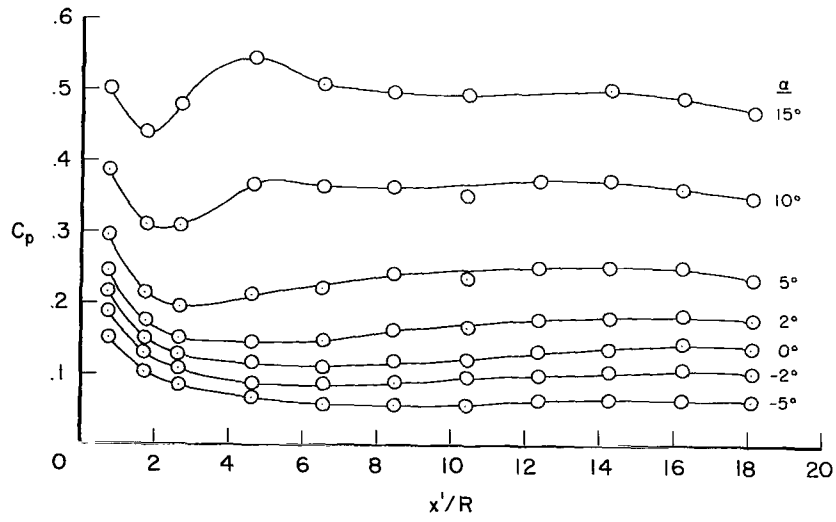

(g) $\varphi = 180^\circ$

Figure 18.- Concluded.

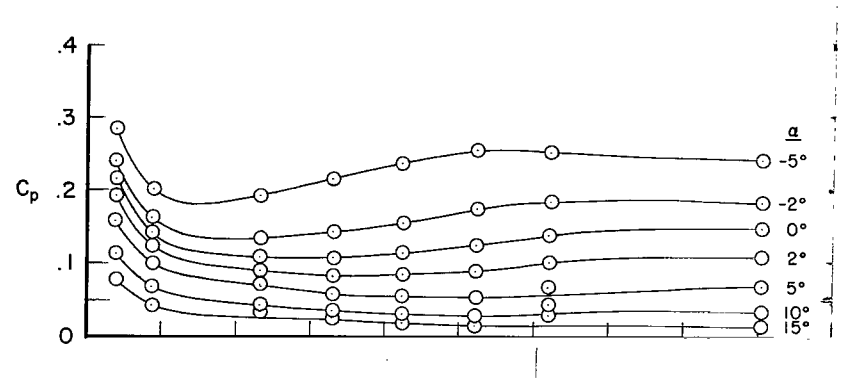

(a) $\varphi = 0^{\circ}$

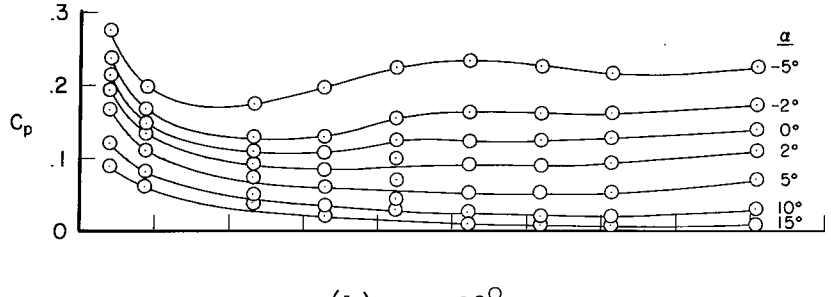

(b) $\varphi = 30^{\circ}$

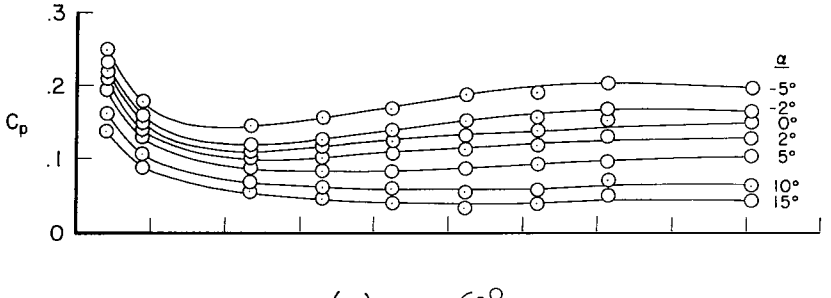

(c) $\varphi = 60^{\circ}$

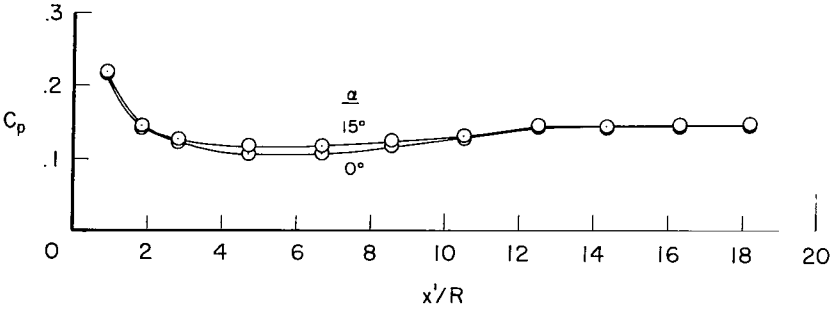

(d) $\varphi = 90^{\circ}$

Figure 19.- Experimental pressure distribution for a 15° half-angle blunted cone; $M_{\infty} = 10.6$, $Re^{*}_{\infty} = 1.0 \times 10^{6}$.

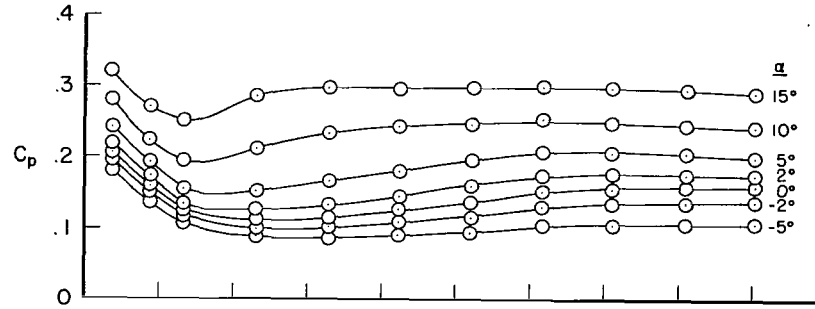

(e) $\varphi = 120^\circ$

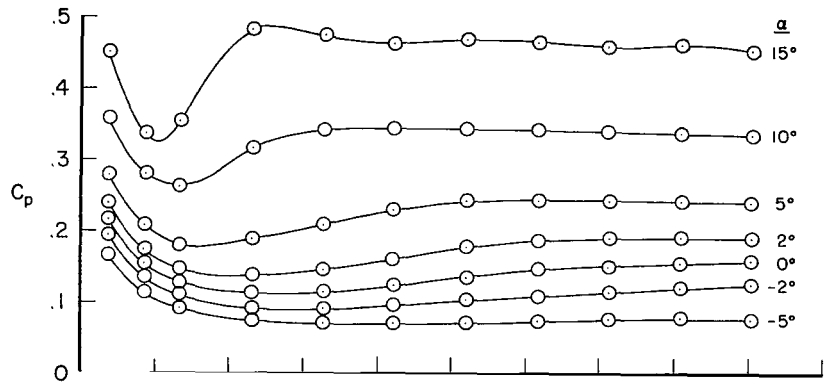

(f) $\varphi = 150^\circ$

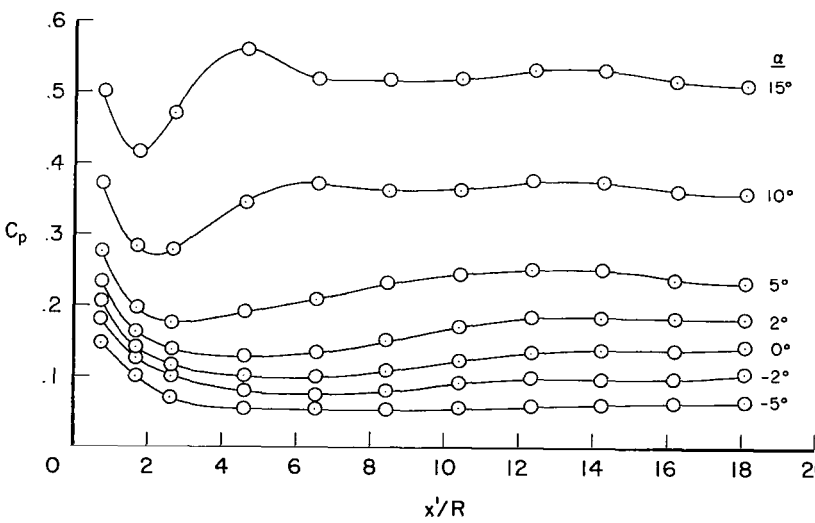

(g) $\varphi = 180^\circ$

Figure 19.- Concluded.

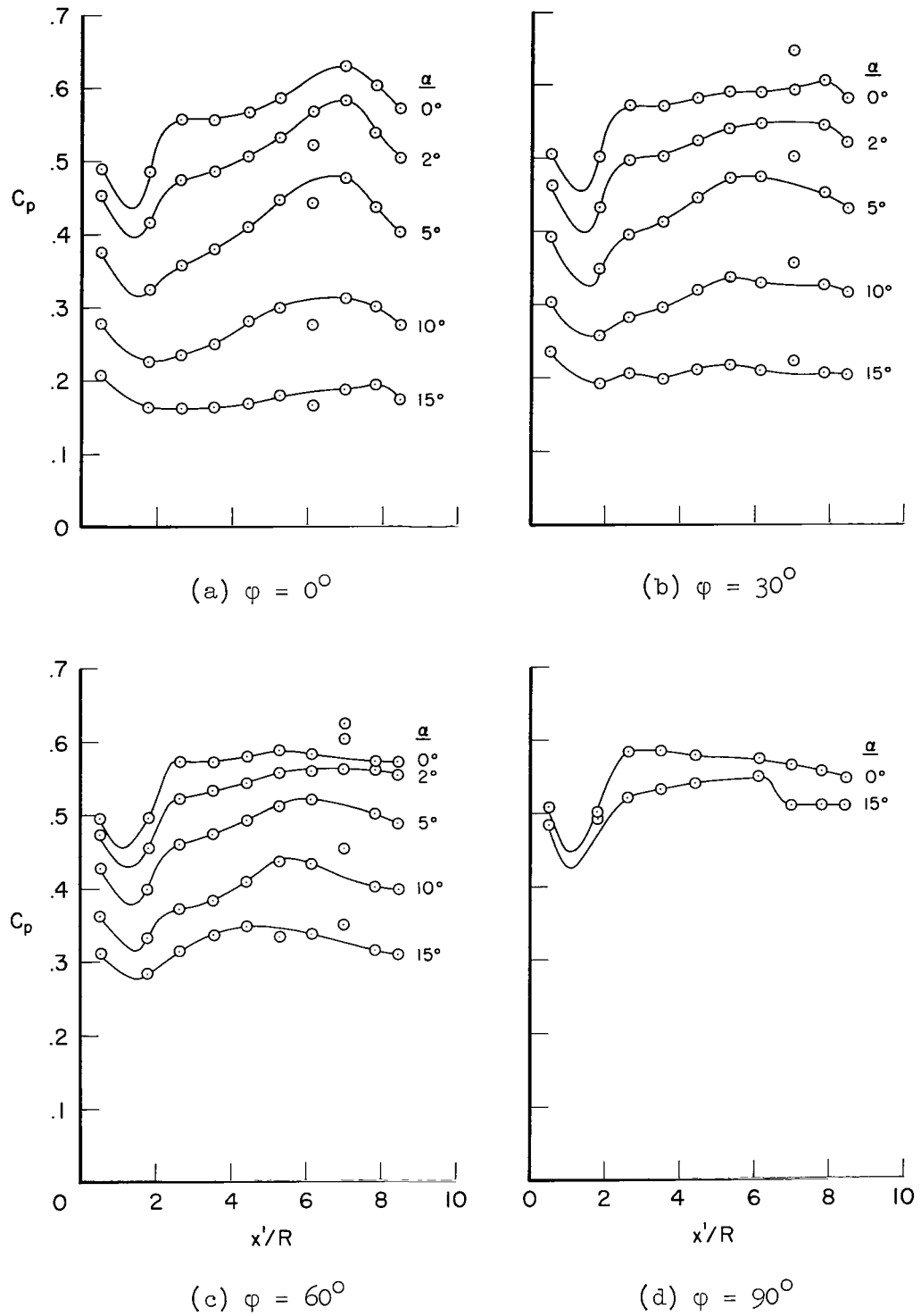

Figure 20.- Experimental pressure distribution for a 30° half-angle blunted cone; $M_\infty = 5.25$, $Re^*_\infty = 1.4 \times 10^6$.

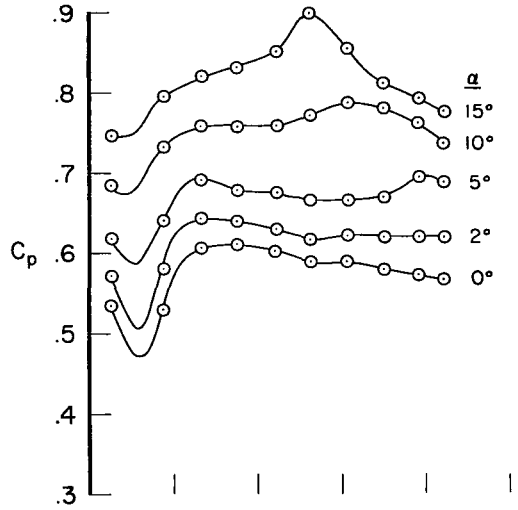

(e) $\varphi = 120^{\circ}$

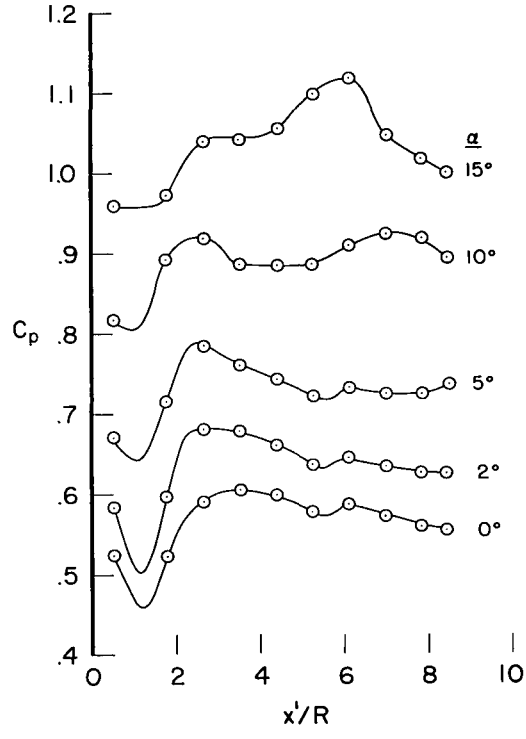

(f) $\varphi = 150^{\circ}$

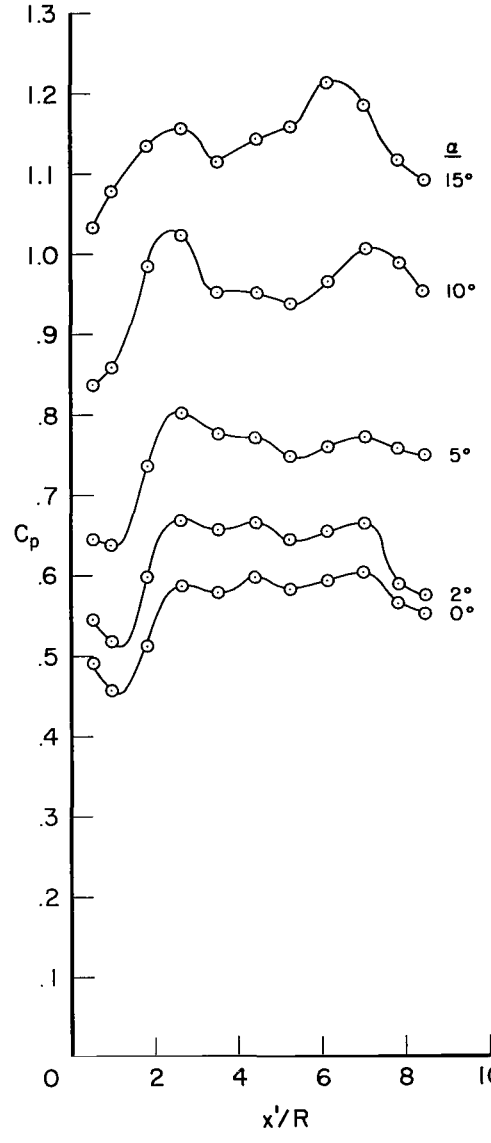

(g) $\varphi = 180^{\circ}$

Figure 20.- Concluded.

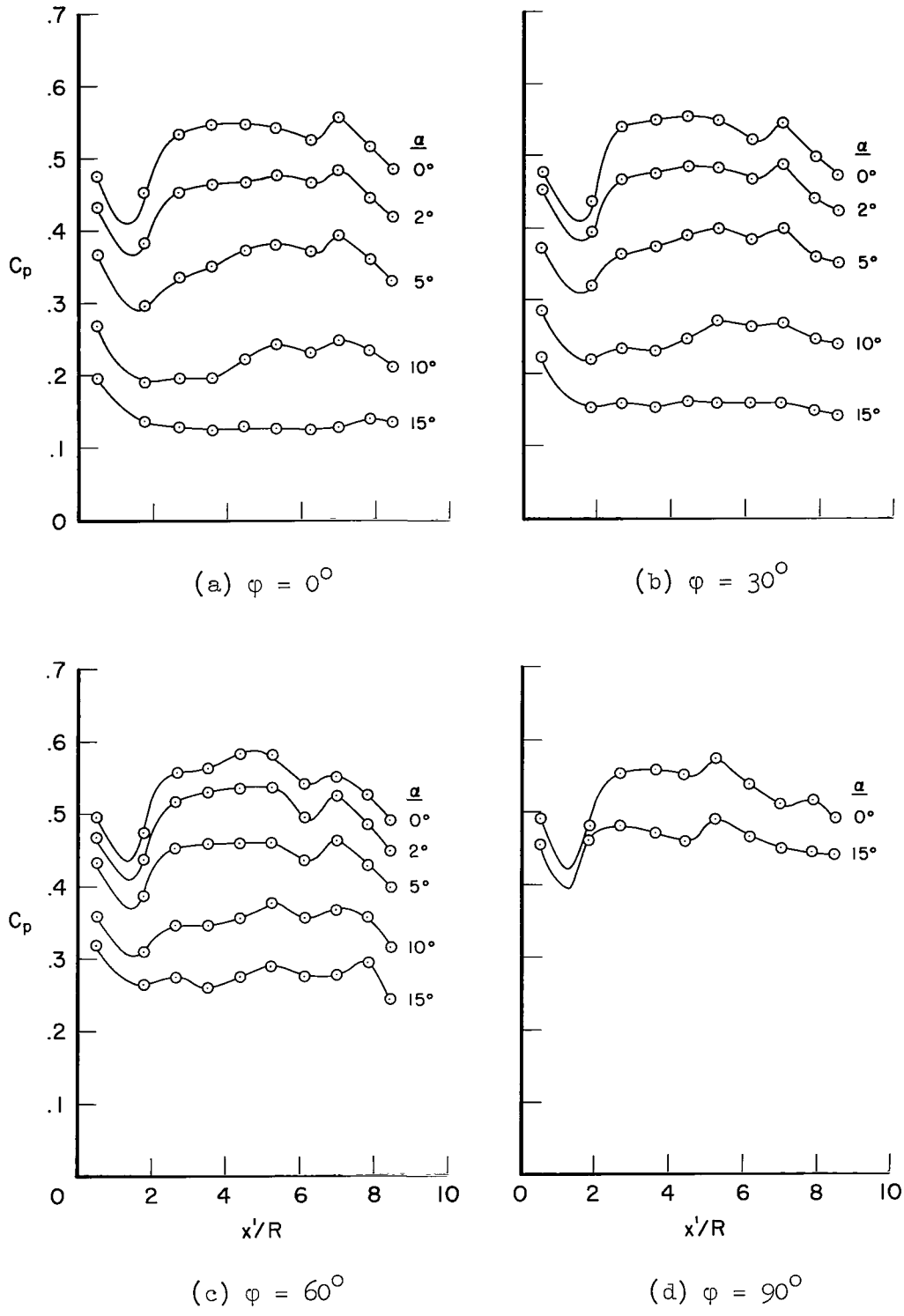

Figure 21.- Experimental pressure distribution for a 30° half-angle blunted cone; $M_\infty = 7.4$, $Re^*_\infty = 3.2 \times 10^6$.

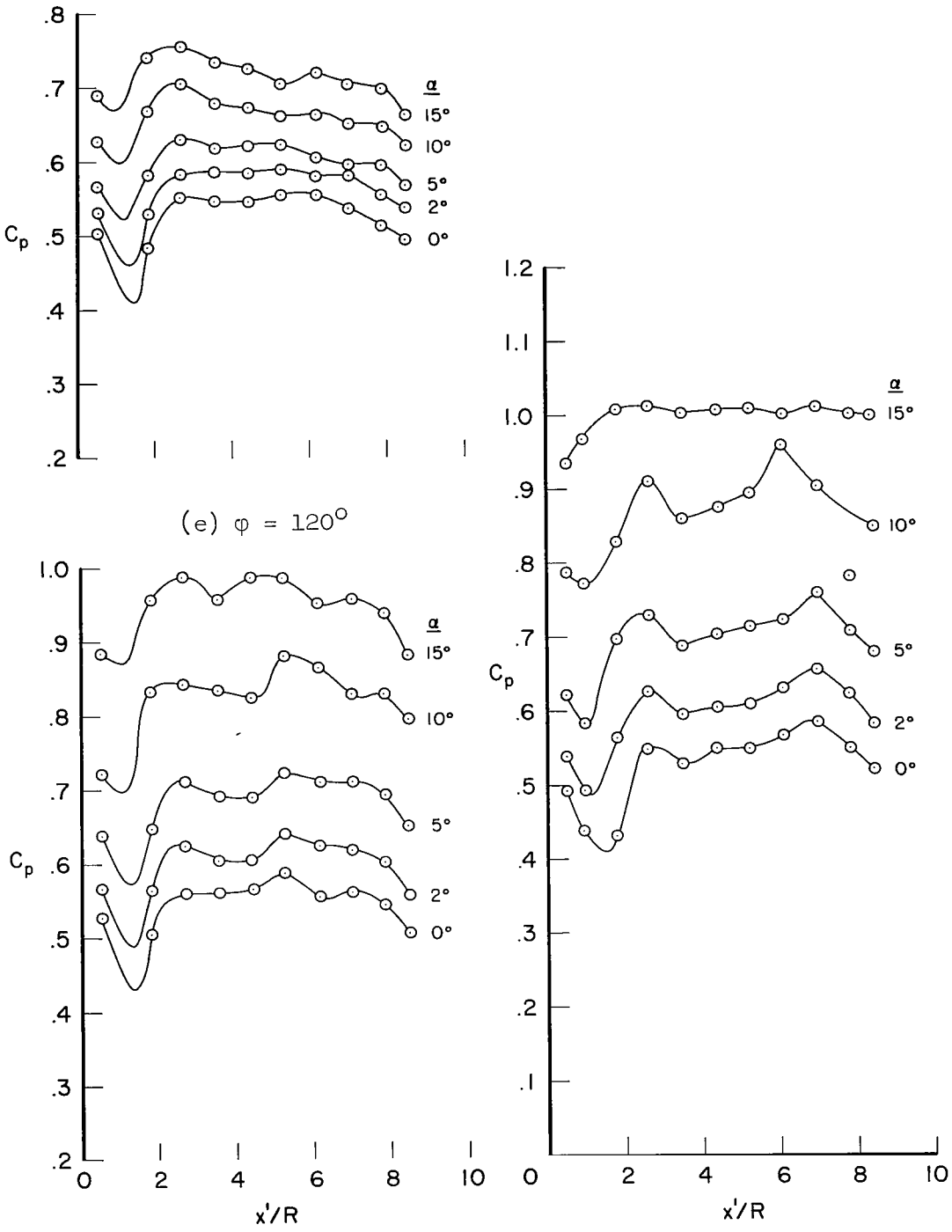

Figure 21.- Concluded.

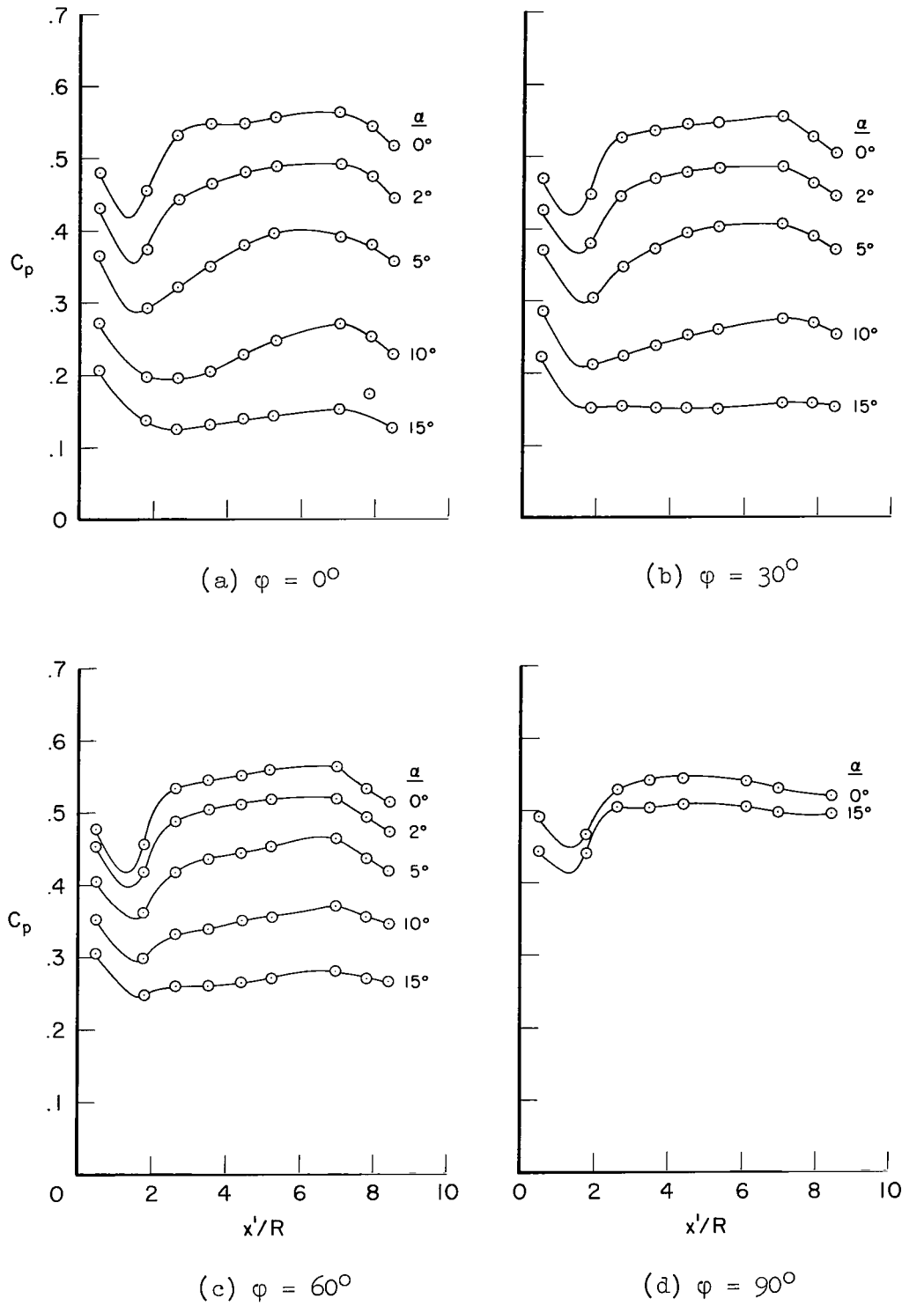

Figure 22.- Experimental pressure distribution for a 30° half-angle blunted cone; $M_\infty = 10.6$, $Re^*_\infty = 1.0 \times 10^6$.

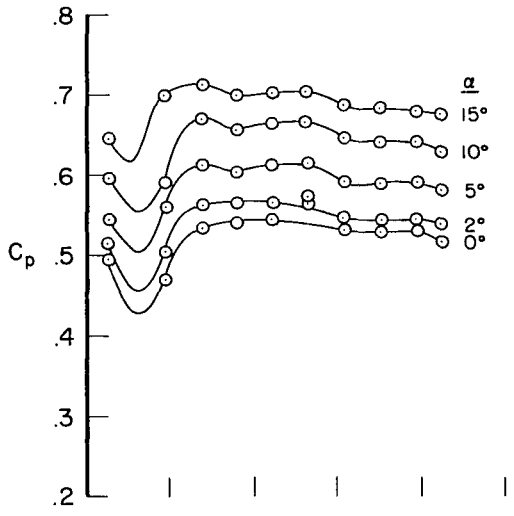

(e) $\varphi = 120^{\circ}$

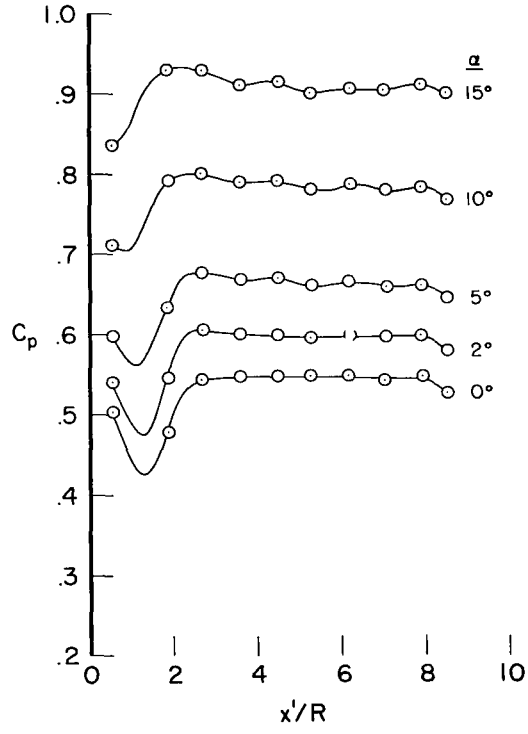

(f) $\varphi = 150^{\circ}$

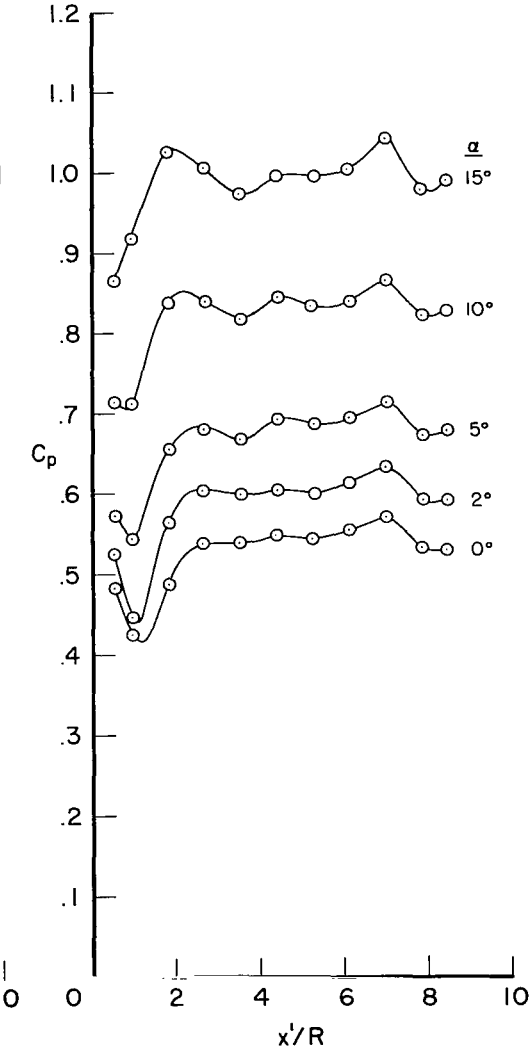

(g) $\varphi = 180^{\circ}$

Figure 22.- Concluded.

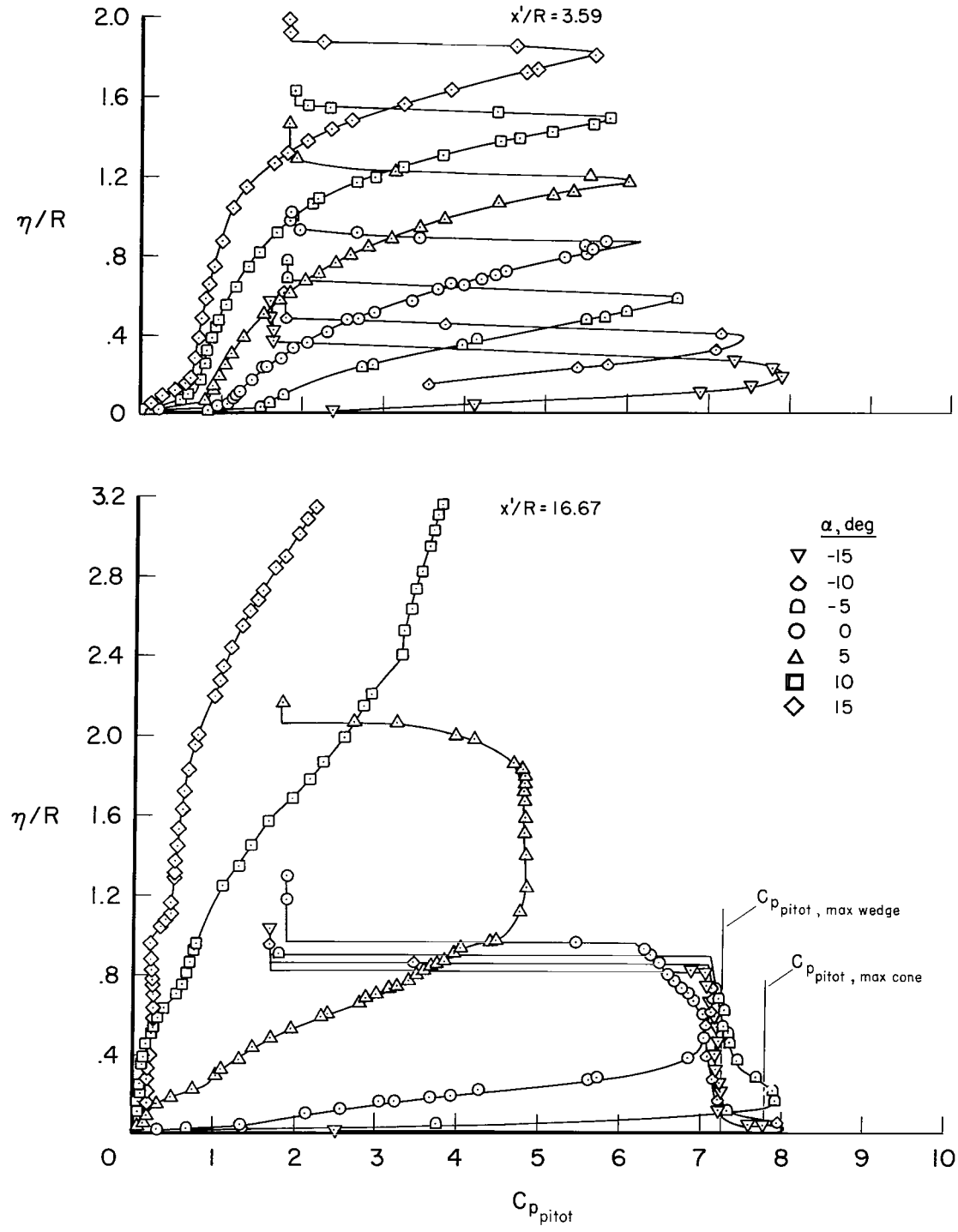

(a) $\varphi = 0^{\circ}$

Figure 23.- Experimental pitot-pressure surveys of the shock layer for a 15° half-angle blunted cone; $M_{\infty} = 10.6$, $Re^{*}_{\infty} = 1.0 \times 10^{6}$.

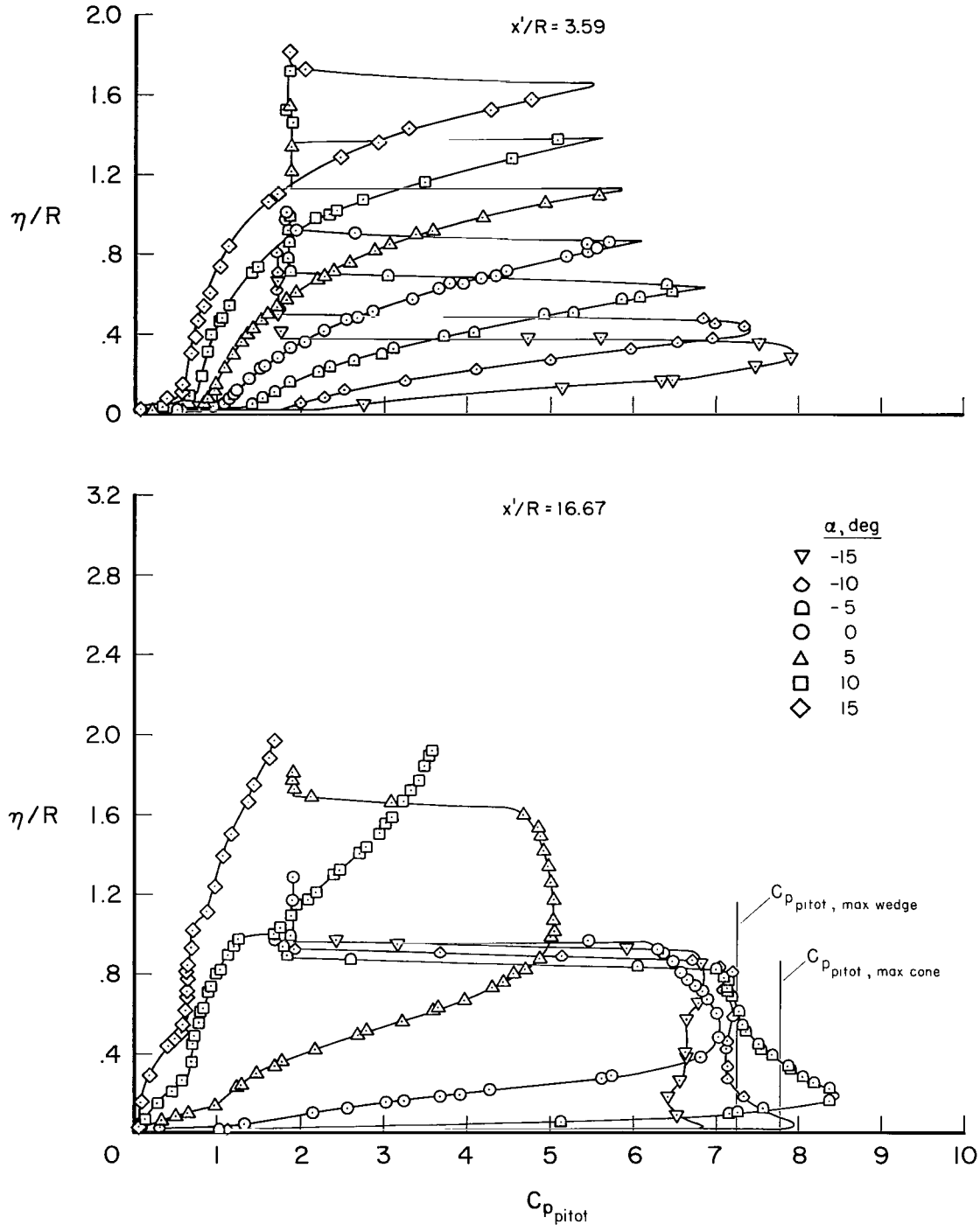

(b) $\varphi = 30^{\circ}$

Figure 23.- Continued.

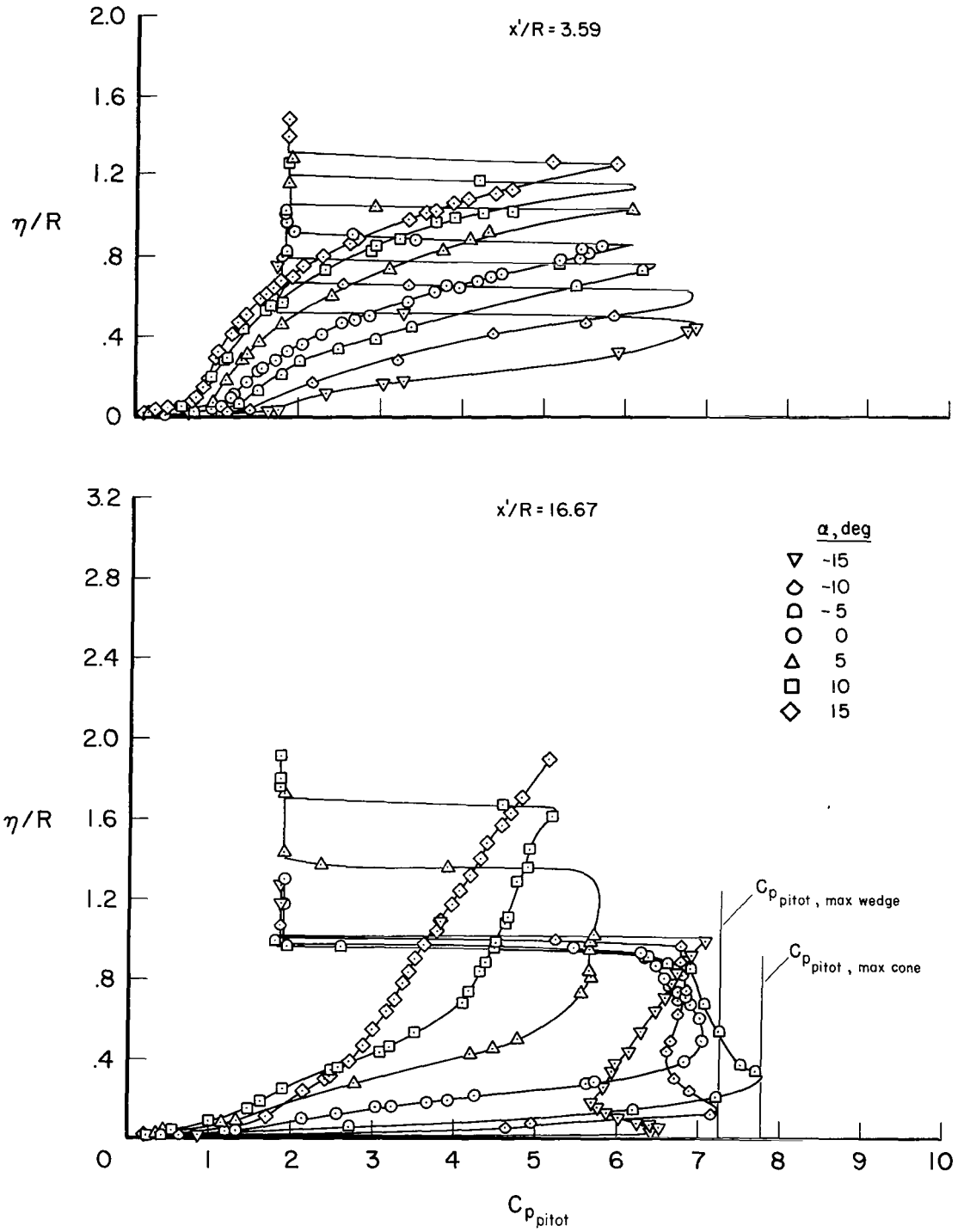

(c) $\varphi = 60^{\circ}$

Figure 23.- Continued.

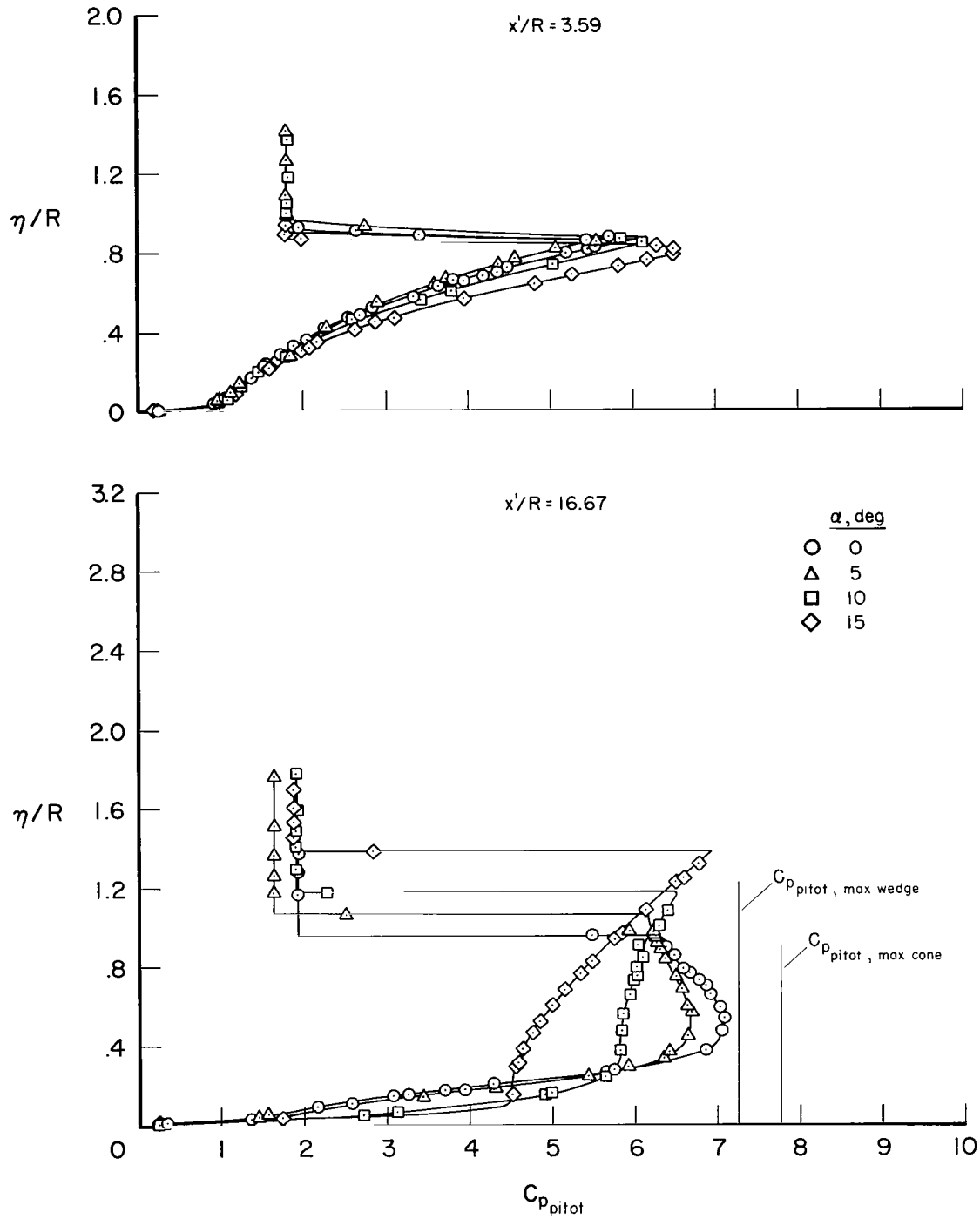

(d) $\varphi = 90^{\circ}$

Figure 23.- Concluded.

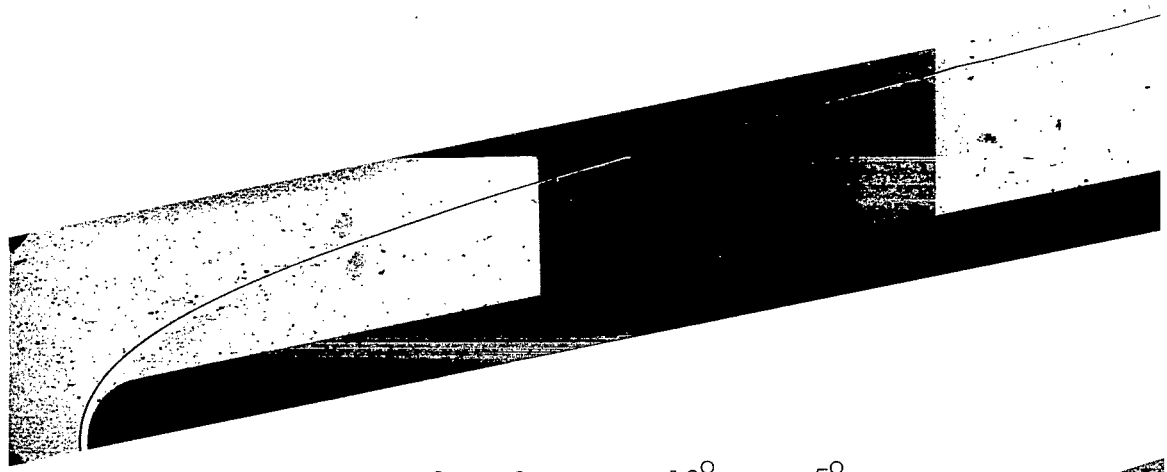

Leeward surface; $\omega = 10^{\circ}$, $\alpha = 5^{\circ}$.

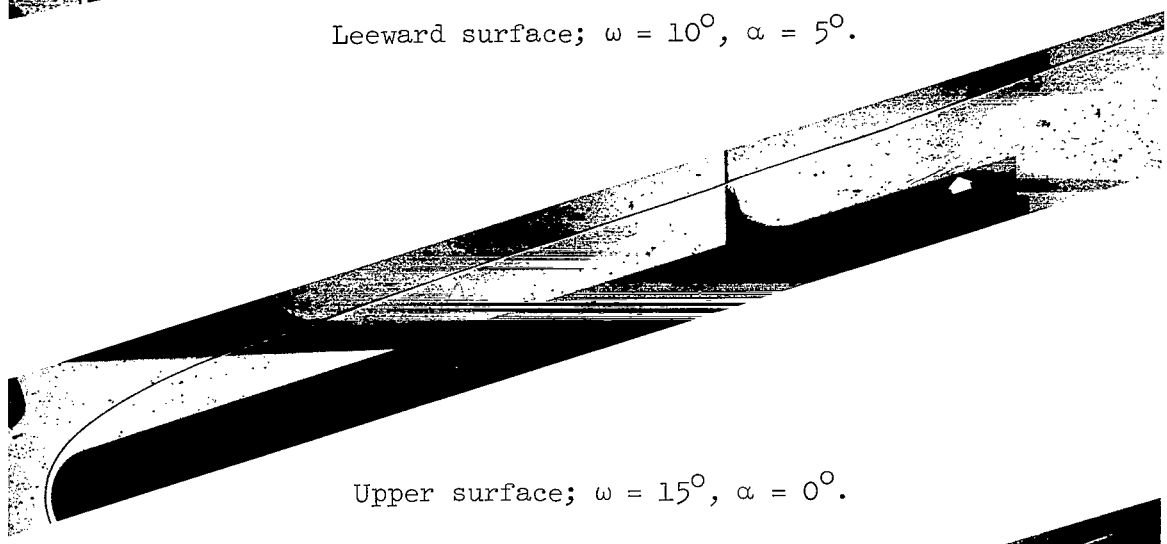

Upper surface; $\omega = 15^{\circ}$, $\alpha = 0^{\circ}$.

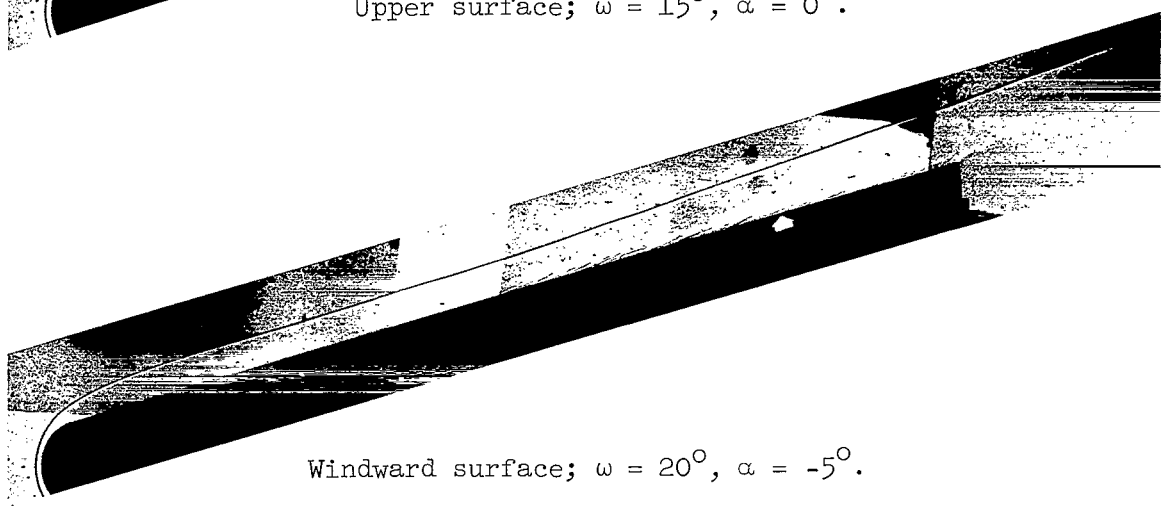

Windward surface; $\omega = 20^{\circ}$, $\alpha = -5^{\circ}$.

Figure 24.- Effect of surface incidence on boundary-layer transition on a blunted cone; $M_{\infty} = 7.4$, $Re^{*} = 3.7 \times 10^{6}$, $\delta = 15^{\circ}$.

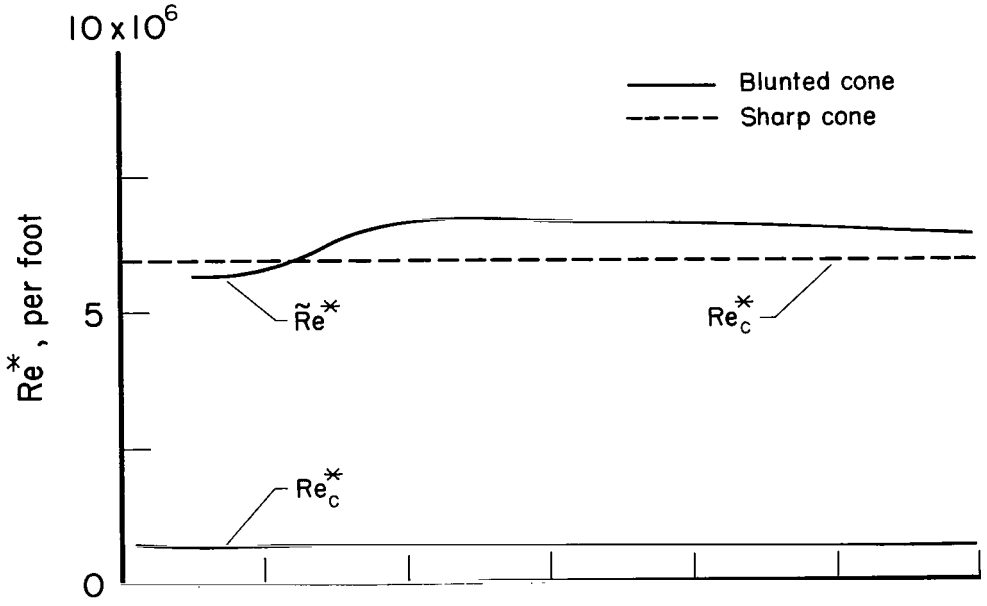

(a) $\delta = 15^\circ$

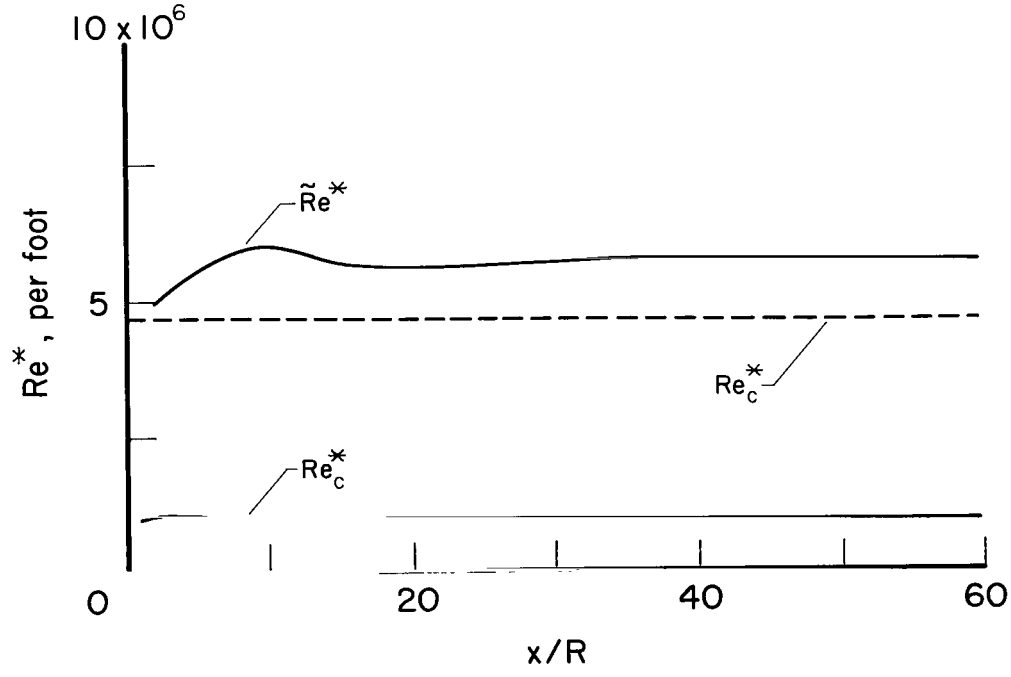

(b) $\delta = 30^\circ$

Figure 25.- Variation of Reynolds number per foot in the shock layer of blunted and sharp cones; $M_\infty = 7$, $T_{t_\infty} = 2000^\circ$ R, $P_{t_\infty} = 1200$ psia, $\alpha = 0^\circ$, $\gamma = 1.4$.

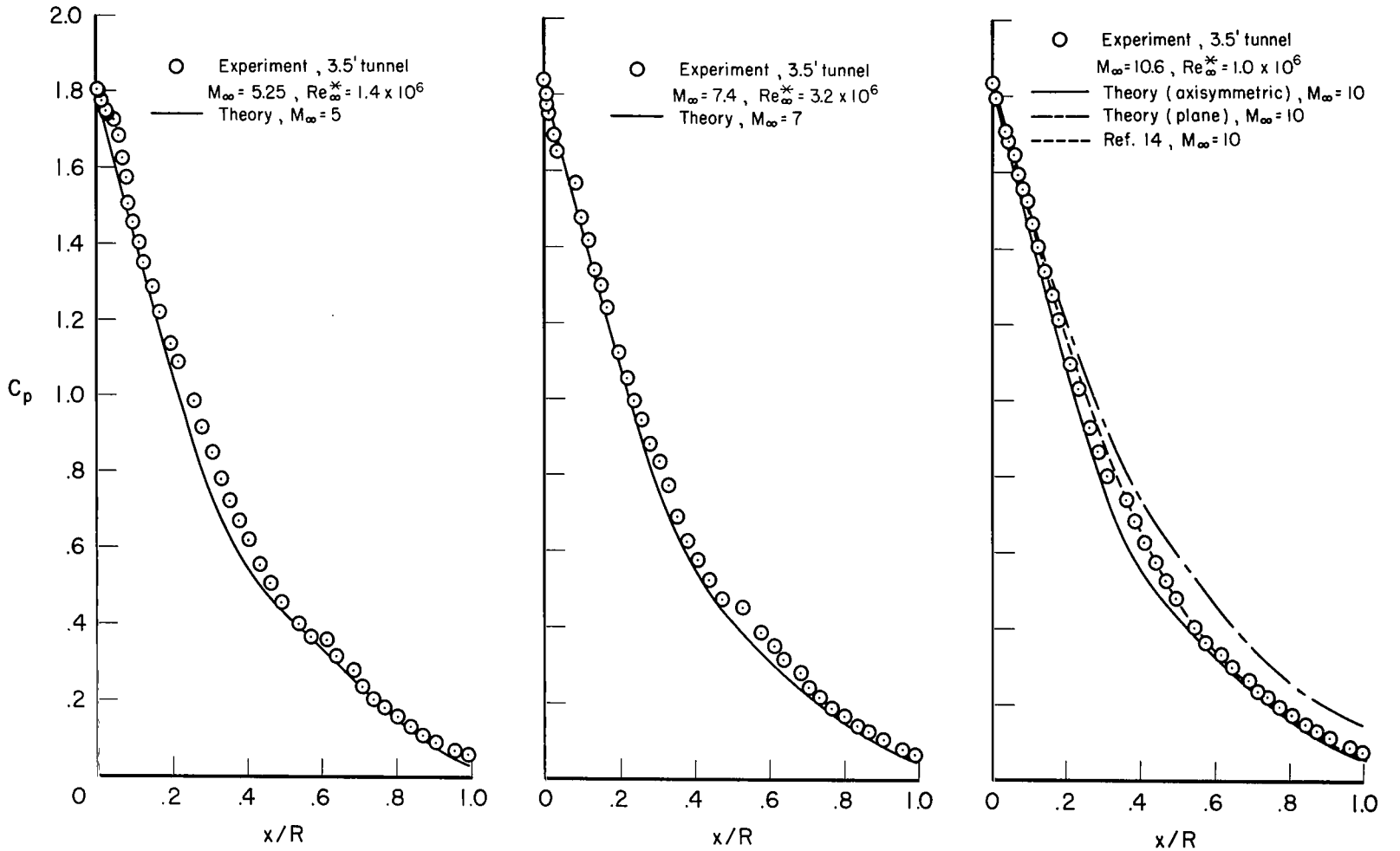

Figure 26.- A comparison of theoretical pressure distribution of the hemispherical nose with experiment, $\gamma = 1.4$.

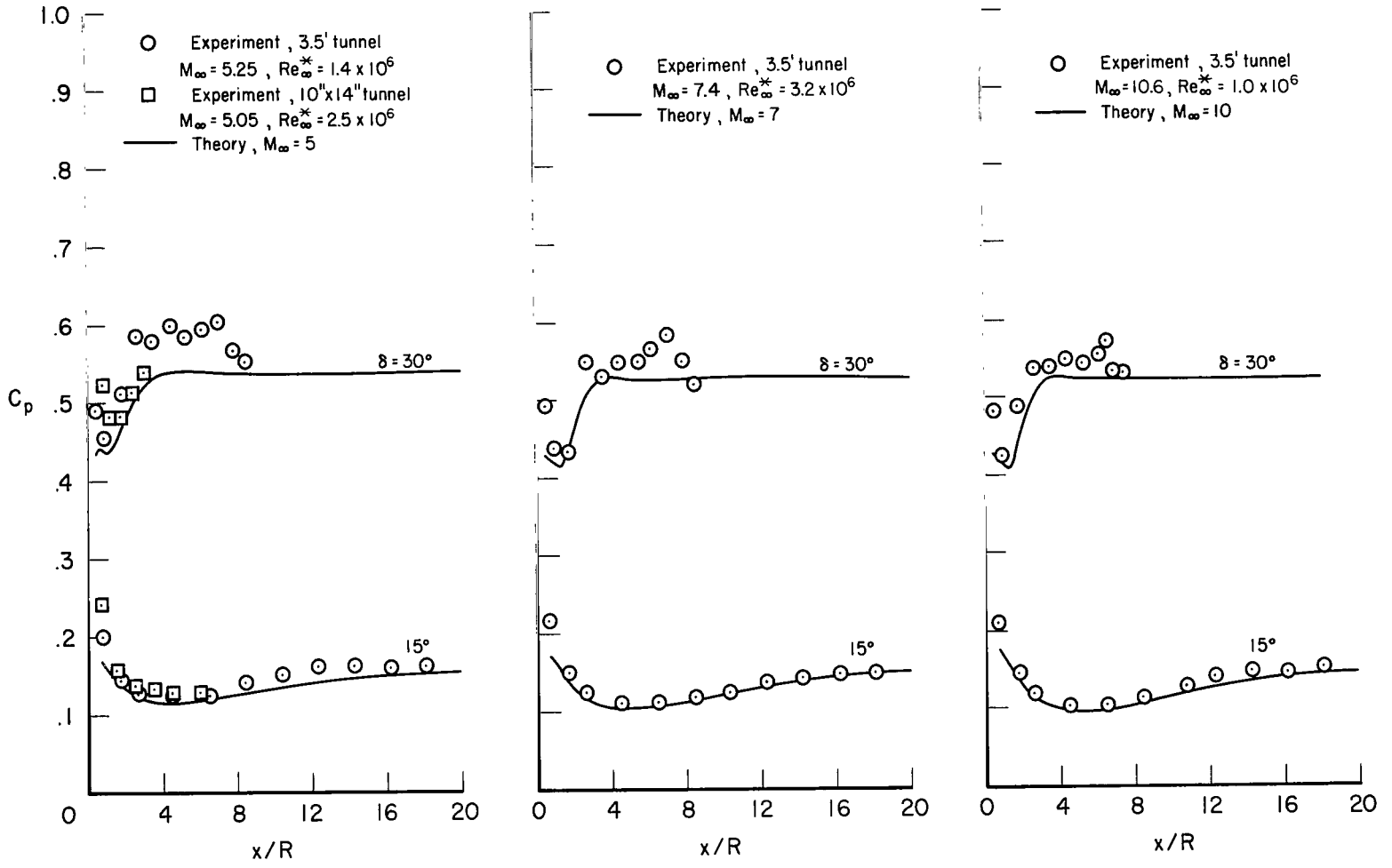

Figure 27.- A comparison of theoretical pressure distribution of blunted cones with experiment; $\gamma = 1.4$, $\alpha = 0^\circ$.

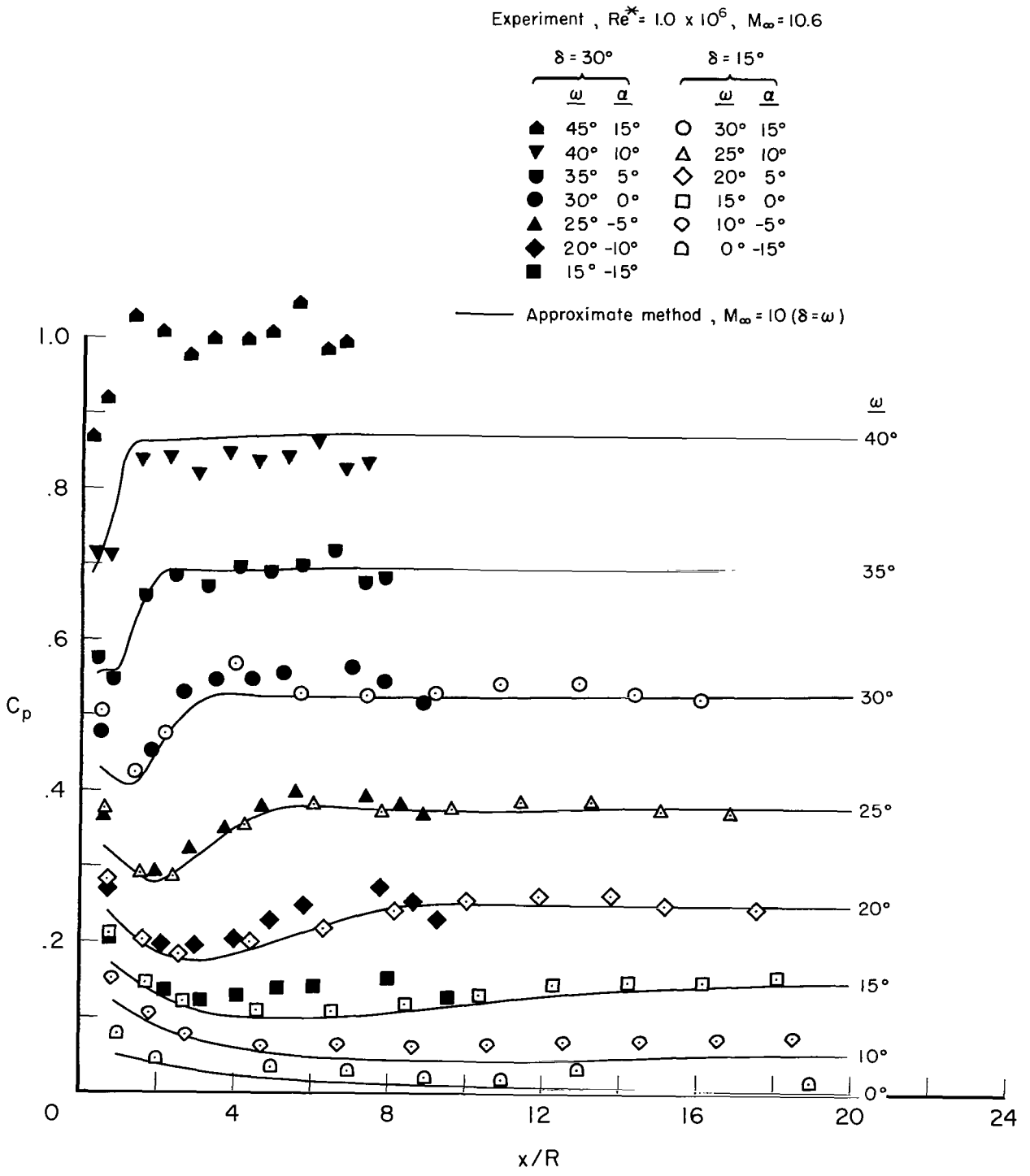

Figure 28.- A comparison of experimental pressure distribution with an approximate method for the same inclinations of the blunted cone surfaces; $\varphi = 0^\circ$ and 180°, $\gamma = 1.4$.

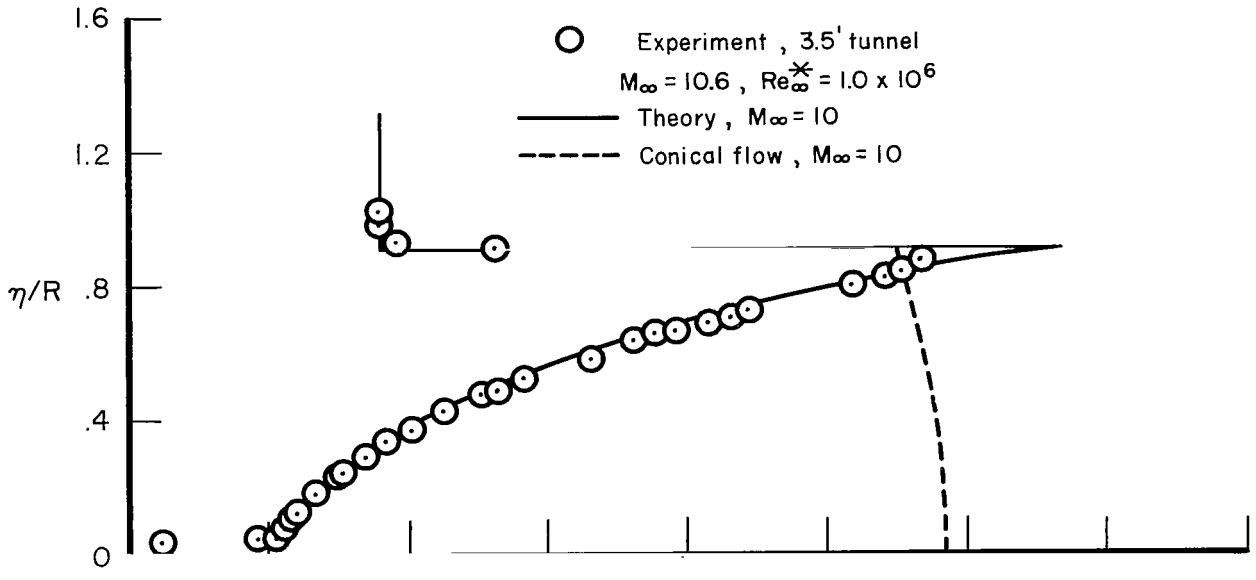

(a) x/R = 3.59

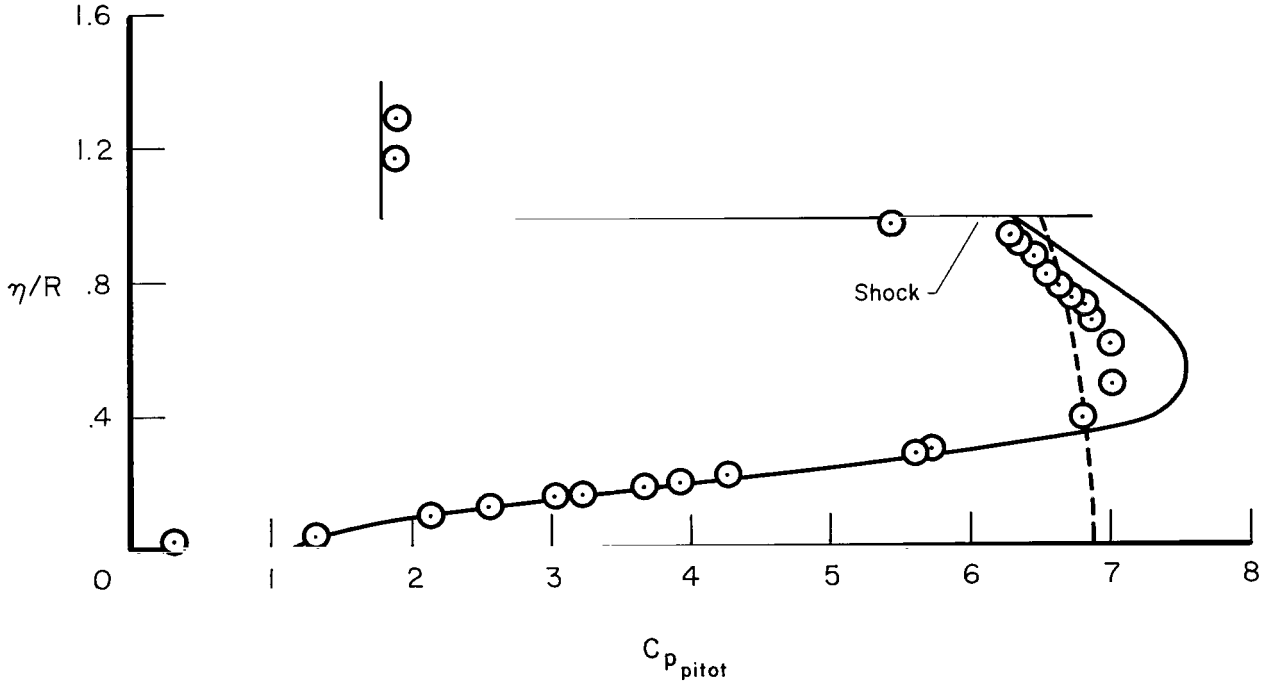

(b) x/R = 16.67

Figure 29.- A comparison of experimental pitot-pressure measurements with theory for the 15° half-angle blunted cone, $\gamma = 1.4$.

"The aeronautical and space activities of the United States shall be conducted so as to contribute . . . to the expansion of human knowledge of phenomena in the atmosphere and space. The Administration shall provide for the widest practicable and appropriate dissemination of information concerning its activities and the results thereof."

—NATIONAL AERONAUTICS AND SPACE ACT OF 1958

NASA SCIENTIFIC AND TECHNICAL PUBLICATIONS

TECHNICAL REPORTS: Scientific and technical information considered important, complete, and a lasting contribution to existing knowledge.

TECHNICAL NOTES: Information less broad in scope but nevertheless of importance as a contribution to existing knowledge.

TECHNICAL MEMORANDUMS: Information receiving limited distribution because of preliminary data, security classification, or other reasons.

CONTRACTOR REPORTS: Technical information generated in connection with a NASA contract or grant and released under NASA auspices.

TECHNICAL TRANSLATIONS: Information published in a foreign language considered to merit NASA distribution in English.

TECHNICAL REPRINTS: Information derived from NASA activities and initially published in the form of journal articles.

SPECIAL PUBLICATIONS: Information derived from or of value to NASA activities but not necessarily reporting the results of individual NASA-programmed scientific efforts. Publications include conference proceedings, monographs, data compilations, handbooks, sourcebooks, and special bibliographies.

Details on the availability of these publications may be obtained from:

SCIENTIFIC AND TECHNICAL INFORMATION DIVISION

NATIONAL AERONAUTICS AND SPACE ADMINISTRATION

Washington, D.C. 20546